

The Dynamics of Artificial Spin Ice in Real and Reciprocal Space



Sophie Ann Morley

School of Physics and Astronomy

University of Leeds

Submitted in accordance with the requirements for the degree of

Doctor of Philosophy

September 2015

For Annie and Norman.

Intellectual Property Statement

The candidate confirms that the work submitted is his/her own, except where work which has formed part of jointly authored publications has been included. The contribution of the candidate and the other authors to this work has been explicitly indicated below. The candidate confirms that appropriate credit has been given within the thesis where reference has been made to the work of others.

This copy has been supplied on the understanding that it is copyright material and that no quotation from the thesis may be published without proper acknowledgement.

The right of Sophie Ann Morley to be identified as Author of this work has been asserted by her in accordance with the Copyright, Designs and Patents Act 1988.

©2015 The University of Leeds and Sophie Ann Morley.

Work from the following jointly authored paper is in first half of chapter 7 of this thesis:

S. A. Morley, A. Stein, M. C. Rosamond, D. A. Venero, A. Hrabec, P. M. Shepley, M.-Y. Im, P. Fischer, M. T. Bryan, D. A. Allwood, P. Steadman, S. Langridge and C. H. Marrows, '(Invited) Temperature and magnetic-field driven dynamics in artificial magnetic square ice', *Proc. SPIE 9551*, 95511Q (2015)

- **Work attributed to the candidate:** Design and management of the project, fabrication of devices, measurements, interpretation and analysis, and writing of parts of the manuscript.
- **Work attributed to others:** A. Stein: fabrication of samples for focussed MOKE experiments. M. C. Rosamond: collaboration in design and fabrication of on-membrane heater and thermometer samples for TXM. D. A. Venero, A. Hrabec and P. M. Shepley: made up the experimental beamtime team for the TXM experiments. M.-Y. Im, P. Fischer: assisted in the TXM measurements carried out at ALS. M. T. Bryan: involved in the fMOKE measurements. D. A. Allwood: provided support and management for M. T. Bryan. P. Steadman, S. Langridge: provided support and management for S. A. Morley. C. H. Marrows: management of the project, interpretation and analysis, wrote part of and edited the manuscript.

Acknowledgements

I would like to start by thanking my primary supervisor, Prof. Chris Marrows, for his encouragement to first apply for such an exciting project and for providing countless opportunities along the way. His guidance throughout has proved invaluable, foremost in an academic sense, but also from a culinary point of view. Secondly, Prof. Sean Langridge has always offered his considered and insightful opinion, particularly on how to avoid the ‘faux-pas’ minefield of networking. Finalment, merci a Dr. Paul Steadman whose knowledge of X-rays, RASOR and parking penalty anecdotes made the many beamtimes at Diamond enjoyable and productive. On a similar note, Raymond Fan and Mark Sussmuth at I10 were always on hand to help fix any problems quickly and efficiently and were heavily involved in the set-up of the beamline for the XPCS technique. Similarly, thanks for the assistance of Mi-Young Im and Peter Fischer for measurements carried out at the TXM beamline.

Also a special thanks to the the many people involved in the beamtime teams, Susan Riley, Yue Li, Dr. ‘Txema’ Porro, Philippa Shepley, Dr. Ales ‘Fat-Fingers’ Hrabec and last but not least Dr. Diego Alba Venero, who was there from the beginning and really helped get the XPCS technique off the ground. His ability at staying awake to man beamlines was second to none. The technical know-how from the nanofabrication experts, Dr. Aaron Stein and Dr. Mark Rosamond, deserve a special mention. It is through their hard efforts that I was able to learn so much and meet tough sample deadlines, thank you both very much. Thanks to Rowan for helpful discussions regarding superparamagnetism. And also to Dr. Gavin Burnell for expert advice on data analysis with Python. Jason Morgan must also get a special mention for having been a great spin ice mentor at the start of my PhD. Also, thanks to Dr. Nick Porter for taking me through the ‘School of Nick’ - my file directories would probably be a complete mess without him.

My office mates May and Ales kept spirits high throughout all the PhD elements. The rest of the CM group who have made it such a great and collaborative place to work. Whether we’re out on the top of a local mountain (or hill to the non-Brits), down at the Fenton on a Friday or consuming

too much caffeine at coffee time, there's a great social element to the group which I think nurtures the mind and the science. Also, the technicians at Leeds are particularly outstanding and we are a lucky group to have such skilled and lovely people on hand, including John, Brian, Stuart, Leigh, Luke and the late Phil Cale.

Finally, all the love and support of my friends and family throughout, particularly my old flatmate Hannah Copley, who worked across the road in the School of English doing her PhD in tandem. My parents and aunties have always believed in me and kept me grounded. And to Albi who has been able to manage my unsociable hours in the final slog and always offered words of comfort (and perspective). Last but not least are Joe and Philippa who have made the thesis writing process that much more bearable by sharing in the madness!

Abstract

Artificial Spin Ice (ASI) have been fabricated from NiFe in the square geometry over areas 1-2mm². They have small enough volumes to be thermally active within an experimental temperature range. The dynamic hysteresis has been measured using a SQUID-VSM magnetometer. We found that larger dipolar interaction can stabilise the superparamagnetic behaviour and lead to increased order at low temperature. Variation in the observed average blocking temperatures, recorded via hysteresis and zero-field-cooled (ZFC) experiments, is attributed to the distribution of island sizes and interaction effects.

A new synchrotron capability at the I10 beamline in Diamond Light Source (UK) has been implemented and used to measure islands as small as $30 \times 70 \times 8 \text{ nm}^3$. At this size, measuring the exact microstates of the individual nanomagnets is challenging. Although, this method is a scattering process it maintains sensitivity to the microstates of the system by using coherent X-rays to produce a speckle pattern. Dynamics were observed in the speckle pattern in the temperature range 180 - 250 K. The characteristic relaxation time was fitted to a Vogel-Fulcher law, with an activation temperature of $40 \pm 10 \text{ K}$ and freezing temperature of $178 \pm 5 \text{ K}$. From magnetometry measurements and simulations we attribute the activation temperature as originating from the non-uniform magnetic structure at the ends of the islands. The freezing temperature relates well to the energy scale of the interaction.

Finally, a full-field magnetic microscopy method to probe dynamic ASI has been demonstrated; transmission X-ray microscopy (TXM). The method uses circularly-polarised soft X-rays to probe the magnetic orientation of the individual nanoislands. We have developed an on-membrane heater and thermometer, which is capable of temperatures in excess of $\approx 700 \text{ K}$. We have used it to heat the ASI whilst tracking the individual vertex states. We have been able to measure the creation and propagation of emergent monopole excitations and observed increased avalanche velocities and magnetic mobilities at higher temperatures. The largest change in the magnetic mobility was found for the most strongly interacting array, increasing by $1.7 \pm 0.7 \text{ mm}^2 \text{ A}^{-1} \text{ s}^{-1}$ for $\Delta T \approx 30 \text{ K}$.

Abbreviations

AFM	Atomic force microscopy
CCD	Charge-coupled Device
CZP	Condenser Zone Plate
DLS	Dynamic Light Scattering
DPS	Diagonally Polarised State
EBL	Electron-beam Lithography
FC	Field cooled
FM	Ferromagnet
GS	Ground State
ICF	Intensity Correlation Function
LCP	Left Circularly Polarised
LTEM	Lorentz-Transmission Electron Microscopy
MFM	Magnetic Force Microscopy
MOKE	Magneto-Optical Kerr Effect
MZP	Micro-zone Plate
PCS	Photon Correlation Spectroscopy
RASOR	Reflectivity and Advanced Scattering of Ordered Regimes
RCP	Right Circularly Polarised
SEM	Scanning Electron Microscopy
SPM	Superparamagnetic
SP-STM	Spin-polarised Scanning Tunnelling Microscopy
STM	Scanning tunnelling microscopy
SQUID	Superconducting Quantum Interference Device
TXM	Transmission X-ray Microscopy
VSM	Vibrating sample magnetometry
XMCD	X-ray Magnetic Circular Dichroism
XPCS	X-ray Photon Correlation Spectroscopy
XPEEM	X-ray Photo-Emission Electron Microscopy
XRMS	X-ray Resonant Magnetic Scattering
ZFC	Zero field cooled

CONTENTS

1	Introduction	1
1.1	Overview	2
1.2	Nanomagnetic behaviour	5
1.2.1	Single Domain Nanomagnetism	5
1.2.2	Anisotropy and the Stoner-Wohlfarth Model	7
1.2.3	Zero-field thermal reversal and superparamagnetism	9
1.2.4	Dipolar interaction and Frustration	10
2	Literature Review	14
2.1	Water and spin ice	15
2.2	Artificial Spin Ice (ASI) in the athermal limit	16
2.2.1	The square geometry	16
2.2.2	The kagome geometry	18
2.2.3	Emergent monopoles and the flow of magnetic charge	20
2.3	Thermal measurements of ASI	21
3	X-rays and magnetism	23
3.1	Non-resonant X-ray scattering	24
3.2	Bragg diffraction and the crystal lattice	25
3.3	Magnetic enhancement at resonance	26
3.3.1	X-ray magnetic circular dichroism (XMCD)	27
3.3.2	X-ray resonant magnetic scattering (XRMS) and magnetic microscopy	28
3.4	X-ray photon correlation spectroscopy (XPCS)	29
3.4.1	Ergodic vs. non-ergodic	31

3.5	Summary	33
4	Methods	34
4.1	Introduction	35
4.2	Nanofabrication	35
4.2.1	Electron beam Lithography	35
4.2.2	Thin Film Deposition	38
4.2.3	Ion Milling	39
4.2.4	Microheater and thermometer fabrication	40
4.3	Characterisation	42
4.3.1	Scanning Electron Microscopy	42
4.3.2	Atomic Force Microscopy	43
4.3.3	SQUID-Vibrating Sample Magnetometry (VSM)	44
4.3.4	X-Ray Reflectivity	46
4.4	Soft X-ray Methods	46
4.4.1	Transmission X-Ray Microscopy	46
4.4.2	Soft X-ray Scattering	48
4.5	Micromagnetic Simulation	54
4.5.1	MuMax Package	55
5	Magnetometry of Thermal Artificial Spin Ice	56
5.1	Introduction	57
5.1.1	Experimental set-up	57
5.2	$m - H$ hysteresis loops with temperature	58
5.3	AC susceptibility	59
5.4	Thickness and interaction dependence	61
5.5	Larger lateral islands with small thickness	63
5.6	Conclusions	67
6	Magnetic X-ray photon correlation spectroscopy (XPCS) to track the dynamics of Artificial Spin Ice	70
6.1	Introduction	71
6.2	X-ray Resonant magnetic scattering of square artificial spin ice with incoherent light	71
6.2.1	Bragg diffraction using a point detector	72

6.3	Coherent scattering from artificial spin ice	74
6.3.1	Characterising the coherence of the beamline I10 at Diamond . .	74
6.3.2	Qualitative time dependence of the speckle pattern	78
6.3.3	Quantitative analysis of the temperature dependence of g_2 function	81
6.3.4	Interpretation of the observed Vogel-Fulcher behaviour	84
6.4	Conclusions	89
7	Nanomagnetic field-driven thermal mobility in artificial spin ice	91
7.1	Introduction	92
7.1.1	Experimental set-up	92
7.2	Thermal behaviour at room temperature using field-modified barrier height	93
7.3	Application of temperature with on-membrane heating	94
7.4	Reversal as a function of temperature	95
7.4.1	Hysteresis	95
7.4.2	Vertex populations	99
7.5	Injection and avalanche dynamics	100
7.6	Role of interaction in drift experiments	107
7.7	Conclusions	109
8	Summary and Outlook	110
8.1	Summary and conclusions	111
8.2	Future Work	112
	References	114

CHAPTER 1

Introduction

1.1 Overview

Over the past decade, the research into a new species of magnetic meta-material has mushroomed into a fully-fledged field in its own right. These new materials are called Artificial Spin Ices (ASIs) and consist of a geometric arrangement of nanoscale magnetic islands. The inter-island distances are chosen so that they are strongly interacting and exhibit frustration phenomena. Frustration usually arises when there is no way to completely minimise the total energy of the system. This is caused by different neighbouring interactions being in competition. Frustration is ubiquitous in physical systems and spans many areas, including granular matter [1], polymer gels [2], the stripe patterns of high temperature superconductors [3] and protein folding [4] to name but a few. If a system has no singular ground state (GS) this can lead to a violation of the third law of thermodynamics, which manifests as a residual entropy at absolute zero. This property is emblematic of the most common form of water ice, Ice I_h, and was explicitly shown by Pauling in the 1930s [5].

It was then realised that some of the low-temperature signatures of the rare-earth pyrochlore crystals were very similar to those of ice. They appeared to be a magnetic analogue and for that reason they became known as ‘spin ice’ [6]. In these systems, the minimisation of the magnetostatic interactions is analogous to that of the electrostatic interactions between the hydrogen ions of the H₂O molecule (as shown in figure 1.1(a)) and it is the spin orientation which shows frustration as opposed to the distribution of electric charge (figure 1.1(b)). Being able to measure these samples is a non-trivial task as the temperature at which thermodynamics become relevant are in the <1 K range and no real direct measurement of the atomic microstates can be made.

It was Wang *et al.* who first demonstrated artificial analogues of these systems using new nanofabrication tools, whose microstates could be directly inspected via magnetic force microscopy (MFM), a relatively simple and widely-available instrument [7]. The artificial systems, contrary to the three-dimensional natural spin ices and water ice, are two-dimensional and their geometry and strength of interaction can be designed with ease using nanofabrication software. The constituent islands act like small bar magnets whose magnetic moment can only be oriented in one of two ways and, as such, mimic a giant atomic spin. When arranged on a lattice, the place where more than one nanomagnet meets is called a vertex. It is a well-defined point of frustration as there is more than one way to arrange the nanomagnetic moments in order to minimise the

energy of the vertex. The focus of this research will be on the square geometry where four islands meet (see figure 1.1(c)). The vertex energy is also minimised when they obey the ‘ice rule’, *i.e.* two poles point in and two poles point out like water ice.

However, the primary interest in ASIs lay in the attainment of true thermodynamics in order to better understand the thermal and emergent behaviour of the systems for which they were invented to model. At first, the size of these islands were made large enough to image with MFM, with the smallest lateral dimension ~ 100 nm and thicknesses ≈ 30 nm, which will be referred to as the standard island size. At these sizes with a typical magnetic material such as NiFe (also known as permalloy or Py), they are too large to perturb with room temperature as the relevant thermal energy scale to observe dynamics requires $T > 10^4$ K. However, this is not strictly the case as the magnetisation, and therefore barrier, can be reduced close to the Curie temperature, which for Py (860 K) is still quite impractical. Alternatively, the islands can be made ultra thin (≈ 3 nm) and a less perturbing method, such as X-ray Photo-Emission Electron Microscopy (X-PEEM), can be used to image the states [8]. However, for the standard size islands, where MFM was suitable to measure the microstates of the system, rotating-field AC demagnetisation experiments were carried out as an attempt to randomise and obtain long-range order in these systems [7]. There was limited success, with short-range order and locally obeying ice-rule vertices, but no long-range order observed [9–12]. These large island systems were ‘jammed’ and in order to access real thermodynamics the field moved towards reducing the island moment; either by changing the material or reducing their volume. A reliable representation of the magnetic state of the less magnetic islands was difficult to measure due to their reduced signal, fluctuating nature and the sample-probe interaction perturbing the states of the ASI. Also, the timescales involved in MFM are very slow and limit the sensitivity to the dynamic changes. The technique was, therefore, not well suited to the task.

X-rays which have wavelengths similar to the lengthscales involved ($\lambda \sim \text{nm}$) and can be tuned to atomic resonances of magnetic materials, presented a possibility to measure the smaller magnetic moment of the islands of thermal ASI. Specifically, X-PEEM achieved great success, demonstrating dynamics in real-time with the opportunity to track vertex states with the system in a thermal state [8; 13–15]. There have also been two examples of magnetic scattering athermal [16] and thermal [17] square ASI. Two novel X-ray methods are further demonstrated in this thesis to measure the

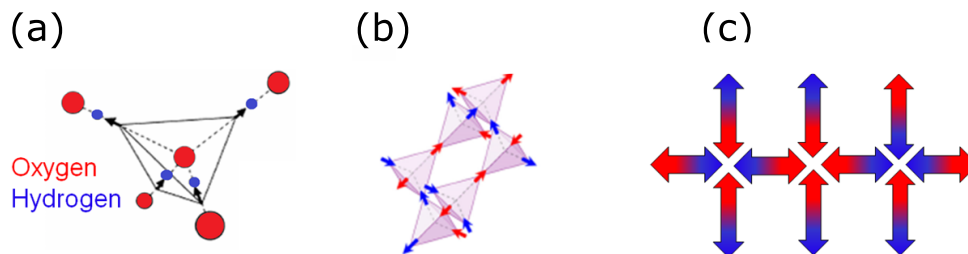


Figure 1.1: (a) Proton arrangement in water ice obeying the “two-in, two-out” ice rule. (b) The corner linked tetrahedra of the pyrochlore spin ice structure where the arrows represent the Ising-like atomic rare-earth spins. (c) The artificial square ice structure showing the macro-spin of each island meeting at a vertex with three others. (a) adapted from [18] and (b) after Jaubert *et al.* [19]

individual microstates of dynamic ASI.

Firstly, in Chapter 6, a completely new technique in the field, X-ray photon correlation spectroscopy (XPCS), has been developed using third generation synchrotron X-rays to probe the real and reciprocal space properties of small volume ASI. We have been able to characterise the dynamics of ASI, which are too small to measure with any current magnetic microscopy technique whilst maintaining sensitivity to individual microstates. We have shown that the low temperature behaviour is well-described by a Vogel-Fulcher law and that the reversal properties of the islands lead to a lower than expected activation temperature.

Secondly, in Chapter 7 thermal activation has been observed using transmission X-ray microscopy (TXM) where propagation of monopole excitations via strings has been demonstrated at different temperatures and propagation fields. Drift experiments have been performed and higher monopole velocities observed for more strongly interacting arrays, as well as at higher temperatures.

Chapter 5 gives some insight into the magnetometry of these systems as a function of temperature and will be shown to be a useful tool for characterising dynamic ASI.

Chapter 2 will contain a brief literature review, whose aim is not to be exhaustive but to set out the current state-of-the-art in the field and therefore the place of this work within it. Chapter 3 will introduce some key concepts related to magnetism and X-rays, as both the main techniques used in this thesis rely on their interaction and resultant

properties. Chapter 4 will go on to detail the nanofabrication processes used and other topographic characterisation of the samples. Finally, Chapter 8 draws together all the main conclusions of this thesis and will discuss possible future directions in the field and further progress that can be made with the present work.

The goal of the remainder of this chapter will be to introduce the relevant nanomagnetic theory and provide a basis to understand the experimental results of the literature and also those presented in this thesis.

1.2 Nanomagnetic behaviour

1.2.1 Single Domain Nanomagnetism

Ferromagnetic materials often have no net magnetisation in zero applied field which, at first, may seem counter-intuitive. The exchange energy of ferromagnetic systems dictates that all atomic spins should be aligned within a sample. It is induced by the Coulombic electrostatic interaction between neighbouring electrons. It is defined by the energy term, $E_{ex} = -2 \sum J_{ij} \mathbf{S}_i \cdot \mathbf{S}_j$, where J is the exchange integral and links the electron i with spin, \mathbf{S}_i to the electron j with spin, \mathbf{S}_j . A positive J dictates ferromagnetic alignment whilst a negative value leads to anti-ferromagnetic alignment. However, in bulk materials there is a way to minimise energy costs further by arranging the moments such that all magnetic moments are not aligned completely with each other but with small areas of surrounding neighbour spins. These areas are called domains and act to reduce the stray field outside of the solid. This energy minimisation can be understood if we consider the total magnetic flux density, \mathbf{B} :

$$\mathbf{B} = \mu_0(\mathbf{H} + \mathbf{M}). \quad (1.1)$$

As the magnetisation, \mathbf{M} , is a property of the solid it must be zero outside the solid in free space. Inside the magnet the \mathbf{B} and \mathbf{H} field are opposed to each other and \mathbf{H} is called the demagnetising field, \mathbf{H}_D . Whereas in free space $\mathbf{B} = \mu_0 \mathbf{H}$ where μ_0 is the permeability of free space ($= 4\pi \times 10^{-7}$). This change of direction of the field at the surface creates what looks like sources and sinks, or magnetic charges. The field created by these charges is called the stray field (indicated by the blue lines in figure 1.2). The potential energy of a magnetic solid can be written in terms of the demagnetising field and is calculated for each point in the material and summed over the total volume.

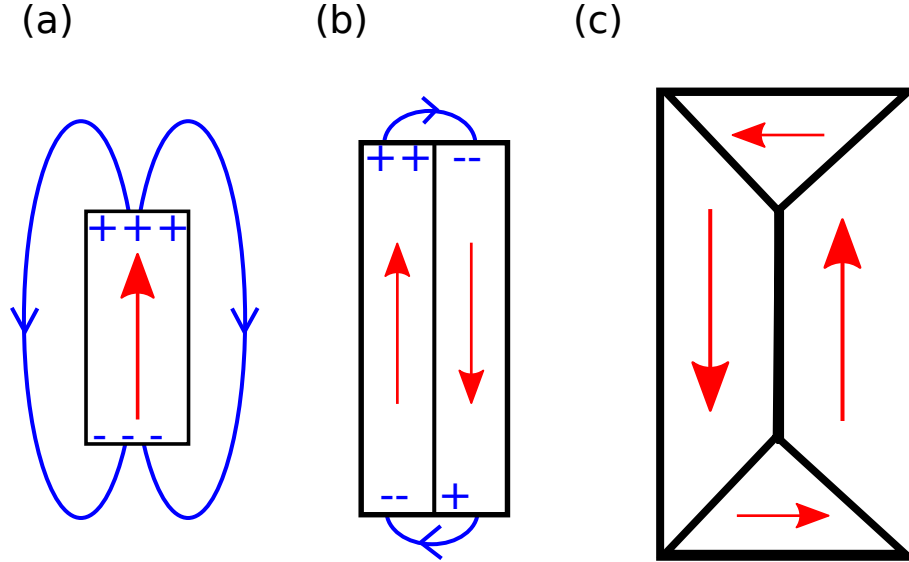


Figure 1.2: A schematic to show the energy saving in creating domains in ferromagnetic objects as you increase the size. (a) Shows how a small object (< 100 nm) will behave as a single domain will have a large stray field outside of itself, whereas, (b) shows the reduction of the stray field by having two or more domains in larger objects (≈ 100 nm). (c) Shows the energy can be further minimised by splitting into smaller perpendicular domains at the ends, allowing flux closure, so that there is almost no stray field outside of the object. Magnetisation is indicated by red arrows and the stray field by blue arrows. Positive and negative effective magnetic charges are also indicated in blue.

This is called the demagnetising energy:

$$\epsilon_{\text{demag}} = -\frac{\mu_0}{2} \int_{\text{sample}} \mathbf{M} \cdot \mathbf{H}_D dV \quad (1.2)$$

Therefore by arranging domains of magnetisation oriented in opposite directions, they will contribute opposite signs, $\pm \mathbf{M}$, to this energy and summing them reduces the energy. This energy saving is shown as a reduction of stray field outside of the object in figure 1.2 (b) and (c). The different regions are separated by domain walls which also have an associated energy cost and as the size of the nanomagnet is reduced at some point this outweighs any saving in demagnetising energy. Therefore, for small nanoparticles below a few 100 nm [20], they behave as one giant spin as the exchange energy locks all the atomic spins parallel to each other, creating a single domain “macrospin”.

1.2.2 Anisotropy and the Stoner-Wohlfarth Model

In magnetism, anisotropy is a direction-dependent property of a material which defines one or more preferred directions for the magnetisation vector to lie in. There are broadly three categories: shape, magnetocrystalline and induced anisotropy. Shape anisotropy arises from the minimisation of the demagnetising energy of the system, as discussed in the previous section. Magnetocrystalline is often found in bulk or epitaxial materials and depends on the symmetry of the lattice. The direction of lowest energy will usually be along a principal crystal axis. Induced anisotropy can be set during deposition, where an applied magnetic field creates a preferred axis. Also, external stress or strain can induce what is referred to as magnetoelastic anisotropy. Magnetoelastic effects are greatest for crystalline materials as it is a distortion of the crystal field which controls the magnitude of the effect [21].

Polycrystalline materials have very low magnetocrystalline anisotropy, which means the shape anisotropy can dominate. The shape anisotropy term arises from a desire to minimise the stray field outside of the sample, as previously discussed and shown in figure 1.2. The difference in energy for aligning the magnetisation along a preferred axis can be expressed using the demagnetising factor, N_D . This is a tensor which accounts for the geometry of the field which is set up in order to counteract the broken symmetry at the surface of a sample. This field is expressed as, $\mathbf{H}_D = -N_D \mathbf{M}$ and is known as the demagnetising field. Ellipsoids are an example of a simplified case where N_D is actually a scalar. An ellipsoid can be defined by its axes where a is the longest length, b is the width and c is the height i.e. $a \geq b \geq c$ (see figure 1.3). Using the different ratios of the axes N_D can be calculated (here the reader is referred to the paper by Osborn for details of the complete calculation and tabulated results [22]).

It is the shape anisotropy of the nanomagnets of this thesis which is heavily relied on to create the required Ising-like states. A general rule was applied to all fabricated nano-islands contained in this thesis, so that $N_D < 0.1$ in the a -direction, which required $\cong a/b > 2$. This means the magnetic moment of the island in the ASI is confined to point in either the positive or negative direction along its length. These two well defined energy minima form the macroscopic analogue to the ‘Ising’ spin - which they attempt to mimic. The general property is called uniaxial anisotropy and its angular dependence can be represented in energy by:

$$E = K_1 V \sin^2(\theta) + K_2 V \sin^4(\theta) + \dots \quad (1.3)$$

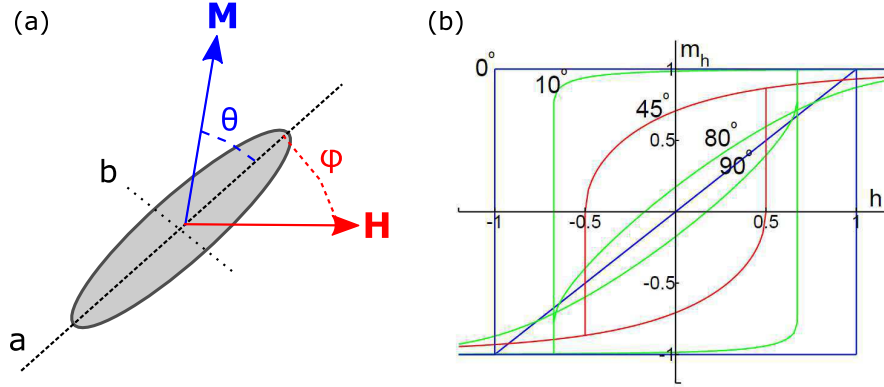


Figure 1.3: (a) An ellipsoid with longest length, a , and its magnetic moment direction defined using angle θ . The direction of the applied magnetic field, H , with respect to the a -axis is defined using the angle ϕ . (b) The Stoner-Wohlfarth model predicts the M-H curves shown on the right (schematic modified from [25]) where the values for ϕ have been labelled. At 0 degrees the field is in the direction of the easy axis of the particle (along the a -axis) and at 90 degrees it is perpendicular (along the b -axis).

Here θ is the angle between the magnetisation and the preferred axis of the particle, as shown in 1.3(a) and K_1 and K_2 are the first order and second order anisotropy constants. In most easy-axis cases such as the elongated ferromagnetic particles described here, higher orders of K are negligible in comparison to K_1 and only have significant contributions in more complex systems such as those with an easy cone anisotropy, for example [23]. Therefore, only the first order term of the anisotropy will be considered and will be now referred to as K . The response of uniaxial systems to a magnetic field at certain angles is well described by the Stoner-Wohlfarth model [24]. If we also now define ϕ as the angle from the a -axis to the applied field, then the energy of the system can be described as:

$$E = KV \sin^2(\phi - \theta) - \mu H \cos \phi, \quad (1.4)$$

where K is dominated by the shape anisotropy and $= \frac{1}{2}\mu_0 N_D M_s^2$ and μ is the size of the magnetic moment of the particle. This function gives the expected result that for $\theta = 0, \pi$, the energy is minimum, defining the a axis as the “easy” axis of the particle. The theory can be used to predict the behaviour under different angles of applied field, as shown in figure 1.3(b). The main features are decreased coercivity and remanence as the angle is increased away from the easy axis, with the minimal values at $\theta = \pi/2$ described as the “hard axis”.

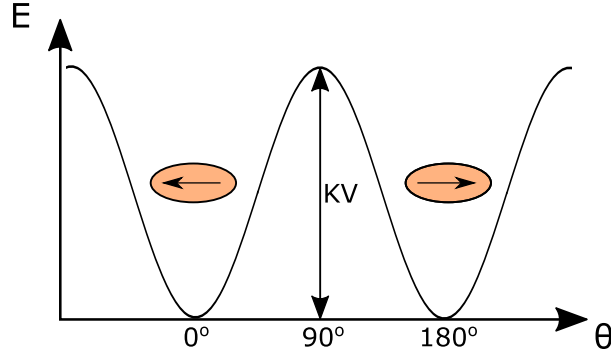


Figure 1.4: This schematic shows the separation of the two low energy states of the elongated island separated by the energy barrier KV . This can be overcome with sufficient thermal energy and cause the island to flip between the two stable states.

1.2.3 Zero-field thermal reversal and superparamagnetism

As previously mentioned, the goal of this thesis is to try to thermalise these macro spins. We can consider the energy required to reverse the island moment with temperature rather than with magnetic field. If the energy barrier due to the magnetic anisotropy of a particle can be overcome by the thermal energy available in the system, it will fluctuate between its bistable lowest energy states. In the case of an elongated particle with uniaxial anisotropy, the energy barrier to reverse the magnetisation direction is equal to the product of its shape anisotropy and its volume, $\Delta E = KV$. This is shown in figure 1.4 where the two low energy states have the macrospin aligned along the long axis and can point to the left or to the right. The energy available from the environment can be defined as, $E = k_B T$, where k_B is Boltzmann's constant. Néel [26] and Brown [27] found that the probability or rate of flipping, τ^{-1} , is linked to the ratio of the two energies in the following way:

$$\tau^{-1} = f_0 \exp(-KV/k_B T). \quad (1.5)$$

where f_0 is the attempt frequency and typically taken as 1-10 GHz is related to the gyromagnetic precession [26]. Therefore, if you attempt to measure the magnetisation in a time frame much slower than τ , the magnetisation will average to zero and hence the remanence will disappear and the particles are said to be superparamagnetic (SPM).

If you were to apply a field to a group of these particles and measure their hysteresis this would be related to the ratio $\frac{\tau}{t}$, where τ is again the relaxation time from saturation to thermodynamic equilibrium and t is the time after removing the field. If the system

has reached thermodynamic equilibrium and the applied field is zero, the magnetisation of the group of islands should also be zero, i.e. there will be no remanence. This can be expressed as:

$$M_{R,t}/M_{R,0} = \exp(-t/\tau). \quad (1.6)$$

This is a simple example of magnetic viscosity and can be used to probe the relaxation time of the sample. Often an experimental time frame is considered, for example if we assume a measurement time of 30 seconds (*i.e.* $\tau = 30$ s), then eq. 1.5 gives an upper limit on the superparamagnetic volume, V_{sp} :

$$V_{\text{sp}} = 25k_B T/K. \quad (1.7)$$

However, due to the exponential dependence the remanence will vary significantly with small changes in particle volume and the distribution in volume will give a distribution in switching fields. It is therefore more accurate to describe a superposition of exponentials for a group of particles. The decay of the magnetisation in the presence of a field can be approximated as a linear dependence on a logarithm of time [28]. Sharrock derived an equation to describe how the coercivity changes with measurement time in terms of thermally assisted barrier crossing, it assumes $\tau \gg t$ and comes from substituting a field-assisted barrier, $E_{\text{barrier}} = KV(1 - \frac{H}{H_0})^n$ for KV into eq. 1.5 [29]:

$$H_c(t) = H_0\{1 - [(k_B T/KV) \ln(f_0 t)]^n\}, \quad (1.8)$$

where n is an exponent dependent on the angle between the field direction and the easy axis of the particle, and $H_0 = 2K/M$ is a field independent measure of the coercivity or the anisotropy field.

1.2.4 Dipolar interaction and Frustration

The ideas discussed so far have not incorporated inter-particle interactions and how they may play a role in the thermodynamic behaviour of an ensemble of nanomagnets. It turns out the dipolar interaction has a large effect on the simple Néel-Brown model. Firstly, let's consider that two particles with magnetic moment μ_1 and μ_2 and a separation r , they have the magnetostatic potential energy [31]:

$$E = \frac{\mu_0}{4r^3} \left[\boldsymbol{\mu}_1 \cdot \boldsymbol{\mu}_2 - \frac{3}{r^2} (\boldsymbol{\mu}_1 \cdot \mathbf{r})(\boldsymbol{\mu}_2 \cdot \mathbf{r}) \right]. \quad (1.9)$$

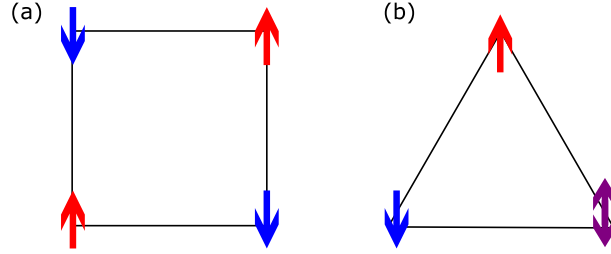


Figure 1.5: (a) It is possible to satisfy all nearest-neighbour interactions on the square lattice for antiferromagnetic coupling, with its even number of coupling. (b) For the triangular lattice one nearest-neighbour can be satisfied but there will always be an unfavourable interaction with another, leading to frustration, due to the odd coupling number.

This energy is minimised when the μ_1 and μ_2 are aligned with their poles north to south (or head-to-tail). Placing magnetic moments on a lattice, as shown in figure 1.5 leads to frustration. Each neighbour will want to anti-align to its neighbour; the square lattice can satisfy all nearest neighbour interactions but the second nearest neighbour is frustrated. Whereas for the triangular lattice after placing two magnetic moments on two of the corners and satisfying their interaction, the third moment can be oriented in either direction without altering the total energy of the system. Therefore, one nearest neighbour interaction can be satisfied but the other will always be frustrated.

When dipolar interactions are incorporated into superparamagnetism, there is a correction to the energy barrier which depends on the strength of interaction [32; 33]:

$$KV \rightarrow KV + J_{NN}, \quad (1.10)$$

where KV is acting to align the magnet to its easy axis and J_{NN} is the nearest neighbour interaction energy, which can be either positive or negative depending on the exact starting configuration. This is essentially a similar method employed by Sharrock in eq. 1.8, although the modification was by applied field rather than the field of neighbouring nanomagnets. The idea of the modification in eq. 1.10 is that the individual barrier of the particle is modified by the total free energy of the assembly. This means that the reversal of one particle acts to change the individual energy barriers of all the other particles in the assembly.

An interesting example of how the barrier can be increased and ferromagnetism recovered is shown in the work of Cowburn et al. [30]. They defined their arrays of circular nanomagnets using electron beam lithography, the nanomagnets were 60 nm

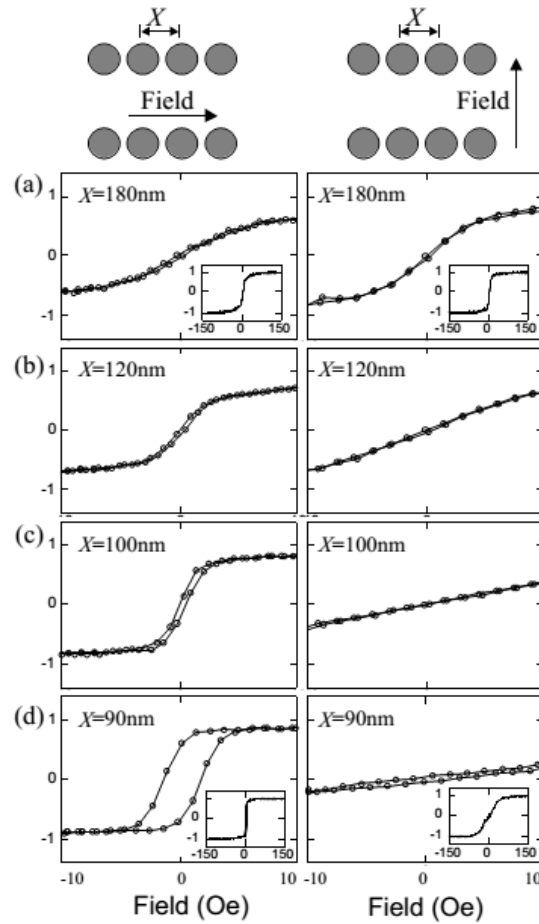


Figure 1.6: Experimental MOKE measurements of arrays of circular nanomagnets reproduced from ref. [30]. Panel (a) shows the superparamagnetic response in both the X and Y direction as the nanomagnets are non-interacting. As the nanomagnets are pushed closer together in the X direction, ferromagnetism is restored. This is demonstrated by the increasing coercivity with decreasing separation from (b) to (d) and there is a less pronounced change for the hysteresis loops taken in the Y direction.

in diameter and 7 nm thick. In order to investigate the role of dipolar interaction between the islands they arranged the array with a constant separation along the y -axis of 180 nm and varied the separation in x between 180 and 90 nm, as shown in the top of figure 1.6. They then used focussed MOKE to study the impact of moving the nanomagnets closer together. For the largest spacing, the hysteresis loops are of the Langevin functional form and display characteristic SPM properties i.e. zero coercivity and small remanent magnetisation. As they illuminated many thousands of nanomagnets at once within the micron-sized laser spot they treat the averaged behaviour as representative of a single nanomagnet, which is similar to previous studies [34; 35]. By reducing the separation in x they increased the interaction between the nanomagnets and observed increased magnetic ordering in the x direction [36], evidenced by an increase in M_R and H_c . This is rightly pointed out as being in direct analogy to the onset of ferromagnetism from paramagnetism on the atomic scale. However, the driving force here is the magnetostatic energy rather than the exchange energy.

CHAPTER 2

Literature Review

2.1 Water and spin ice

The original paradigm of frustration, water ice, arose from the competing interactions of the local bonding in the molecule and the symmetry of its crystal lattice. As shown in figure 1.1(a), each oxygen atom has four neighbouring hydrogen atoms where two are classed as near and are covalently bonded and two are further away belonging to neighbouring molecules and are hydrogen-bonded. This compromise of ‘two-in/two-out’ has been dubbed the Bernal-Fowler ‘ice-rule’ and is the ground state (GS) configuration [37]. Although the ‘ice rule’ is obeyed locally, as the size of the sample increases, the number of equivalent proton arrangements grows exponentially, yielding a macroscopically degenerate GS of the sample. It was Pauling, in 1939, who predicted this would manifest itself as a non-zero entropy, specifically $S = \frac{R}{2} \ln(3/2)$ [5], this violation of the third law of thermodynamics was confirmed by heat capacity measurements the following year [38].

The spin ice materials also exhibit this characteristic value of residual entropy, which was confirmed experimentally by Ramirez *et al.* in 1999 [39]. Common examples of the pyrochlore materials include the $\text{Dy}_2\text{Ti}_2\text{O}_7$ and $\text{Ho}_2\text{Ti}_2\text{O}_7$ whose structure is shown in figure 1.1(b) [6; 39; 40]. These crystals are built up of corner-sharing tetrahedra which are occupied by rare earth magnetic ions (Dy^{3+} or Ho^{3+}). These ions carry spins which, due to strong anisotropy from the crystal field interactions, are confined to the [111] axes and can either point into or out of the tetrahedra, and are therefore Ising in nature. They offer a playground to explore exotic excitations; for instance when the ice rule is obeyed a tetrahedron will have no overall moment, however if thermal excitation flips one of the spins, Castelnovo *et al.* predicted that the “3-in/1-out” vertex excitation would have interesting properties and coined the term ‘emergent monopole’ [33]. These excitations are produced in monopole-antimonopole pairs and diffuse away from each other in order to reduce the energy cost of the excitation itself. The chain of flipped spins left in its wake can be likened to the theoretical construct of flux channels known as ‘Dirac strings’ [41], which is highlighted in white in figure 2.1. These excitations can be manipulated with an external field much like electrons with electric fields, leading to the comparative term ‘magneticity’ [42; 43].

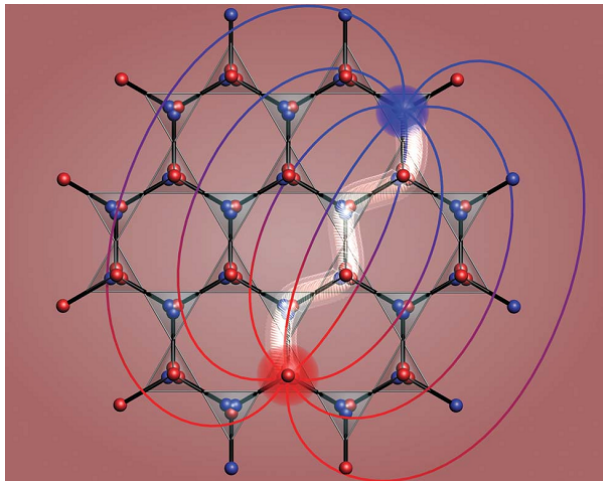


Figure 2.1: Sketch of a spin ice pyrochlore lattice where a monopole-antimonopole pair have been created and have separated via a string of flipped spins highlighted in white. The corresponding field lines from the monopole excitations are also shown (after Castelnovo *et al.* [33]).

2.2 Artificial Spin Ice (ASI) in the athermal limit

2.2.1 The square geometry

A square ASI is where four nanomagnets meet at each vertex of a lattice and the different vertex arrangements are shown in figure 2.2(a). There are $2^4 = 16$ possible vertex configurations which can be grouped by energy, indicated by the different dotted boxes in the figure. In order to obey the ‘two-in/two-out’ ice rule, the vertex can be arranged in six different ways, which are shown as Type-1 (T_1) and Type-2 (T_2) in the figure. The square vertex has an inequivalence in its pair-wise interactions, since the distance between perpendicular islands is smaller than that between parallel ones. This leads to an energy saving by having the perpendicular (closer) islands head-to-tail and the more costly interaction of head-to-head for the parallel (further) islands. This T_1 arrangement has the minimum energy and a checker-board tiling of the two T_1 vertices, shown in figure 2.2(b), defines the GS of the system. This is an important difference compared with the pyrochlore spin ice where the 6 possible ice-rule configurations on the tetrahedra are energetically equivalent leading to a large GS degeneracy. T_2 vertices have slightly higher energy due to this smaller distance between perpendicular

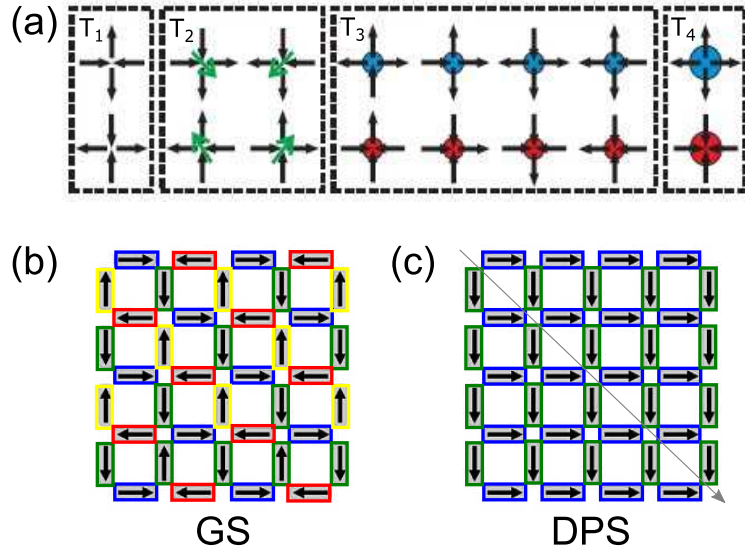


Figure 2.2: (a) The sixteen possible vertex configurations of square artificial spin ice, grouped by vertex energy increasing from 1 to 4. The Type-1 and 2 vertices obey the ice rule, where two poles point in and two point out. Type-1 have the lowest energy as they are magnetically charge neutral. Type-2 are also neutral but possess a dipole moment indicated by the green arrow. The Type-3 and 4 are monopole-like magnetic charges (differing polarities indicated by the blue and red colour). The bigger circle of Type-4 indicates the double charge, $\pm 4q$ of the vertex (diagram modified from ref. [44]). (b) The checker-board tiling of the T_1 vertices constitutes the ground state (GS) arrangement. (c) A diagonally polarised state (DPS) consisting of all of the same T_2 vertices with the applied field direction indicated by the grey arrow.

2.2 Artificial Spin Ice (ASI) in the athermal limit

neighbours. The vertex has a resultant magnetic moment in the direction shown by the green arrows in the figure. If a magnetic field is applied along the diagonal of the islands a diagonally polarised state (DPS) can be made as indicated in figure 2.2(c). For the experiments of chapter 7, this DPS is the initial state of the system. The Type-3 (T_3) vertices have a degeneracy of 8 and arise from a violation of an ice-rule vertex, where one nanomagnet has been flipped. Each nanomagnet can be thought of as dumbbell-like contributing a north or south pole, each of charge q , to the vertex centre. If one sums these when there is an uncompensated pole at the vertex, it is said to possess charge. For the T_3 vertex this equals $\pm 2q$. The most energetically-costly excitation is Type-4 (T_4) where all four nanomagnets meet head-to-head (or tail-to-tail) and carry $\pm 4q$.

Both water and pyrochlore spin ice involve atomic-scale interactions and the direct inspection of the microstates of the system is not possible with current experimental techniques. As previously mentioned, in 2006 a group at Pennsylvania State first fabricated an analogous system on a mesoscopic scale, making use of electron beam lithography and the single domain nature of nanomagnets [7]. They fabricated nanomagnets arranged on a 2D square lattice such as that shown in figure 2.3(a). They noted that all vertex types were populated with slightly more low energy T_1 and T_2 vertices than expected for a random distribution. This proportion increased as the interaction (lattice spacing) was increased (decreased). In their samples they observed short-range ice-rule order, however they did not see any long range correlation in their samples. Since then many other studies have extended this idea to different geometries and materials.

2.2.2 The kagome geometry

One such system is the kagome structure, where the magnets are arranged in a hexagonal pattern with three poles meeting at each vertex, as shown in figure 2.3(b). This uneven vertex number is in contrast to that of the square ice and leads to increased frustration as now all the interactions are of equal strength. There are $2^3=8$ possible vertex types, six of which obey the pseudo-ice rule vertex of two-in/1-out and have an overall charge, $\pm q$ and there are two higher energy states where all moments point in or out with $\pm 2q$. This means all vertices are magnetically charged and although, theoretically there is a ground state which is both spin and charge-ordered [46], it remained experimentally elusive before samples could be thermally annealed [47; 48]. Connected arrays of

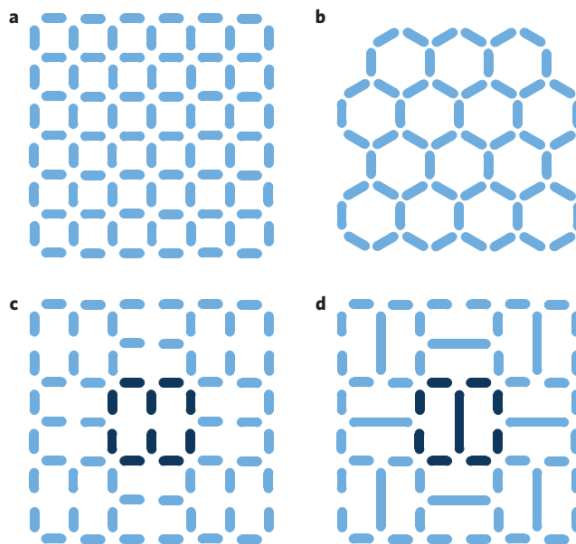


Figure 2.3: Some of the different geometries so far explored experimentally including (a) square, (b) kagome and both the (c) short-island and (d) long-island Shakti lattices. After ref. [45].

kagome structures have shown that, locally, ice-rules are obeyed and have displayed long-range disorder through imaging via Lorentz-transmission electron microscopy (L-TEM) [11; 49].

Disconnected arrays have also been studied with reversal propagation occurring via string excitations, as will be demonstrated in the following section [32]. There are four phases of the kagome ice; at high temperatures they are superparamagnetic and there are ice-rule obeying vertices as well as higher energy vertices. On cooling and increasing interaction strength the kagome ASI can order into strictly ice-rule obeying states and this is known as the ice-I (K1) phase. Upon further cooling the vertices can display charge order where each negative vertex is surrounded by positive vertices and vice versa, known as the ice-II (K2) phase. A high degree of charge order has been demonstrated recently with domain sizes which are controlled by the lattice spacing [47; 48]. This phase can still show only partial order and the real lowest entropy state is that of the K3 phase, which is fully loop ordered [50].

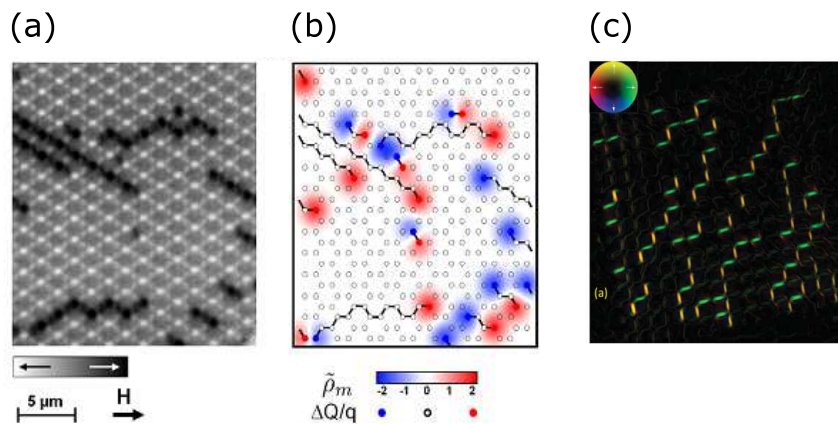


Figure 2.4: (a) A PEEM contrast image of a kagome lattice, mid-reversal and (b) the corresponding charge density map associated with the emergent monopole excitations and their associated Dirac strings (black chains) connecting them (after ref. [32]). (c) A similar behaviour has been shown in the reversal of the square geometry with L-TEM contrast shown in the top right of the image. For the square geometry branching events were observed (after ref. [51]).

2.2.3 Emergent monopoles and the flow of magnetic charge

These artificial systems have harboured the predicted emergent monopole excitations and the flow of magnetic charge has been reported via MFM in kagome [52], and Lorentz TEM in square artificial spin ice [51]. Mengotti *et al.* have studied their creation and propagation in kagome structures using X-PEEM [32]. During the magnetic reversal of the system, the monopoles were imaged propagating along 1D chains of reversed islands through the array and were likened to the theoretical Dirac strings. This is shown in figure 2.4(a) and (b), along with the work of Pollard *et al.* on the square geometry shown in (c). Due to the energetics of the system the Dirac strings in square ice are actually better described by Nambu strings, as they are connected by T2 vertices with a finite string ‘tension’, their energy defined as $E(T_2) - E(T_1)$ [53]. In the kagome ice due to the full degeneracy of the system they are better described as tensionless Dirac strings [54]. It is important to note that all of these studies have been athermal and used magnetic fields to induce the dynamics. The islands have had large volumes, requiring thermal energies $\approx 10^3$ K / k_B in order to flip the magnetic moment and have been “jammed”. The demagnetising field protocol employed to randomise the system introduces effective thermodynamics and the specific properties of the field ramp have been used to define an effective temperature of the system [55–57]. The extension of

this to describe an effective entropy has also been reported [58; 59].

2.3 Thermal measurements of ASI

There have been recent demonstrations of true thermodynamics in ASI systems using several different approaches. Morgan et al. were the first to demonstrate a thermal system and long range ground state order in square ASI [44]. This was achieved during fabrication when the islands had a smaller volume during the initial stages of growth of the magnetic material. As the islands continue to grow so does their energy barrier to reversal. This is a one-shot approach, as once the islands have been fully deposited the order is frozen in. Other groups have since shown it is possible to heat large islands in a vacuum close to the ordering temperature of the material and on subsequent cooling they have obtained arrested thermalised states, which are imaged using MFM [47; 60]. They obtained long range order in square and kagome geometries but also a more complex geometry known as a Shakti lattice (see figure 2.3(d)) [45]. Long-range order over an entire sample, as has been observed in the square geometry [8; 48], has not been seen in the kagome geometry. However, these approaches still involve large enough islands to image in an MFM and it is not possible to study the dynamics in real-time.

As the energy barrier to reversal is dependent on the magnetisation and the volume it is possible to decrease both of these parameters in order to access the dynamic regime. The first example of achieving this with a low magnetisation material was shown in 2012 by Kapaklis et al. [61]. They used δ -doped Pd(Fe), which had a low Curie temperature, $T_C = 230$ K, and demonstrated the so-called “melting” of their ASI. They used a macroscopic measurement, the magneto-optic Kerr effect (MOKE), to infer from the remanent magnetisation that ‘macro-spin order’ was lost more quickly for their patterned film, compared to a sheet film of the same material. They attributed this to the islands being able to thermally agitate at a temperature below T_C of the material, due to a lower energy barrier to reversal. More direct measurements have since been made using PEEM, a technique which has the required sensitivity and time resolution in order to study the dynamics as they proceed. Arnalds et al. first showed thermal experiments on the kagome geometry for one, two and three ring structures [13]. Another study where an extended sample was used they built up a theoretical model using the framework of hyper-cubic trajectories and demonstrated that the dipolar energy and

the complexity of the system affected the temporal and spatial exploration of its phase space [14]. Drisko *et al.* recently demonstrated PdFe₃ as another good candidate material with dynamic behaviour tuned to practical experimental temperatures, observing full GS-order in a square ASI and the highest reported charge-order in kagome ASI, using L-TEM[48].

The other route to dynamics is reducing the island size. This was expertly demonstrated by Farhan *et al.* who engineered a wedge sample and tuned the exact thickness in order to access appropriate dynamics [8]. They made Py ASI with areal dimensions of 470×170 nm and lattice spacing $a = 425$ nm and varied the thickness along the wedge, 0 - 20 nm. They were then able to image a large area ($20 \mu\text{m}$ area) with thickness 3 nm having the appropriate relaxation time of several hours for their measurement technique. Firstly, they applied a saturating magnetic field along the diagonal of their sample, creating all T₂ vertices in a DPS (see figure 2.2(c)). They then removed the field and allowed the sample to relax. One of the interesting conclusions of this study was that in order to simulate the observed relaxation rate from the experiment it was necessary to include disorder in their model (using Monte Carlo methods). If they did not do this, the relaxation was almost instantaneous. This correction to the theoretical model had previously been predicted by Budrikis *et al.* [62].

The opportunity to image these microstates and their time evolution directly, allows a comparative study with theory, including that of disorder [63] and out-of-equilibrium dynamics [64]. The ratio of the interaction and thermal energy controls the rate at which domains will grow, however, it has been shown that disorder also plays a vital role [65]. Budrikis *et al.* postulated that the intrinsic disorder of the patterning process of these systems can have a significant effect on the nucleation and reversal dynamics, consistent with findings in studies of nanomagnet arrays fabricated via block copolymer lithography [66]. Kohli *et al.* did an extensive magneto-optical study on square ASI and also showed that in order to obtain good agreement between their simulation and experiment, it was necessary to introduce island edge disorder into their model (estimated from SEM images) [67]. Many other studies have also used the disorder as a parameter to help fit the theoretical predictions with their experimental results [32; 48].

CHAPTER 3

X-rays and magnetism

3.1 Non-resonant X-ray scattering

An incident X-ray is scattered by the interaction of its electric field with an electron within the targeted material. The scattered photon can have the same energy as the incident photon and the process is elastic (Rayleigh scattering) or the energy of the scattered photon is different and the process is inelastic. The scattering vector, \mathbf{Q} , is defined in reciprocal space as:

$$\mathbf{Q} = \mathbf{k}_f - \mathbf{k}_i, \quad (3.1)$$

where \mathbf{k} is the X-ray wave vector and $f(i)$ denotes final(initial), λ is the wavelength of the light and $|k|$ is $2\pi/\lambda$. If $|k_i| = |k_f|$ the process is elastic. The smallest scattering unit in matter is the electron. Classically, the interaction can be described as the X-ray causing the single electron to vibrate which then acts as a small dipole antenna. One can evaluate the ratio of the radiated and incident field as:

$$\frac{E_r(R)}{E_{in}} = - \left(\frac{e^2}{4\pi\epsilon_0 mc^2} \right) \frac{e^{ikR}}{R} \cos \psi. \quad (3.2)$$

The spherical wave, $e^{i\mathbf{k}\cdot\mathbf{R}}/R$ is multiplied by a bracketed pre-factor which is defined as the Thomson scattering length, r_0 , and the negative sign here indicates that the radiated field is exactly π out of phase with the incident one. If you extend this picture to an atom where there are Z electrons with a specific number density, $\rho(\mathbf{r})$, the total atomic scattering length is:

$$f^0(\mathbf{Q}) = \int \rho(\mathbf{r}) e^{i\mathbf{Q}\cdot\mathbf{r}} d\mathbf{r}. \quad (3.3)$$

Here f^0 is the atomic scattering amplitude, also known as the atomic form factor. The integral is evaluated over each small volume $d\mathbf{r}$ element. In the limit $\mathbf{Q} \rightarrow 0$, all volume elements scatter in phase and the total number of electrons in the atom, Z , is recovered. As \mathbf{Q} increases different elements then scatter out of phase and as $\mathbf{Q} \rightarrow \infty$, $f^0 \rightarrow 0$ corresponding to when the wavelength, λ , becomes small relative to the atomic size. It is noted that the right hand side of this equation is a Fourier transform and therefore f^0 is actually the Fourier transform of the electron distribution in the sample. This can be used to define the probability of observing a scattered particle per unit solid angle, $d\Omega$, also known as the differential cross section:

$$\frac{d\sigma}{d\Omega} = |f|^2. \quad (3.4)$$

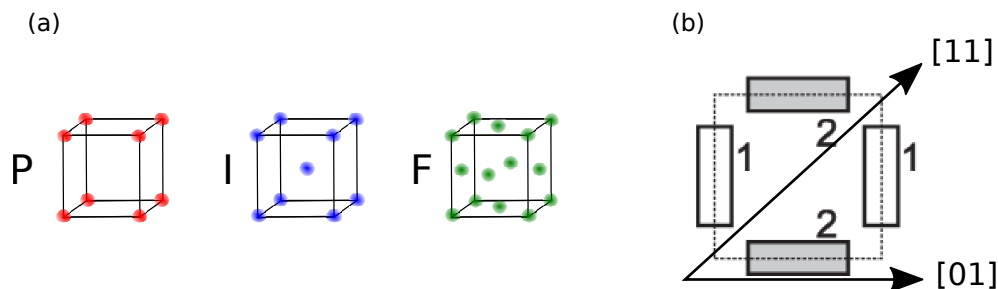


Figure 3.1: (a) A simple cubic unit cell labelled as P for the primitive unit cell, I is the body-centred cubic and F is face-centred. (b) The square artificial spin ice with its unit cell defined by the dotted line and $[01]$ and $[11]$ directions indicated. The square ASI can be broken down further into sublattices, highlighted here with different numbers 1 (white) and 2 (grey).

3.2 Bragg diffraction and the crystal lattice

A crystal is defined by its *unit cell*, this is the smallest constituent that it can be broken down into whilst retaining translational symmetry and periodicity (see figure 3.1(a)). Considering a crystal in three dimensions, the translation of the unit cell can be described by:

$$\mathbf{R}_n = n_1 \mathbf{a}_1 + n_2 \mathbf{a}_2 + n_3 \mathbf{a}_3, \quad (3.5)$$

where $n_{1,2,3}$ are integers and $\mathbf{a}_{1,2,3}$ are the lattice vectors. In the example of a simple cube in the figure they can be primitive, body-centred or face-centred with only one lattice point per unit cell. Otherwise they would be non-primitive. The basis is the species which is placed on the lattice to form the crystal and in the case of the square ASI the basis would be a pair of magnetic nanoislands, as shown in 3.1(b). In order to specify certain planes within a crystal we can use the Miller indices formalism. Considering a family of planes in a crystal, then the one nearest to the origin will have the intercept $(\frac{a_1}{h}, \frac{a_2}{k}, \frac{a_3}{l})$ on the axes $(\mathbf{a}_1, \mathbf{a}_2, \mathbf{a}_3)$. Considering the ASI which is a crystal in 2D, the $[10]$ and $[11]$ directions are defined as shown in figure 3.1(b). The spacing between planes, d , can be defined in terms of the lattice parameter, a , as:

$$d_{hkl} = \frac{a}{\sqrt{h^2 + k^2 + l^2}}. \quad (3.6)$$

When measuring diffraction from a crystal lattice it is this spacing, d_{hkl} , which is probed. This can be either chemical or magnetic so long as there is a repeating pattern of the electronic structure on a similar length-scale to the wavelength of the scattered

3.3 Magnetic enhancement at resonance

radiation. The condition for constructive interference of the waves in relation to the crystal lattice was actually first discovered at the University of Leeds, in 1913, through work of the father and son collaboration, W. H. Bragg and W. L. Bragg [68]. They would later win the Nobel prize for this discovery and it has become known as the eponymous Bragg's law:

$$n\lambda = 2d_{hkl} \sin \theta, \quad (3.7)$$

where n is the order of diffraction, λ is the wavelength of the radiation, d_{hkl} is the spacing between the lattice planes whose Miller indices are $[hkl]$ and θ is the angle made between the incident and diffracted beam and the hkl planes. The momentum transfer and wavelength of the X-ray are related by:

$$\mathbf{Q} = \frac{4\pi}{\lambda} \sin \theta. \quad (3.8)$$

Combining this with Bragg's law allows us to relate the position in reciprocal space of a first order diffraction peak ($n = 1$) and the real space lattice spacing as, $\mathbf{Q} = 2\pi/a$.

3.3 Magnetic enhancement at resonance

Quantum mechanically the electrons in atoms are in discrete energy levels and those in the K shell, closest to the nucleus, are the most tightly bound and happen to have binding energies similar to the energy of a typical X-ray photon ($\sim 1-10$ keV). Electrons in the L or M shell are less tightly bound and therefore can respond more closely to the external driving field of an incident X-ray. However, this is with the reduction in the scattering length by some factor f' [69]. If the X-ray energy is much higher than the binding energy, then $f' = 0$ and the electrons can be considered free. In between these limits resonant behaviour may be observable at element-specific absorption edges. The dissipative part of the process is defined by f'' and is closely related to the absorption. The atomic form factor can now be expressed, more completely, as the following,

$$f(\mathbf{Q}, E) = f(\mathbf{Q}, E) + f'(E) + f''(E). \quad (3.9)$$

The Q dependence has been omitted from the last two terms as these are related to core shells so do not have a appreciable dependence on Q and are largest at atomic resonant energies. The second term is proportional to the magnetic scattering and is usually around 10^6 times smaller than the charge scattering from the atom [70]. This

can be enhanced using the third resonant term, close to 1%, at an atomic absorption edge.

3.3.1 X-ray magnetic circular dichroism (XMCD)

When X-rays are incident upon a ferromagnetic sample their polarisation has an effect on their absorption and subsequent scattering. For the two different helicities of circularly polarised light, the X-ray absorption cross-section is strongly dependent on the orientation of the magnetisation in the direction of propagation of the photons for energies at an absorption edge; this property is known as X-ray magnetic circular dichroism (XMCD). The strongest effect is in ferromagnets at the L edge *i.e.* between the $2p$ and $3d$ states. The Fe and Co L_3 atomic resonance has the largest difference between the XMCD intensity for the two helicities of light due to the larger number of spin moments involved in the interaction (L_3 corresponds to the $2p_{3/2} \rightarrow 3d$).

The process can be considered as a two-step process. Firstly, there is the absorption of the photon by the bound electron, then there is the excitation of the electron in the $2p$ level, which is split in the presence of spin-orbit coupling. Due to conservation laws, the angular momentum of the X-ray photon is transferred to the angular momentum of the photo-excited electron. There are selection rules for the quantum numbers involved in the electronic transition, which are demonstrated in the simplified energy level picture in figure 3.2(a). Total angular momentum is defined as, $J = \sqrt{j(j+1)}\hbar$, where j is the total angular momentum quantum number and can take values, $j = l \pm s$, where l is the orbital momentum quantum number and s is the spin quantum number. The z -component of angular momentum is $L_z = m\hbar$, where m is the magnetic quantum number. The transition requires that $\Delta l = \pm 1$ and also that the total angular momentum is conserved. Right circularly polarised (RCP) light has $m = 1$ whilst left circularly polarised (LCP) light has $m = -1$. In figure 3.2(a), the final state is described by $|l, m\rangle$ indicated on the right-hand side of the diagram. Therefore, after the RCP photon transfers its angular momentum to the electron, the electron can only make a transition into the $2p$ level for $l = 1$ with $m = 1$ and there happens to be an empty state in $|1, 1\rangle$. The only allowed transition for the electron after LCP photon transfers its angular momentum is not possible as the $|1, -1\rangle$ is already occupied. This creates the imbalance in the transition probabilities that manifests macroscopically as the difference in absorption for different spin orientations.

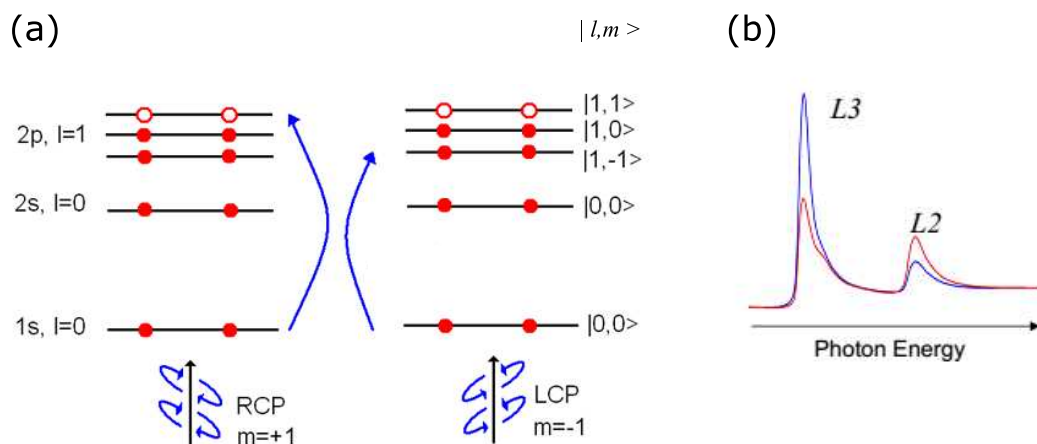


Figure 3.2: (a) Selection rules illustrating the difference in absorption for the two helicities of light. The transition, indicated by the blue arrow, requires conservation of J_z and $\Delta l = \pm 1$. Therefore, an electron which absorbs a left circularly polarised (LCP) photon, has its transition forbidden as the 2p level with $m=-1$ is already occupied. Whereas for the electron which absorbed an RCP photon, $l=-1$ is occupied but $l=1$ is empty and the transition is allowed (after ref [69]). (b) The energy spectra shows a large difference between the intensity for RCP X-rays (red) or LCP X-rays (blue), the same would be observed for positive or negative \mathbf{M} .

As the magnitude of the XMCD effect depends on the X-ray angular momentum $L_z \cdot \mathbf{M}$, it can be measured with a constant polarisation of light and a varied applied magnetic field to reverse \mathbf{M} or with constant applied field direction and varied helicity of the X-ray beam. They both manifest as a difference in the absorption energy spectra, as shown in figure 3.2(b).

3.3.2 X-ray resonant magnetic scattering (XRMS) and magnetic microscopy

XMCD only measures the imaginary part of the atomic resonant scattering factor, whereas XRMS measures both the real and imaginary part [72], the two processes are illustrated in figure 3.3. X-ray absorption directly measures the magnitude of f'' , as it is proportional to the X-ray absorption cross-section. This can be related to the magnetic part of the atomic form factor, f' , using the Kramers-Kronig relation [71]:

$$f'(E) = \frac{2}{\pi} P \int_0^\infty \frac{\epsilon f''(\epsilon)}{E^2 - \epsilon^2} d\epsilon. \quad (3.10)$$

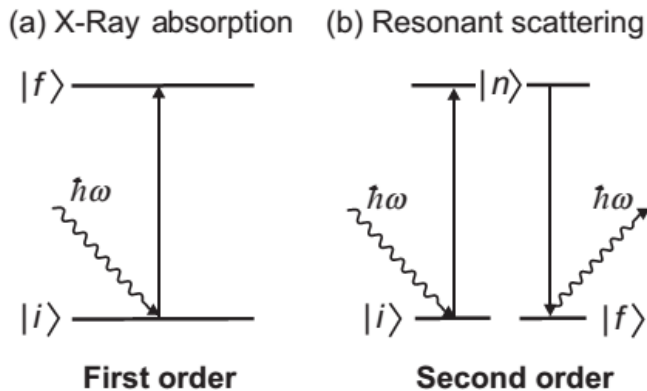


Figure 3.3: Resonant processes which can take place. (a) The absorption process as a first-order process where there is energy conservation between the initial and final state. (b) Resonant scattering involves the absorption of a photon but is related to the photon which is emitted after the photo-excited electron de-excites. It is a second-order process as the conservation is still between the initial and final state, however, intermediate or virtual states, n can be accessed without energy conservation (after ref. [71]).

The ‘ Pf ’ indicates the Cauchy principal value integral. This pure absorption signal can be measured directly via transmission X-ray microscopy (TXM), which we will see in the following chapter in section 4.4.1 and also in results chapter 7.

XMCD can also be made use of in X-PEEM where for soft X-ray energies there is a preference for an Auger decay process, where an electron is expelled and can be directly measured.

3.4 X-ray photon correlation spectroscopy (XPCS)

When coherent light is incident on a sample with disorder, the scattered light interferes and is broken up into bright and dark regions, originating from the phase shifts of the scattered waves between the different parts of the sample, this is known as a speckle and is shown in figure 3.4. This detail is averaged away for incoherent light. If the details of the speckle change over time then this means that the scattering objects are also changing with time and their relative phase shifts change. It is common to define the dynamics using the dynamical structure factor, $S(\mathbf{Q}, \omega)$ given by,

$$S(\mathbf{Q}, \omega) = \frac{1}{2\pi} \int_{-\infty}^{\infty} dt e^{i\omega t} \langle \rho(\mathbf{Q}, 0) \rho(-\mathbf{Q}, t) \rangle \quad (3.11)$$

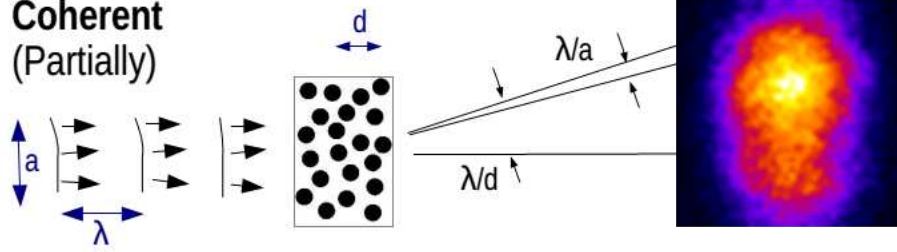


Figure 3.4: The details of the speckle are related to the coherent volume of the beam, a , the average separation, d , of the scatterers and, λ , the wavelength of the light used.

Here $\rho(-\mathbf{Q}, t)$ is the Fourier component of the electron density at time t and $\langle \dots \rangle$ indicates the statistical average of the system. This is the same function as measured for inelastic scattering experiments, *i.e.* the incident photon has a different energy, $\hbar\omega$, than the scattered photon. The frequency Fourier transform is:

$$g_1(-\mathbf{Q}, t) = \frac{1}{N} \langle \rho(\mathbf{Q}, 0) \rho(-\mathbf{Q}, t) \rangle, \quad (3.12)$$

and is also known as the intermediate scattering function, where N is the total number of scatterers in the system. However, in XPCS measurements it is the intensity that is measured and this is related to the electron distribution by the constant C which is dependent on parameters such as incident flux:

$$I(\mathbf{Q}, \omega) = C \langle \rho(\mathbf{Q}, t) \rho(-\mathbf{Q}, t) \rangle. \quad (3.13)$$

If the intensity measured is completely dynamic then the experiment is said to be homodyne, however if there is a portion of the scattered beam which is static and acts as a reference beam, then the experiment is heterodyne and there are differences in the expected results [73]. In a homodyne experiment the measured intensity time-time autocorrelation function, $g_2(\mathbf{Q}, \tau)$, is:

$$g_2(\mathbf{Q}, \tau) = \frac{\langle I(t') I(t' + \tau) \rangle_{t'}}{\langle I(t')^2 \rangle_{t'}} = 1 + A |g_1(\mathbf{Q}, \tau)|^2, \quad (3.14)$$

where the average is over the time t' . The second part of the equation shows how the intensity correlation, which is fourth order in the electric field, is related to the normalised intermediate scattering function, $g_1(\mathbf{Q}, \tau)$. When there is a static reference beam mixed with the fluctuating magnetic signal the mixing results in extra terms,

such that [74]:

$$g_2(\mathbf{Q}, \tau) = I_r^2 + \langle I_s(t) \rangle_t^2 [1 + \beta |g_1(t)|^2] + 2I_r \langle I_s \rangle_t + 2I_r \langle I_s \rangle_t \beta \text{Re}[g_1(t)], \quad (3.15)$$

where I_r is the static reference signal and I_s is the fluctuating sample signal. The mixing causes an oscillatory part to the signal which will manifest itself as a cosine component when fitting the data later in chapter 6. For those experiments, the reference beam comes from the charge scattering of the array, as the experiments were carried out on a structural Bragg peak. Therefore, our experiments are better described by a heterodyne picture.

3.4.1 Ergodic vs. non-ergodic

An ergodic medium is one which can explore the whole of phase space available to it, and therefore the time averaged speckle pattern gives a good representative picture of the ensemble dynamics. If this is not the case and certain portions of the sample are static, or ‘stuck’, then the sample will be non-ergodic. For instance, a scatterer may be able to make Brownian motion but only around a fixed point. Pusey and van Megen were able to calculate how the measured g_2 function would change for ergodic vs. non-ergodic media which is outlined in figure 3.5 [75]. The most important aspects of their results are that a time average for a static sample evaluates to 1 rather than 2 (for perfect coherence). This is the result of a typical volume containing uncorrelated regions which will give different average intensities at different scattering vectors. When you sample over the full ensemble the amplitude of the light field at time t , $E(Q, t)$, is a zero-mean complex Gaussian variable. In an ergodic medium the time average and ensemble average should be the same as the intensity within the speckle should fluctuate in time but also when measured for long enough it should move through a representative number of all the possible states and undergo the full range of Gaussian fluctuations. For a non-ergodic samples this is not possible and the time-average can have different starting values. The proportion of 2 that can be reached is also affected by the degree of beam coherence. As synchrotron X-rays are not good coherent sources, typical starting values are between 1 and 1.1, also defined as the coherence factor, which will be discussed in more detail in section 6.3.1.

3.4 X-ray photon correlation spectroscopy (XPCS)

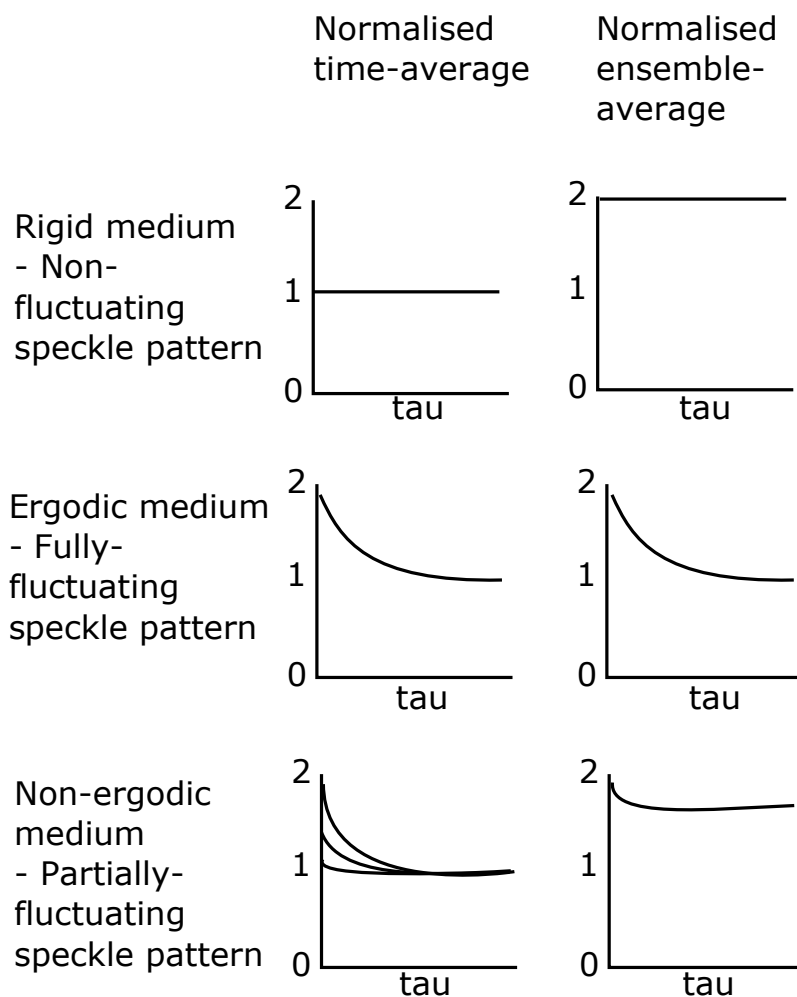


Figure 3.5: A comparison of time and ensemble averaging of the measured intensity correlation function (ICF), or g_2 , for an ergodic vs. non-ergodic sample. For a non-fluctuating sample, one would measure 1 for time averaged (a) or 2 for ensemble averaged (b). For an ergodic medium the time and ensemble averages equate to the same value (c,d). For a partly fluctuating or non-ergodic sample, the time-averaged starting values can be different (e) and ensemble-averaged ICF shows a plateau (f). Adapted from ref [75].

3.5 Summary

This section has introduced some fundamental concepts related to X-rays and how they can be used to measure periodic patterns on the nanoscale, and also magnetic moments via the XMCD effect. The XPCS technique has been introduced in preparation for the experimental chapter 6 and the fluctuating magnetic configuration of the spin ice is what leads to observed changes in the intensity of the speckle pattern on atomic resonance.

In this thesis, the two main soft X-ray experiments make use of the XMCD effect. TXM measures changes in absorption directly whereas XPCS is predominantly a scattering technique. For both experiments constant polarisation was used and the changes of absorption (TXM) or changes in intensity in the speckle (XPCS) were attributed to changing magnetic moments of individual islands.

CHAPTER 4

Methods

4.1 Introduction

In this chapter we will review the sample fabrication and characterisation techniques, including details and differences of the main synchrotron methods reported in this thesis. The majority of the nanofabrication was performed at the Center for Functional Nanomaterials at Brookhaven National Laboratory in collaboration with Dr. Aaron Stein, specifically samples made on silicon wafers used in the X-ray scattering experiments. In more recent times fabrication has moved over to the clean room facilities in Leeds, after a similar electron beam lithography tool became available in the School of Electronic and Electrical Engineering. The majority of the on-membrane samples made for the TXM measurements were made there in collaboration with Dr. Mark Rosamond. The characterisation tools discussed in this chapter will generally relate to determining sizes and volumes of the constituent nano-islands using scanning electron microscopy, atomic force microscopy and hard X-ray reflectivity (to determine film thicknesses). Also, details of the SQUID-VSM, which has been used to measure the magnetic properties of these nanomagnetic systems over a large temperature range, will be outlined.

4.2 Nanofabrication

For the main synchrotron experiments, samples were patterned on two different types of substrate. For the TXM experiments, it was necessary to pattern the sample on a substrate which was transparent to soft X-rays, therefore 100 nm thick Si_3N_4 membranes were used. In addition, as the the TXM beamline does not have sample heating capabilities, additional stages of lithography were involved in order to pattern an on-membrane heater and thermometer. For the X-ray scattering (and SQUID) experiments, samples were patterned on standard silicon wafers and did not require any additional stages of lithography as there was temperature control incorporated into the instruments.

4.2.1 Electron beam Lithography

In order to fabricate samples on the nanoscale, physicists must turn to chemists. There is detailed chemistry involved in creating the template of your pattern on the nanoscale which owes its precision to the size of the molecules of various resists. There are different ways to expose resists but the main one used in this thesis is done with an electron

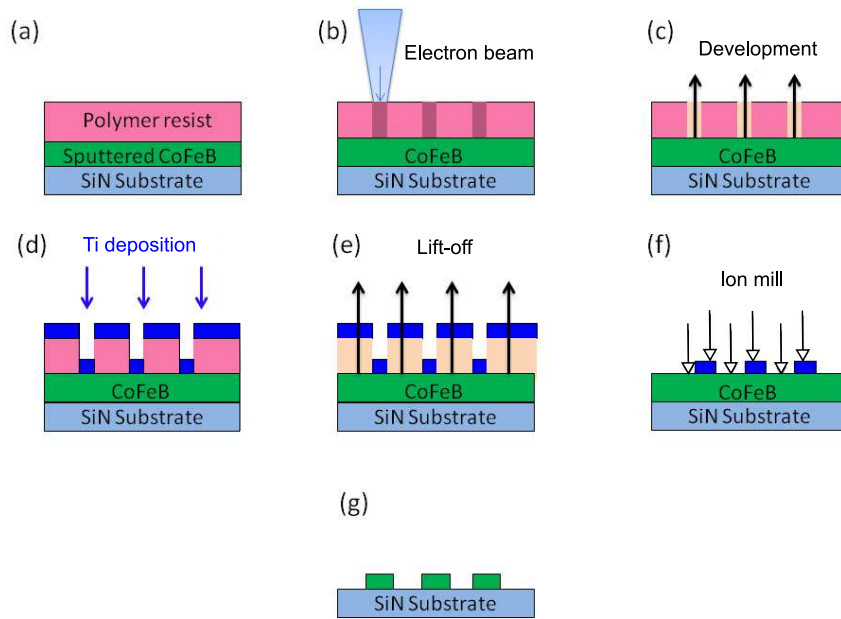


Figure 4.1: A schematic of the process developed in order to make CoFeB ASI on SiN membranes. In (a) the CoFeB has been sputtered on the the SiN substrate and then a polymer resist has been spun into a thin film and baked at 180 °C. In (b) the resist is exposed to a high voltage electron beam which writes the ASI pattern. The exposed parts of the film are removed in development, (c). Then Ti is e-beam evaporated in (d), adhering directly to the substrate where there is no longer resist. In (e) the remaining resist lifts off, also removing any metal on top of it, leaving the Ti hard mask of the pattern. In (f) the sample is ion milled and the Ti acts as a mask only to the CoFeB underneath the pattern. The unmasked CoFeB mills away with the Ti, leaving just the CoFeB in the desired ASI pattern.

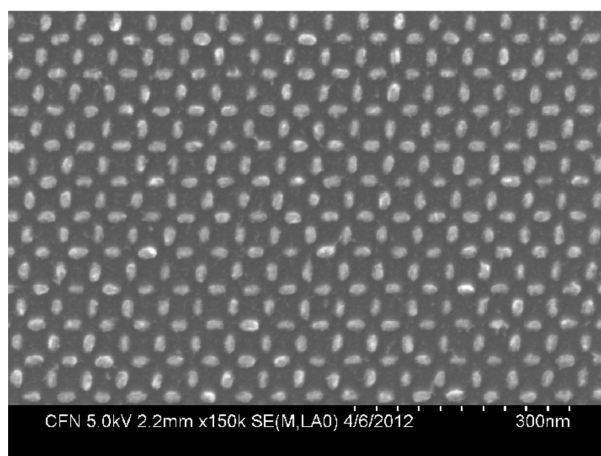


Figure 4.2: An SEM of the smallest ASI made with areal dimensions $8 \text{ nm} \times 25 \text{ nm}$ and 10 nm thick Py.

beam. The electron emitters used in electron guns in order to ‘draw’ the patterns on this ‘molecular paper’ are generally thermionic sources, however for higher stability and brightness it is more common nowadays to encounter field emission sources. The JEOL-6300 (as well as the Scanning Electron Microscope described later) have Schottky field emitters to produce the electrons. These tungsten filaments are heated and have a sharp tip where an electric field is excited by an extractor voltage, which acts to lower the thermionic emission energy barrier. The tip has a zirconia, ZrO_2 , coating to lower the work function of the tungsten and enhance the emission.

Firstly, a polymer resist, in this case, ZEP520A, is spun on to a clean substrate. It is placed on a hot plate at 180°C for 180 s to harden the resist and also remove excess solvent to reduce the possibility of bubbling during exposure. Then the predefined pattern is written with a 100 kV electron beam at a dose of $254 \mu\text{C cm}^2$ for the Si wafer (and an increased dose of $343 \mu\text{C cm}^2$ for the membrane), schematically shown in figure 4.1(b). As ZEP is a positive resist, the area which has been exposed undergoes scission which can then be dissolved away in amyl acetate; known as the development. The ZEP resist has been chemically enhanced so that it displays a very high contrast ratio which means that the dose to clear the resist has a very sharp feature and the probability of having under-dosed and leave resist residue is heavily reduced. This means the minimum feature size obtained is less than 10 nm ; as shown in figure 4.2. This effectively leaves a stencil of the desired pattern into which material is deposited.

4.2.2 Thin Film Deposition

Electron beam evaporation

E-beam evaporation is a physical vapour deposition process carried out in a vacuum chamber where a crucible of the source material is targeted by an electron beam and heated. Electrons produced via thermionic emission of a heated filament are accelerated, by an 8 kV potential, into a beam. This beam is then in turn directed by a magnetic field towards the source. There is no direct line of sight between the filament-evaporant or filament-substrate to prevent contamination of the electron gun assembly with the source material. The source, held in a water-cooled crucible, is heated by the high power electron beam (typically ≈ 1 A current) and only melts (or sublimes) at the surface to prevent alloying with the crucible. The material emitted has a cosine distribution with respect to the normal causing a unidirectional flux at the distance where the substrate is held. This prevents side-wall coating of the resist, ideal for the lift-off process used here. An oscillating quartz detector is used to monitor the rate of growth, which was typically $1\text{-}2 \text{ \AA s}^{-1}$. Within the evaporation chamber there are several source positions so that different metals can be deposited without breaking vacuum for clean growth. Permalloy is a good alloy for this evaporation process due to the similar physical properties of the two metals, Ni and Fe, which evaporate independently but at comparable rates and maintain the stoichiometry of the target. Unlike Py, the CoFeB used for TXM experiments was not suited to this method and had to be deposited via magnetron sputtering.

Direct Current (DC) Magnetron Sputtering Deposition

Sputtering is a method whereby thin films of high purity material can be deposited. It is an energetic method in comparison to evaporation deposition but allows materials with high melting points to be deposited fairly quickly and evenly. The deposition chamber used at Leeds attains a low base pressure, $\sim 1 \times 10^{-7}$ Torr, via a system of pumping techniques which include a primary mechanical roughing pump to reach the mTorr regime, then once the chamber dynamics are reduced from a viscous fluid flow regime to that of a Knudsen one, a cryopump is used. This consists of a cold, high-surface area, carbon porous stage (maintained at 10 K by a closed loop ^4He refrigerator system), which condenses gas molecules onto it. The majority of atmospheric gases are

adsorbed at this point, however molecular hydrogen and water vapour are usually left. A further method is employed to reduce the partial pressure of H_2O ; a liquid-nitrogen cooled Meissner trap which is attached to the chamber prior to deposition can achieve up to 1×10^{-8} Torr base pressure. This is mostly effective due to its large surface area within the chamber itself, *i.e.* pumping power not lost through poor conductance of pipes, flanges, etc. A working gas of argon is then flowed into the system during growth so that the actual pressure during deposition is in the mTorr regime. Argon is used as a working gas as the atoms have large enough mass to transfer sufficient momentum but small enough to only impinge surface atoms and its inert nature is paramount for clean growth. The target is held at a high negative voltage whilst the substrate is grounded, this causes electrons to be accelerated away from the cathode target. The argon gas is ionised by collisions with these electrons to create a plasma. The positively-charged plasma ions (Ar^+) are then accelerated back towards the negatively biased target, made up of the required growth material. The incoming momentum of the ions displaces the surface atoms of the target causing them to be ejected onto the substrate, thus creating a thin film of the target substance onto the substrate. However, to improve this simple DC method magnets are utilised; hence the nominal “magnetron”. A central pole is placed under the middle of the circular target and an opposite pole ring is placed around the edge. This static field is perpendicular to the electric field and causes the plasma to be trapped in a racetrack path due to the Lorentz force. The charged particles are maintained close to the surface so less gas is used but a greater number of ions are produced. This generally increases the sputtering growth rate to of the order of \AA s^{-1} .

4.2.3 Ion Milling

Ion milling is physical method of etching and works on a similar principle to sputtering. It can be used to gently remove oxides or impurities from surfaces before deposition as a preparatory cleaning procedure or, in our case, it can be used to physically etch through material. The preferred method to deposit into a resist stencil is evaporation as it is more unidirectional process and doesn't lead to the problems encountered when sputtering into patterned resist. As sputtering is a more energetic and Ar ions can arrive at the target from any angle this means the dislodged atoms also arrive at the substrate from all angles and this generally leads to side-wall deposition in the resist stencil, which after lift-off leaves unwanted material still attached at the edge; known

as flagging. In order to circumvent this problem one can try a bilayer resist process in order to discourage the side-wall deposited material remaining attached (a process discussed in the following section) or one can deposit the material before patterning and use another material, which is easily evaporated, as a hard mask material. This process is illustrated in figure 4.1. The ion milling was done in home-built system at Leeds which achieves a base pressure $\approx 1 \times 10^{-7}$ Torr via a turbo-molecular pump and benefits from having a load lock so that the main chamber stays at low pressure most of the time. An argon-oxygen working gas mix was used with a flow rate of 5 sccm giving a working pressure $\approx 1 \times 10^{-5}$ Torr. The operating parameters which gave a mill rate 1 \AA s^{-1} and a low roughness were 20 mA beam current and 80 V accelerating voltage.

4.2.4 Microheater and thermometer fabrication

For the TXM experiments where elevated temperatures are required, an on-membrane heater and thermometer were designed in collaboration with Dr. Mark Rosamond in the School of Electronic and Electronic Engineering at the University of Leeds. It operates via Joule (or resistive) heating, generally described by the Joule-Lenz law:

$$Q = I^2 R t, \quad (4.1)$$

where Q is the energy transfer, I is the current, R is the resistance and t is the time. Therefore, it is necessary to make the resistance highest at the point where you want most heat dissipation; as it is directly proportional to the resistance. This was achieved by decreasing the cross-sectional area *i.e.* making the wire much thinner around the sample array as $R = \frac{\rho l}{A}$, where ρ is the resistivity, l is the length of the wire and A is the cross-sectional area. The calibration of the heater using the thermometer will be described in more detail in section 7.3. The design is shown in figure 4.3 and incorporated a counter-wound meandering wire structure in order to prevent any induced magnetic fields from a circulating current. The heater wire was $15 \mu\text{m}$ wide and had a total of ten loops. The thermometry was defined as a double loop and was $6 \mu\text{m}$ wide, this minimised the space for the thermometry so it was close to both the samples and the heater and would not cause unwanted heating as the sense current would be very small in comparison. The material used for both purposes was Pt due to its highly linear resistivity with temperature and also high melting point, $T_m = 2041.5 \text{ K}$, making it ideal for high temperature purposes.

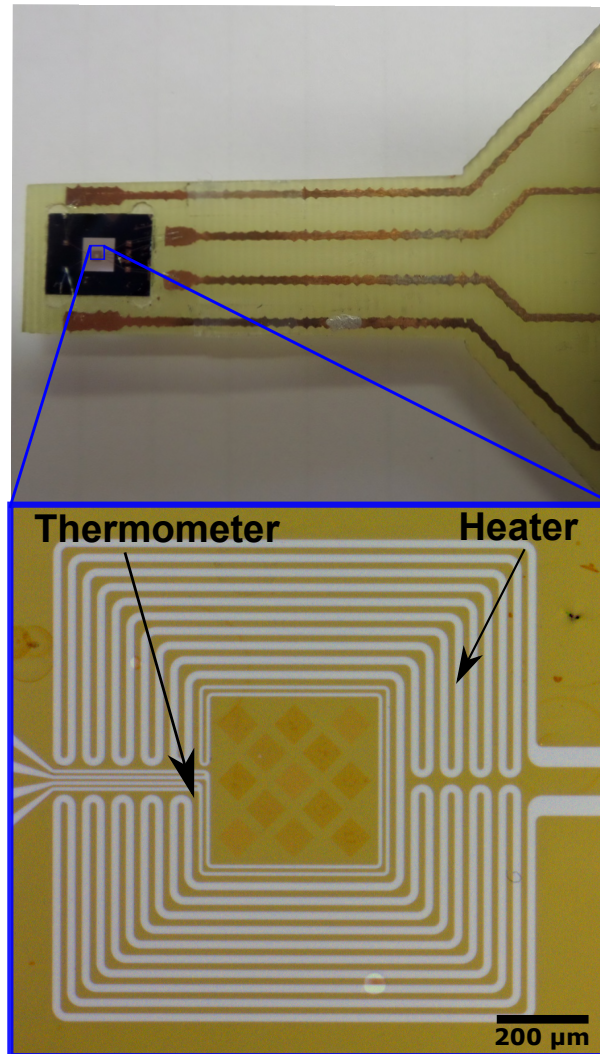


Figure 4.3: (Top) A photograph of the printed circuit board (PCB) used with the membrane attached showing the wire-bonded connections and also the recessed and drilled part of the board to allow the X-rays to be transmitted when mounted in XM-1 microscope. (Bottom) An optical image of the on-membrane heater and thermometer. The meandering Pt wire is counter-wound to avoid induced magnetic field at the sample and the ASI arrays were patterned in the centre of the design, here you can see 13 separate arrays.

The fabrication was carried out post-ASI patterning. A bilayer resist was used for this procedure. The bottom layer of MMA(8.5)MAA EL11 was spun at 4 krpm for 40 s and baked at 180 °C for 5 minutes, then PMMA 950k A4 was applied in the same way as the top layer. This higher molecular weight polymer provides an undercut in the patterning process to aid the lift-off procedure. The respective resist layers were 450 nm and 200 nm in thickness. As the design was on the microscale rather than the nanoscale the lower resolution mode of the JEOL6300 was used at a relatively high write current of 20 nA and dose of 824 $\mu\text{C cm}^2$. Development was IPA:H₂O (7:3) and the Pt was deposited via e-beam evaporation with a thin 5 nm Ti buffer layer to promote adhesion. The membranes were fixed to a PCB which had a small hole drilled out of it in order to be transparent to the X-rays during the experiment which can be seen in the upper panel of 4.3. They were micro-bonded for separate connections to the heater and thermometer wires.

4.3 Characterisation

4.3.1 Scanning Electron Microscopy

In order to characterise the shape and size of the islands which have been produced it is possible to use scanning electron microscopy (SEM). This technique uses a beam of electrons which are accelerated from a cathode to an anode at the sample, by a voltage ≈ 10 kV for conducting samples. A set of magnetic lenses focus the beam and scanning coils are used to move the beam laterally, to scan the sample in a rastering fashion. The electrons will scatter and reflect with different energies depending on their initial energy, how deeply they penetrate the sample, and the scattering cross-sections of materials. Scattering cross-sections are influenced by density and atomic number. The backscattered (high energy elastic scattering) and secondary electrons (with energy less than 50 eV) are collected and originate from the surface and upper few nm of the sample, respectively. These combine to build an image of the surface structure and contrast of the atomic number of the material. This helps to characterise the final outcome of the fabrication and can also be used as a diagnostic tool in a lower accelerating voltage mode to view the exposed resist in earlier stages of the process. An example of imaging by tilting the sample stage within the SEM is shown in figure 4.4 which is useful to detect flagging, the lift-off problem mentioned previously.

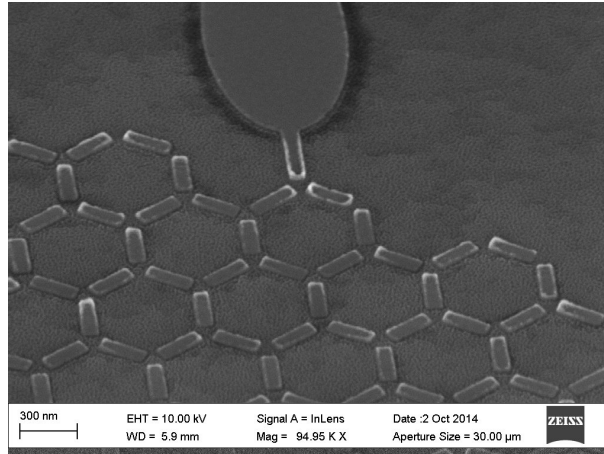


Figure 4.4: An example of a scanning electron micrograph taken at an angle of 45° in order to see if there was significant side wall deposition. This example is a kagome structure with an injection pad imaged on a membrane (more detail of the use of this injector is given in section 7.5). Side-wall deposition here is not drastic but can be seen most easily as bright edges on the islands near the injection pad.

4.3.2 Atomic Force Microscopy

An atomic force microscope (AFM) is one of a group of scanning probe techniques which were borne out of the original invention of the scanning tunnelling microscope (STM) in 1981 by Gerd Binnig and Heinrich Rohrer [76]. Binnig realised that if the STM tip was close enough to the surface other significant forces acted and he soon made use of this fact by developing the first AFM. The significant interaction between the tip and the surface was due to van der Waals forces which are attractive and slowly increase towards the surface. However, on further approaching the surface a repulsive force is encountered due to Coulomb repulsion.

The AFM builds a topographical map by raster-scanning a sharp tip, approximately 10 nm in diameter, across a surface which is attached to the free end of a microfabricated cantilever. Generally, the AFM used in this thesis was a Veeco Nanoman system in tapping mode. In this mode the cantilever is driven to oscillate at a frequency close to its resonance and any departures from this caused by tip-sample interactions are amplified. A laser beam is directed at the cantilever and the vertical deflection of the cantilever is recorded as a change in signal over a split photodiode. A piezo actuator makes sub-nm adjustments to the z separation in order to maintain a fixed amplitude.

The resolution is limited by the size of the tip so can be variable depending on the quality of the tip.

Magnetic Force Microscopy (MFM)

It was later realised if the tip was magnetic, the magnetic long range interaction could be probed using the same method, and this has come to be known as magnetic force microscopy (MFM). It relies on a topographic image to be first built up, then at a fixed height above the recorded topography, another line scan is repeated at an elevated distance above the surface (typically 30-100 nm depending on the strength of the interaction) and the deflection due to the magnetic signal is detected. MFM requires a tip which is coated with a magnetic material, those used in this thesis were generally Cr/Co tips, and they are magnetised by a permanent magnet before use so that they act like a magnetic dipole-type object. The magnetic mapping of the sample is created as the opposing forces from opposite sign components normal to the surface magnetisation create bright and dark contrast. Therefore, domains can be mapped qualitatively, however, quantitative information is difficult to extract and there can be huge variation in signal from tip to tip [77]. In the in-plane nanomagnets measured in this thesis have opposite out-of-plane components of stray field from each end which give contrasting force gradients and so opposite contrast.

4.3.3 SQUID-Vibrating Sample Magnetometry (VSM)

The SQUID-VSM system used for measurements in this thesis was a Quantum Design model capable of measuring the characteristically small moment from the patterned samples; in this case due to the low pattern coverage ($\leq 20\%$) and generally thin material (≤ 10 nm) used there is a trade-off between having a large enough sample area in order to measure a good signal, with the length of time it takes to pattern large area arrays. Samples therefore were patterned over 1 - 2 mm² areas. The operation of the standard VSM is based on Faraday's law where a magnetic sample is vibrated between a set of pick-up coils and produces an electromotive force which is detected as a voltage. First pioneered by Simon Foner [79], the set-up is arranged so that the direction of vibration and field are parallel. The sample is attached to the lower part of the sample rod and made to oscillate at a known frequency. Irrespective of the sample being magnetised permanently or in response to an applied magnetic field,

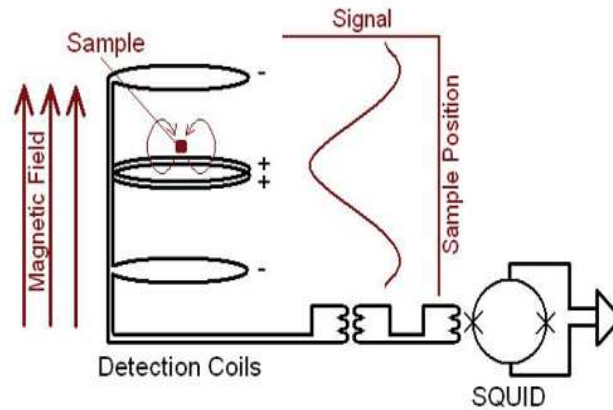


Figure 4.5: A simple schematic showing the detection method for the SQUID. The sample is vibrated in the detection coils and the resulting signal is inductively coupled to the SQUID device which acts as an extremely sensitive current-to-voltage converter (after ref. [78]).

the oscillation will induce an alternating current (AC) signal in a set of pick-up (or detection) coils. A lock-in technique is employed to extract the small changes in signal from the known vibration frequency and detects the in-phase voltage from the sense coils to identify the desired component of the signal. The noise signals at other frequencies are rejected and do not affect the measurement which ensures high sensitivity. This standard VSM method can reliably measure moments as small as $\approx 10^{-9} \text{ Am}^2$. In order to be sensitive signals up to a thousand times smaller than this $\approx 10^{-12} \text{ Am}^2$, a superconducting quantum interference device (SQUID) is used as a second order gradiometer to reject background flux. The SQUID is inductively coupled to the VSM detection circuit so that even for a tiny signal, the superconducting wire is able to sense it and convert it into a measurable voltage. It is an extremely effective low-noise current-to-voltage amplifier. A calibration file from a standard sample is used to convert the measured voltage into a value for the magnetic moment.

The sample temperature can be controlled over a range from 1.8 - 400 K by balancing the cooling power of the liquid He flow with a resistive heater. The liquid He is drawn from the main reservoir through a vent using a roughing pump and an optional oven module can be used to measure samples in the range 300 - 1000 K and in magnetic fields up to 7 T.

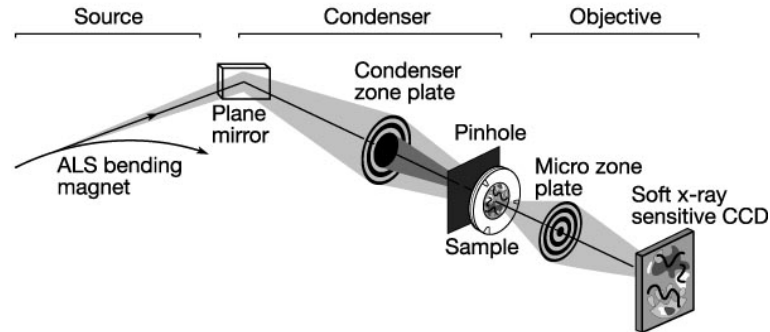


Figure 4.6: A schematic of the set-up for the XM-1 microscope taken from ref. [81]. The synchrotron bending magnet is the source of the X-rays, the plane mirror defines the energy of the X-rays, the condenser zone plate (CZP) focusses the beam. The central stop of the CZP and the pinhole create a partially coherent and monochromatic beam at the sample. The precisely engineered microzone plate refocusses and magnifies the image at the CCD detector.

4.3.4 X-Ray Reflectivity

X-ray reflectivity was carried out at Leeds in order to calibrate the thickness of thin films. The equipment used to do this was a Bruker Diffractometer in a low angle reflection geometry. At low angles, $2\theta < 10^\circ$ the scattered waves from the interface between electronically dense but different density layers produce an interference pattern characteristic of the layer thickness and can be fit with the Kiessig method [80].

4.4 Soft X-ray Methods

4.4.1 Transmission X-Ray Microscopy

The XM-1 microscope at the Advanced Light Source (ALS) in Berkeley is a transmission X-ray microscope (TXM) which can resolve features of less than 15 nm [81] and images can be recorded with an exposure time of a few seconds and it covers a several micrometer large field of view [82]. A schematic of the set-up is shown in figure 4.6. The synchrotron accelerates electrons to 1.9 GeV and injects them into a storage ring where they follow the trajectory of a 12-sided polygon. After each straight section, the electrons are deflected in a magnetic field, as they accelerate on a curved path they emit X-ray radiation tangentially. The microscope is placed at the straight of one of

these tangential paths. It uses the off-axis synchrotron radiation to illuminate samples with soft X-rays (500 - 1300 eV). As the refractive index of X-rays is close to unity, conventional refractive lenses cannot focus the beam, instead e-beam lithographically defined circular gratings, known as zone plates, must be used. A larger condenser zone plate (CZP) upstream of the sample focusses the beam on to the sample, and the micro-zone plate (MZP) refocusses the beam at the imaging plane to high magnification. A back-thinned, back-illuminated 2048×2048 pixel CCD camera acts as a detector to form the image, so the absorption is directly measured. The MZP is lithographically very challenging to fabricate as it has curved continuous lines defining each zone, the smallest of which defines the resolution of the technique:

$$k_1 \lambda / NA_{\text{MZP}}, \quad (4.2)$$

where k_1 is a sample-dependent constant for the illumination, λ is the wavelength of light and NA_{MZP} is the numerical aperture of the MZP. This is equal to $\lambda / (2\Delta r_{\text{MZP}})$, where Δr_{MZP} is the width of the outermost (smallest) zone. For our experiments, the smallest zone was 15 nm.

It is also possible to tune the energy of the X-rays to a certain value which corresponds to specific elemental absorption edges, *i.e.* the specific binding energies of electrons. For a given helicity the X-ray absorption cross-section will be strongly dependent on the magnetic orientation in the direction of propagation of the photons, a property known as X-ray magnetic circular dichroism (XMCD), previously discussed in 3.3.1. In the presence of spin-orbit coupling the angular momentum of the X-rays is transferred to the angular momentum of the photo-excited electron. Due to the larger magnetic moment of Fe and Co atoms they have the largest XMCD signal. For this reason $\text{Co}_{60}\text{Fe}_{20}\text{B}_{20}$ would be a preferable material over Py ($\text{Ni}_{80}\text{Fe}_{20}$) to study these systems as it has a larger percentage of Co than permalloy has of Fe, yielding stronger magnetic contrast in the analysis of the images. The effect can be measured with a constant polarisation of light and a varied applied magnetic field, as used here, or with constant (or no) applied field direction and varied helicity of the X-ray beam. The helicity of the X-ray beam is changed by moving either above or below the plane of the incoming X-rays (on-axis is linearly polarised). XM-1 previously demonstrated magnetic imaging in samples as thin as 3 nm [83] for out-of-plane magnetism. As the technique relies on charge-neutral photons, rather than the electrons of other methods (e.g. Lorentz-TEM, X-PEEM), a magnetic field does not affect the path of the beam,

and can be applied during imaging in order to collect real-time field-driven dynamics.

4.4.2 Soft X-ray Scattering

X-ray Resonant Magnetic Scattering (XRMS) is the process which measures the scattered photon after absorption of a photon has taken place (see section 3.3 for more theoretical detail). XRMS measurements are generally carried out in a diffractometer on a beamline which has linearly and/or circularly polarised light and access to the relevant atomic resonant energies responsible for the magnetism in a given system. It can be used to characterise magnetic domain periodicity, where at the resonant energies extra scattering terms coming from the magnetic order lead to additional Bragg peaks, not attributable to the charge scattering.

All scattering measurements were carried out at the Diamond Light Source in Oxfordshire (UK) and the specific details of the beamline and the modifications of the set-up that were made are described below with further detail to be found in chapter 6.

The I-10 Beamline and Optics

The BeamLine for Advanced Dichroism Experiments (BLADE), or I10, is a soft X-ray beamline designed to study magnetisation and magnetic structure. A schematic of its layout can be seen in figure 4.7. In contrast to the XM-1 bending magnet source, it uses synchrotron radiation produced by two helical APPLE-II undulators, capable of providing right and left circularly polarized and linearly polarized light. The energy range available is 0.4-2 keV which is most suited to the $3d$ and $4f$ magnetic elements, where the XMCD effect is strongest. There are two branches on BLADE, a scattering and an absorption branch, which both make use of the dichroic effects from the two different types of interaction. At the end of the absorption branch is a high field magnet and at the end of the scattering line is the Reflectivity and Advanced Scattering from Ordered Regimes (RASOR) diffractometer. The experimental work carried out in this thesis only utilised the scattering branch, inside RASOR.

As you can see in the schematic, firstly the helical undulator sources (with period 48 mm) provide the X-ray radiation, then the primary slits lower the power profile without much loss of flux. The toroidal focussing mirror (M1) focusses the beam in the horizontal direction and collimates it in the vertical direction. The plane grating mono-

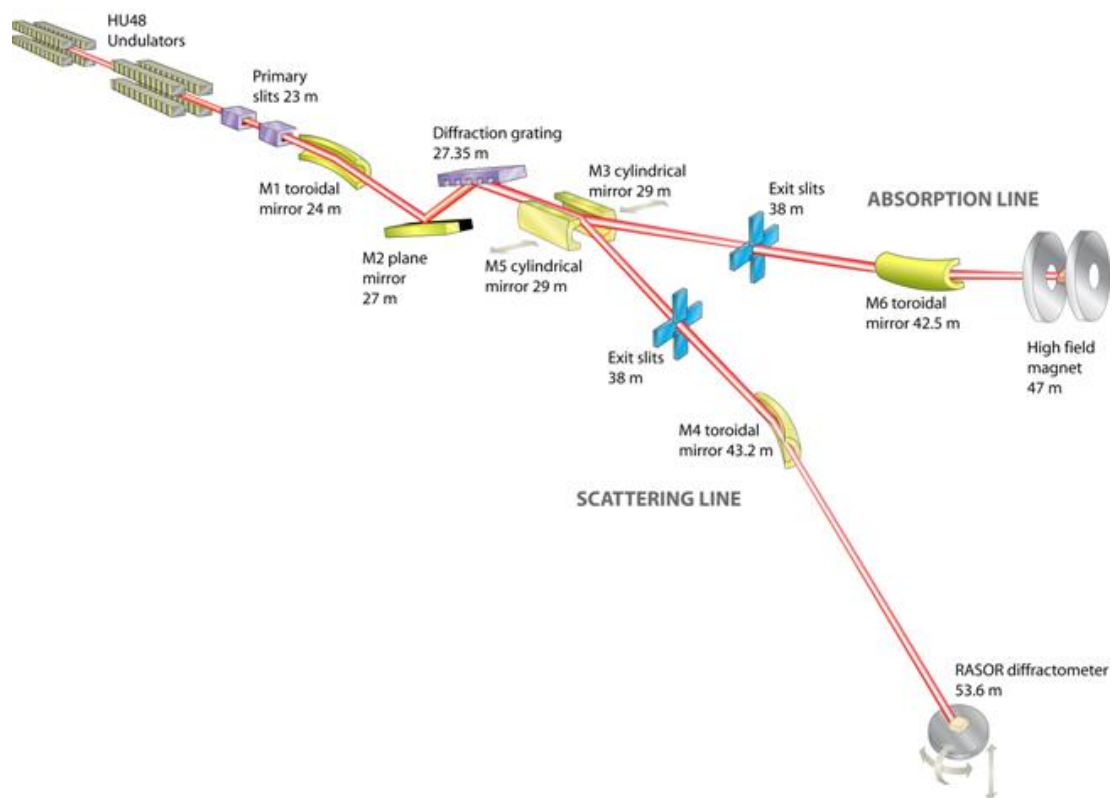


Figure 4.7: A schematic of the beamline optics at I10 at Diamond Light Source. The undulators provide the intense beam of X-rays, the focussing mirrors image and collimate the beam, the plane grating mirror and diffraction grating select the energy of the X-rays. The beamline has two branches which run independently, the scattering line is the one used in this thesis. The final optic refocusses the source from the exit slit at the sample position in the RASOR diffractometer (taken from <http://www.diamond.ac.uk/Home/Beamlines/I10/layout.html>).

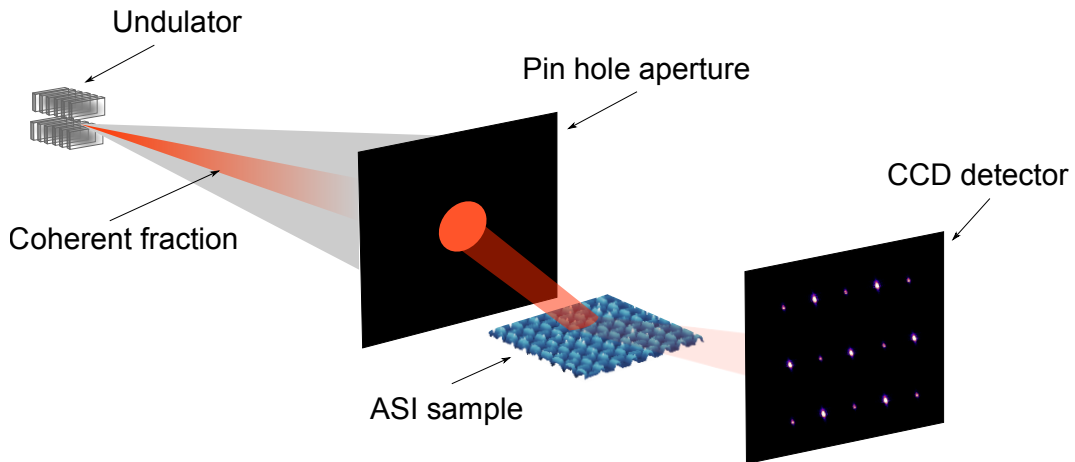


Figure 4.8: A schematic of the experimental set-up showing the incoming X-ray beam with its coherent proportion selected by the pin hole aperture. The reflection geometry is shown and the corresponding square diffraction pattern which is obtained on the CCD detector.

chromator (M2) can select the X-ray energy within the soft X-ray range without adjusting the magnification of the beam. After this there are cylindrical mirrors (M3/M5) which split the X-ray beam down the two possible branches at I10. The “exit slits” then act as a new source and the size of the X-ray beam upon leaving is $20 \times 200 \mu\text{m}^2$. The slits are 5.2 m from the refocussing mirror (M4), which re-images the exit slits at the sample position in the centre of the diffractometer.

The RASOR diffractometer

The RASOR diffractometer operates under high vacuum ($\sim \times 10^{-8}$ Torr) and sample movement has six axes of motion ($x, y, z, \theta, \chi, \phi$) in order to define precisely the diffraction conditions required for crystalline and nanostructured materials, as well as reflectivity measurements from surfaces. Its also fitted with a cryostat, allowing measurements in the temperature range $\sim 15 - 400$ K. The standard point detector usually used is a Si photodiode mounted on the 2θ circle which records the scattered intensity from a sample in “0D”. There are a set of different sized slits placed just before this detector, which can be individually selected and the resolution is defined by their aperture size. The reader is directed to the the publication of Beale et al. for a detailed description of the instrument and its design [84].

The XPCS technique and set-up

Previously, the measurements carried out at this beamline have utilised incoherent light, however, we have installed a pinhole before the sample to select the coherent portion of the X-ray beam as shown in the schematic of figure 4.8. The characterisation of the coherence of the beamline will be discussed in detail in section 6.3.1. By using coherent light we can probe the exact microstates of the individual nanomagnets. The incident photons will be scattered from the sample and interfere with each other, and their interference pattern is recorded at the detector. This interference pattern is known as speckle and depends on microscopic information such as the relative path lengths of the interfering waves and the separation between the scattering objects. If the detector is a CCD, the speckle diffraction pattern is recorded in 2D as shown in figure 4.8. The speckle pattern is directly representative of the scatterers and their disorder. If the position of a single particle is changed, all interferences are affected, and the details of the speckle pattern will change.

For the XPCS experiment, we have upgraded the detection aspect of RASOR by fitting a new “2D” detector which was installed on an external flange. The 2θ angle and distance from the sample were consequently fixed at 9.6° and 800 mm, respectively which is shown in figure 4.9. The resolution of the speckle pattern is determined by the pixel size of the camera, the wavelength of the X-rays and the distance between the sample and the CCD. We estimated the size of the speckle, S , as:

$$S = \frac{\lambda l}{d} = \frac{1.755\text{nm} \times 800\text{mm}}{10\mu\text{m}} = 140\mu\text{m}, \quad (4.3)$$

where l is the sample-CCD distance and d is the size of the pin hole. The CCD used in this experiment had a 2048×2048 pixel active area and each pixel was $13.5 \times 13.5 \mu\text{m}^2$. This results in one speckle covered roughly 10 pixels, giving good sampling statistics. During the measurements the back of the CCD was cooled, using a water chiller, to $T = -40^\circ\text{C}$ as this significantly reduced the dark noise. The sample was measured in reflection geometry which is illustrated in figure 4.9 and the angle of incidence was determined by the angle of the sample in relation to the beam, known as the θ rotation. Generally, a small incident angle was used ($\theta = 2 - 3^\circ$) in order to be sensitive to the in-plane periodicity of the sample [85]. A similar measurement geometry has previously been demonstrated on an artificial spin ice with incoherent light [16; 17].

As highlighted already in section 3.4, XPCS requires the measurement of the time

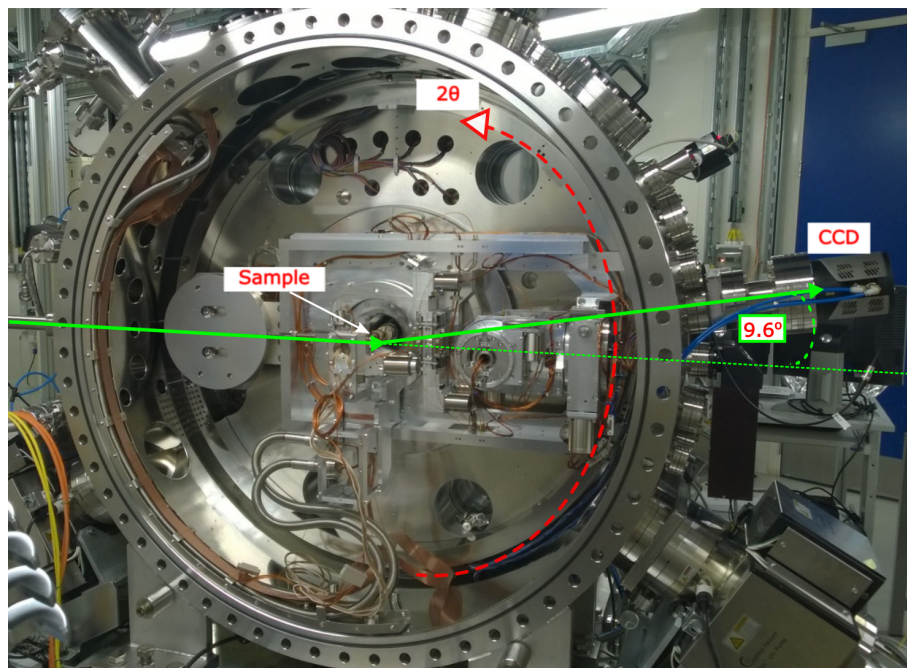


Figure 4.9: The RASOR diffractometer with the incoming X-ray beam marked with a green arrow, the point detector can move around the 2θ circle as outlined with the dashed red line and the CCD was mounted on an external flange at fixed angle $2\theta = 9.6^\circ$ from the incoming beam direction (photograph credited to Prof. Sean Langridge).

evolution of the speckle pattern. Dynamic Light Scattering (DLS) with photon correlation spectroscopy (PCS) has been widely used as a technique in polymer and soft matter physics for many decades to describe the dynamics of the speckle [86]. In that case laser light of optical wavelength probes dynamics usually on the micron scale, although the same optical theory applies. They use the normalised intensity-intensity auto-correlation function to characterise the timescale of the dynamics, g_2 , which is calculated according to:

$$g_2(Q, \tau) = \frac{\langle I(Q, t)I(Q, t + \tau) \rangle}{\langle I(Q, t) \rangle^2}. \quad (4.4)$$

A pictorial representation of how this calculation is done for our experiment is shown in figure 4.10. A long time series of a speckle pattern at one Bragg position is taken creating a stack of images over a whole measurement time t_m . For a singular pixel, its corresponding intensity can be plotted as a function of time, as shown in the figure. It is then possible to define different delay times, $\tau_{1,2}$ for example, in order to calculate the correlation function and these are indicated by the dotted lines. The function evaluates to a high value if the intensity looks the same, as would be the case for the shorter delay time τ_1 shown here, and to a low value if it has decorrelated as would be the case for the τ_2 . The normalisation (the denominator in the equation) comes from calculating the square of the average intensity of one pixel over the entire measurement time, indicated in the figure by black dotted line. Each stack of images were cropped to include only one Bragg position and so only one speckle pattern and the g_2 was calculated for each pixel within the cropped image. The average over all pixels (all Q) was taken and plotted for that delay time. Examples of the resulting $g_2(\tau_2)$ functions will be shown in section 6.3.3.

One thing to point out is that the $g_2(\tau_1)$ function would be averaged over many more pairs of points than that of $g_2(\tau_2)$, therefore it is general procedure to measure for much longer than the longest timescale one would want to probe in order to have good enough statistics for the longest delay times. The resulting correlation function is a measure of how correlated the intensities are at all possible delay times during the measurement. In our case we took images usually over a few hours. This obviously requires very high stability of the beamline over these sorts of time periods. The exposure time of the CCD ranged from 2 ms to 1 s, although most experiments had exposures in the lower end of this range; 10 - 100 ms. The actual time resolution was defined by the the 4 s delay between acquisitions; a combination of the readout time

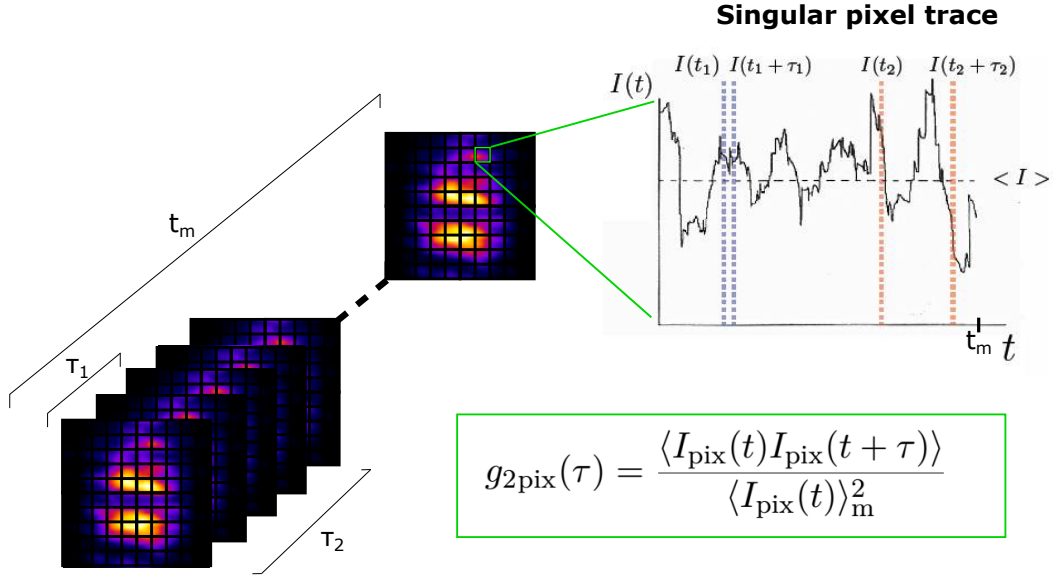


Figure 4.10: A schematic of the measurement process, showing the image stack acquired during one measurement time, t_m . The speckle pattern is divided into a grid of pixels and for each pixel there is an intensity trace as shown. The blue dotted line on the plot signifies a short delay time, τ , and the orange dotted line indicates a longer time delay. $\langle I \rangle$ indicates the average intensity value over the whole time of the experiment, t_m , the square of which is used as the normalisation. For each pixel the g_2 function is calculated for each value of τ and averaged over all pixels, giving an average over Q .

of the CCD and software-hardware communication.

4.5 Micromagnetic Simulation

Simulations using micromagnetic packages have been used to study the switching mechanisms involved in individual and pairs of nanomagnets. They are designed to calculate mean field problems numerically, as otherwise the task for any realistic sample size would be labour intensive. It employs a finite element method which involves dividing the sample volume into small cubes, usually a few nm in size, and solves partial differential equations using an iterative approach.

4.5.1 MuMax Package

The MuMax software used in this thesis is a micromagnetic package very similar to the well-known OOMF simulation package from NIST [87], with an important difference in that it is designed to run on graphics processing units (GPUs). The source code is freely available to download and use [88].

The method used is the minimisation of the Landau-Lifshitz-Gilbert (LLG) equation:

$$\frac{d\mathbf{M}}{dt} = -\gamma\mathbf{M} \times \mathbf{H}_{\text{eff}} \frac{\alpha\gamma}{M_S} \mathbf{M} \times (\mathbf{M} \times \mathbf{H}_{\text{eff}}), \quad (4.5)$$

where $\gamma = g\mu_B/\hbar$ is the gyromagnetic ratio, \mathbf{H}_{eff} is the combination of the internal demagnetising field and the external applied field and alpha is the damping parameter. For each small cell volume, eq. 4.5 is solved to minimise the magnetostatic energy. It allows the 3D visualisation of the spin configurations of the sample and its associated demagnetising field. The input parameters required for simple calculations include the saturation magnetisation, exchange constant and the damping parameter of the material been used. All simulations carried out were done with T=0 K and standard properties for Py were used.

CHAPTER 5

Magnetometry of Thermal Artificial Spin Ice

5.1 Introduction

There has been little data reported on the magnetometry of artificial spin ice as a function of temperature. This is perhaps due to the large patterned areas required to give enough signal to measure in even the highest resolution magnetometers. Arnalds *et al.* recently offered insight into accessing the dynamic regime of coupled nanomagnets. They were able to define the regime between a frozen and a fully paramagnetic state by measuring patterned circular nanodisks as a function of their size and interaction, using low temperature MOKE [89]. Here we have patterned samples over 1 - 2 mm² areas and used an ultra-sensitive SQUID-VSM magnetometer to measure their response to applied field as a function of temperature. AC susceptibility measurements have also probed the dynamic character of the samples as a function of temperature. These results have been used as a characterisation tool to inform the XPCS experiments of this thesis.

5.1.1 Experimental set-up

Samples were cut < 5 mm dimensions in order to mount on the quartz stick of the SQUID. This was usually done post-patterning with a wafer saw. Measurements were done in the normal operating mode of the SQUID in the temperature range 5 - 390 K or in the oven mode in the temperature range 400 - 700 K. For oven mode measurements, samples were fixed to the sample stick with zirconia concrete (soluble in water) and wrapped in a Cu foil. The oven sample sticks incorporate a heater and thermometer and the foil is to ensure good thermal contact between the sample and these components.

Standard hysteresis curves as a function of temperature have been measured as well as zero field cooling and field cooling (ZFC-FC) experiments. These were carried out by heating the sample above its blocking temperature, or as high as possible (395 K), in order to randomise the system then cooling in zero applied field. After this a small probe field is applied as the sample is warmed back up and the magnetic moment is recorded. The spins will align with the applied field once they reach their blocking temperature. The FC measurement is usually performed straight afterwards and simply measures the sample moment whilst cooling. The temperature at which the curves separate (bifurcate) or where the ZFC curve peaks, gives a measure of the average blocking temperature of the sample.

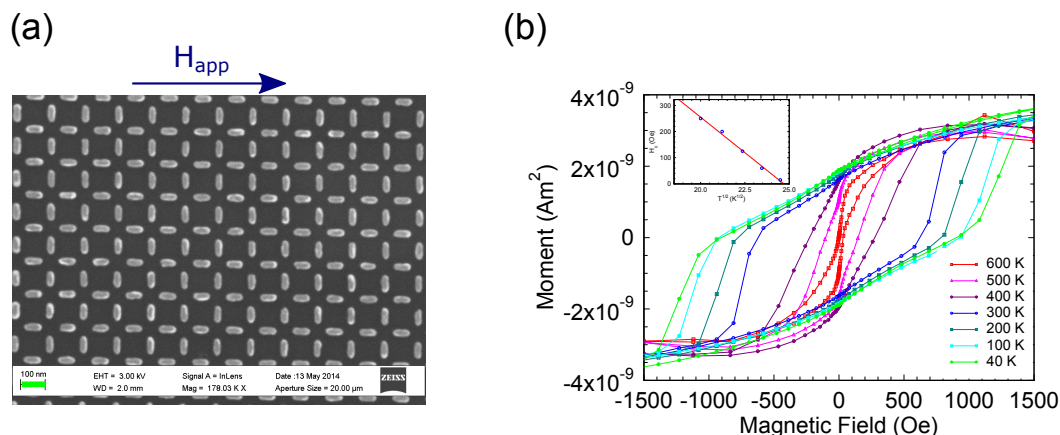


Figure 5.1: (a) Scanning electron micrograph of an ASI with islands 30×70 nm and a lattice spacing of 140 nm with the applied field H_{app} indicated along the [10] direction (green scale bar is 100 nm) (b) Hysteresis for this sample measured in SQUID over a large temperature range. At the highest temperature the coercivity is reduced to nearly zero, indicating the onset of superparamagnetic behaviour. (Inset) The $T^{1/2}$ dependence of H_c , fitted with eq. 5.1.

5.2 $m - H$ hysteresis loops with temperature

Hysteresis loops were measured on an ASI sample with islands 30×70 nm with 10 nm thickness and a lattice spacing of 140 nm as shown in figure 5.1. The loops taken at different temperatures in the range 40 - 600 K are shown in (b). The array was patterned over an area of 2 mm^2 , totalling some 408 million individual islands sampled during the measurement. Assuming the saturation magnetisation of Py to be 860 kAm^{-1} and using island dimensions measured from SEM, gives a total predicted sample moment of $7 \pm 1 \text{ nAm}^2$, the majority of the error here coming the measured thickness from AFM. The maximum measured moment at $T=5 \text{ K}$ is 3.3 nAm^2 , which is 47 % of that expected. This implies a much lower magnetisation of the sample, of 405 kAm^{-1} . A reduction of this magnitude after patterning has previously been seen for Py by Farhan et al. [8; 14]. A possible cause could be due to oxidation. The samples were capped with 3 nm of Al, however, it is possible that the Al may not have been thick enough to have the thin Al layer between the aluminium oxide that forms on the top with atmosphere and the Py metal underneath. Also, as the cap is not conformal it is likely that oxidation occurs at the edges also resulting in a reduced moment.

The measurement was carried out with the magnetic field applied along the [10] axis of the array *i.e.* the easy axis of one of the sub-lattices and the hard of the other

sub-lattice. The shape can therefore be understood as a combination of the prediction of the Stoner-Wohlfarth model for the two cases (from section 1.2.2). The superposition of the two curves has an overall positive slope coming from the hard axis contribution, with an abrupt change in the moment at the field where the easy axis reverses. This is signified by the sharpest dM/dH slope in the data. The shape at low temperature is very similar to what was reported by Kohli *et al.* for their 80×220 nm (25 nm thick) square ASI [67]. Their measurements were done at room temperature using a focussed MOKE magnetometer, also along the [10] axis. This indicates for our sample at these low temperatures, we are below its blocking temperature and it is in an athermal state. Interestingly, as the temperature is increased the shape changes from a square shape to a more ‘wasp-waisted’ shape at the highest temperature, due to the different field orientation with respect to the two sub-lattices. The largest changes can be noted in the coercivity, decreasing from around 1240 Oe at 40 K to nearly zero at 600 K. Also, there is a notable change in the remanent moment, again decreasing from around 60% m_S , to almost zero at the highest temperature measured. Both of these changes indicate thermal activation as we increase the temperature [90]. We would expect that when all the islands are in the the fully superparamagnetic, $H_c=0$.

The coercivity for these loops was measured as $H_c = H_{m=0}$ and can be used to estimate the blocking temperature of the sample according to [90],

$$H_c = H_0 \left[1 - \left(\frac{T}{T_B} \right)^{1/2} \right]. \quad (5.1)$$

The fit shown in the inset of figure 5.1 (b) gives the field, $H_0=1340 \pm 50$ Oe. This field is equivalent to the zero temperature energy barrier height to reverse the particle, $H_0 = 2KV/m_{\text{island}}$ [90]. The fitted value gives an $M_S \Delta N_D$ product of 1.07×10^3 A/m and if we assume the $\Delta N_D = 0.1$, then this measure of $M_S = 1.07$ MA/m, is much higher than the expected value. The fitted blocking temperature of the array is 610 ± 7 K. This is in good agreement with the data as the loop at 600 K is almost fully closed.

5.3 AC susceptibility

The AC susceptibility was measured for the same sample and is shown in figure 5.2. The measurement was carried out using a small AC field of 10 Oe and frequency of

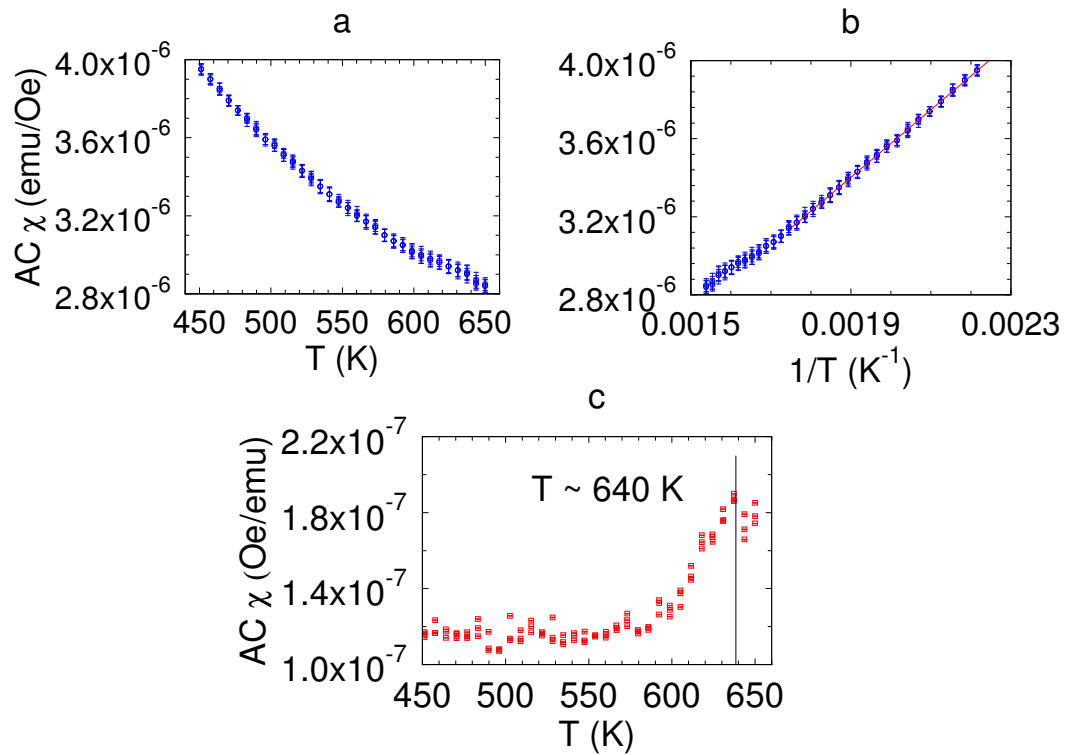


Figure 5.2: (a) AC susceptibility measured at 1000 Hz in the temperature range 400-650 K in the SQUID oven mode. (b) The same data plotted with inverse temperature and the red line is the fitted $1/T$ behaviour. (c) The susceptibility after the paramagnetic contribution has been subtracted. There is a peak feature around 640 K, interpreted as the blocking temperature.

5.4 Thickness and interaction dependence

1000 Hz. Plotting the signal as a function of inverse temperature, a linear behaviour is observed up to ≈ 550 K, this can be attributable to a paramagnetic contribution from the sample stick. Fitting this $1/T$ Curie-like behaviour, $\chi = C/T$, gives a constant of proportionality 0.0017 ± 0.0001 emu/OeK which has been confirmed from other measurements on different samples. After subtracting the background signal a peak was observed at $\approx 640 \pm 6$ K, at a temperature similar to that which was estimated from the coercivity data, although the fitted error does not account for the discrepancy in the values. The discrepancy could arise from the different sampling times of the measurement for the two techniques. The AC measurement has a sampling time, $t = 2$ s, whereas the averaging time at each field for the hysteresis loops was 5 s. This larger measurement time would lower the observed T_B , as can be seen from [60]:

$$\ln(t_m/\tau_0) = KV/k_B T_B \quad (5.2)$$

Therefore, for a longer measurement time $\ln(t_m/\tau_0)$ increases and T_B would be smaller for a shorter measurement time. This is because the nano-islands have more time to thermally relax over their energy barriers whilst the measurement is taking place, they are not able to do this when the measurement is done quickly and therefore appear less dynamic [91]. The ratio expected would give a difference of 8% from the T_B found from the hysteresis measurements; giving $T \approx 660 \pm 10$ K, which is in reasonable agreement with the observed deviation.

5.4 Thickness and interaction dependence

In figure 5.3(a), H_c has been plotted for nominally the same size islands, 30×70 nm but for four different thicknesses detailed in the legend. Plotted are data for $a=140$ nm (solid symbols) and for the two lowest thicknesses, the 8 and 5 nm-thick samples, are additional data for $a=240$ nm (open symbols). It can be seen that as the thickness is reduced so too is H_c . Also for decreased coupling there is a reduction in H_c , most obvious at $T=5$ K, between the 140 nm and 240 nm lattice spacings. The difference for the 5 nm sample between the two lattice spacings is $\Delta H_c \approx 300$ Oe. Another interesting feature of the 5 nm data is that on increasing the temperature, the H_c values for the two lattice spacings converge, and therefore the decrease is much more rapid for the more strongly coupled arrays. Whereas, the more weakly interacting samples have a very gradual decrease into a plateau. This is further evidence for superparamagnetic

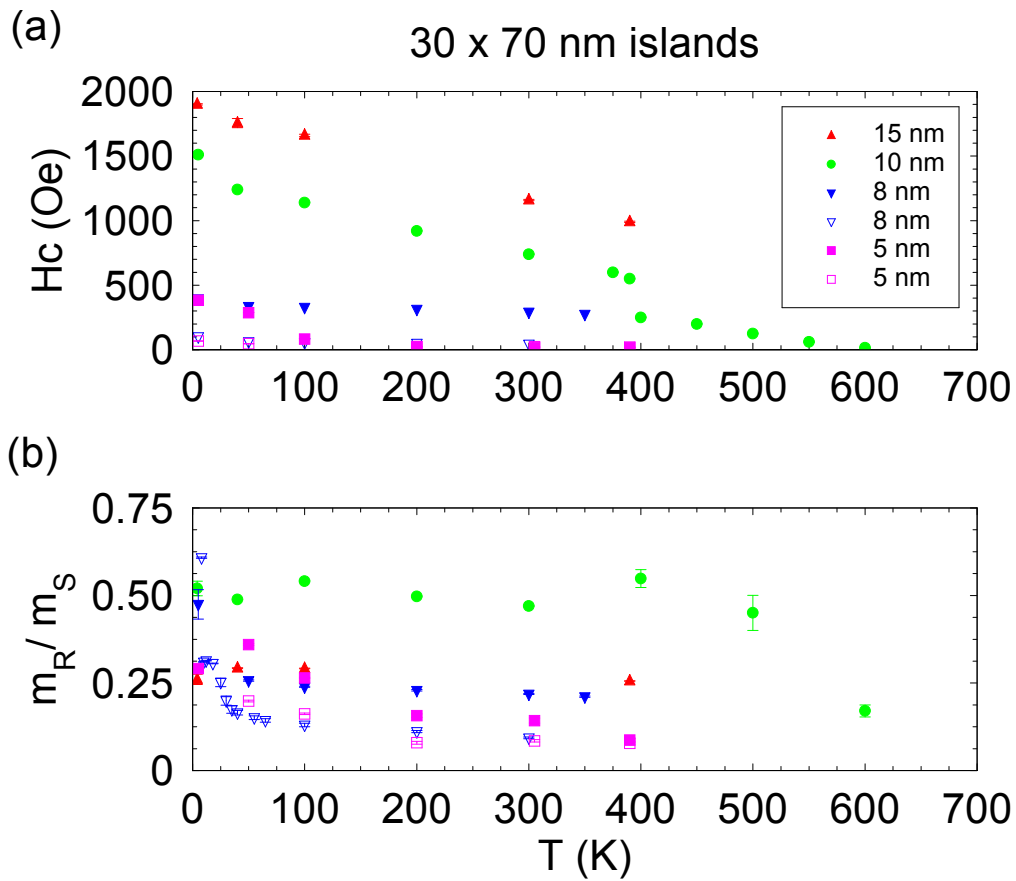


Figure 5.3: (a) Coercivity and (b) m_R/m_S as a function of temperature for nominally the same island size but different thickness or lattice spacing. Colours indicate different thickness of Py with 15 nm (red), 10 nm (green), 8 nm (blue) and 5 nm (pink). The solid points indicate the more strongly interacting 140 nm lattice spacing, whereas the open points indicate the weaker interaction of the 240 nm lattice.

5.5 Larger lateral islands with small thickness

behaviour, as it has been previously shown that ferromagnetism can be recovered from a fluctuating sample if the interaction between elements is increased [30; 92].

Also plotted in (b) the m_R/m_S values, which are expected to be 0.5 as the average of the easy and hard remanent values from Stoner-Wohlfarth model. Once the islands become fully dynamic you would expect this value to drop to zero [89]. Here it is easy to see for the 10 nm thick sample (green data points), m_R/m_S takes a value close to 0.5 until $\cong 450$ K, whereafter it reduces to 0.17 ± 0.03 at the highest temperature. The thickest sample has a constant value of 0.27 ± 0.02 , indicating no change over the temperature range measured. This suggests we do not reach any dynamic region, a fact supported by the high measured coercivity at all temperatures. For the 8 nm samples (blue data points) they start with high values at the lowest temperature and rapidly drop to 0.26 (140 nm) and 0.15 (240 nm) by $T=50$ K, with a gradual decrease thereafter. The 5 nm samples also behave in a similar way, reaching the smallest value of all samples measured, 0.08 at 390 K, indicating a fully SPM state.

5.5 Larger lateral islands with small thickness

In figure 5.4 (a) and (b) the half hysteresis curves are shown for much larger lateral islands - having areas of $80 \text{ nm} \times 250 \text{ nm}$ - but with thickness of 3.5 nm, for lattice spacings 350 nm and 450 nm, respectively. There is a monotonic decrease of H_c and m_S with temperature for both samples. Again the maximum measured moment is lower than what would be expected, giving a reduced magnetisation of $0.7 \pm 0.1 M_S(\text{Py})$, similar to that seen in section 5.2. Also, we can see that there are still blocked particles at the highest temperature measured (390 K) in the hysteresis, due to the non-zero H_c and m_R . Plotted below the hysteresis, in (c) and (d), are the ZFC-FC curves for the same samples. For these measurements, we can see that where the two curves bifurcate at a similar value in temperature to that in the ZFC curve. As they coincide reasonably well, this gives an indication of the average blocking temperature. This is very similar for the both lattice spacings, within the error, at 265 ± 5 K. The broad feature in the ZFC can be attributed to a large distribution in blocking temperatures which can come from the size distribution due to the inherent disorder of the patterning process but also from the presence of dipolar interactions, as both alter the energy barriers of the system [93].

We have plotted this data along with additional samples in the thickness range 3 -

5.5 Larger lateral islands with small thickness

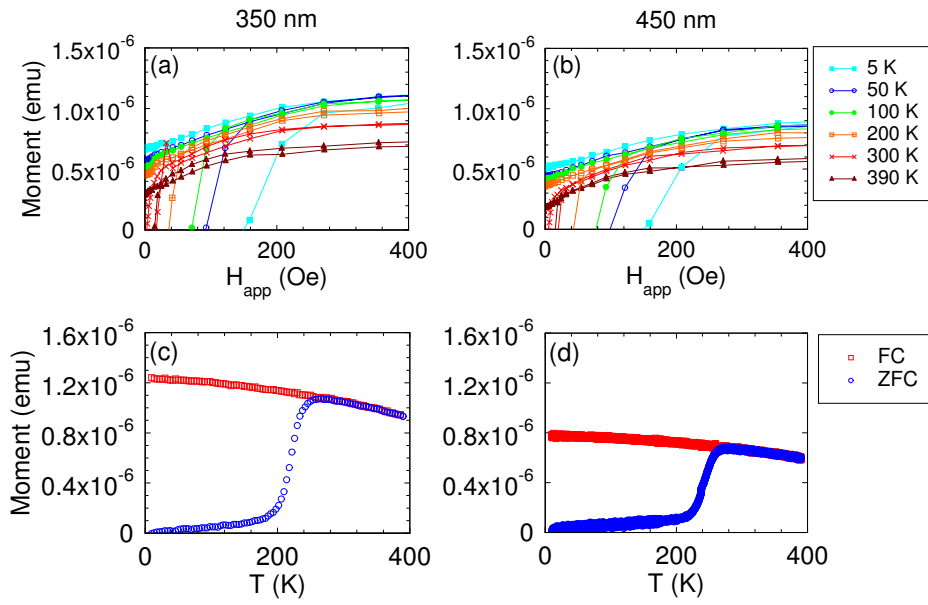


Figure 5.4: Hysteresis at different temperatures for $80 \text{ nm} \times 250 \text{ nm}$ islands, 3.5 nm-thick with lattice spacing (a) 350 nm and (b) 450 nm (lines are to guide the eye). Also shown are the corresponding ZFC-FC curves underneath in (c) and (d).

5.5 Larger lateral islands with small thickness

4 nm, for 350 nm and 450 nm lattice spacings in figure 5.5(a). They are in contrast with the 30 nm \times 70 nm samples, as there is no trend in the H_c at the lowest temperature with thickness, nearly all samples start from a $H_c \approx 150\text{-}250$ Oe (except for the thinnest sample) and also the rate of change with temperature is different. The same analysis has been carried out as before, fitting the H_c data with eq. 5.1 but this time we compare it to that observed in the ZFC-FC data. In (b) the fits are shown for the same sample as the previous figure, and in both cases they estimate the T_B to be higher than the T_B of the ZFC-FC data which was $\approx 265 \pm 5$ K, with $T_B(350\text{nm}) = 320 \pm 30$ K and $T_B(450\text{nm}) = 380 \pm 30$ K, interestingly for the less interacting sample it overestimates T_B more. A similar behaviour is observed in the 4 nm sample shown in (c) giving a $T_B(350\text{nm}) = 590 \pm 70$ K and $T_B(450\text{nm}) = 700 \pm 200$ K, although the error here is much larger. It would perhaps be expected that eq. 5.1 would do better to estimate the less interacting samples, due to the fact it is derived based on a non-interacting system, but it actually seems to fare worse. This large error suggests more sophisticated models are needed, which would take into account the combination of the size distribution and interaction effects [93].

For the other samples the T_B and H_0 values were extracted from the $H_c - T$ plots and are summarised in figure 5.6. A linear increase in T_B can be seen for increasing thickness, as to be expected for the increasing volume and subsequent increasing energy barrier. More interestingly, however, is that increased coupling seems to act to lower the T_B in the two thickest samples. As previously discussed, a truly SPM system is non-interacting and requires a modification of the energy barrier (section 1.2.4). Naively, one might expect that increased coupling should act to stabilise the FM state, as shown by the results of Cowburn *et al.* discussed in section 1.2.4 (ref. [30]). However, in some recent studies it has been shown that higher concentrations (stronger interaction) can actually lead to a negative correlation with the blocking temperature [94; 95]. The origin of this is still disputed and a model has been proposed by Mørup and Trunc [96] using a argument similar to that of Shtrikman and Wohlfarth (S-W) [97]. This is based on the definition of different regimes of weak and strong interaction. In order to define the regimes, they compare the interaction energy and the anisotropy energy. In the weak limit, where the anisotropy energy is high compared to the interaction energy, they argue there is a negative correlation between T_B and interaction strength. In a strongly interacting regime, they argue the blocking temperature is associated

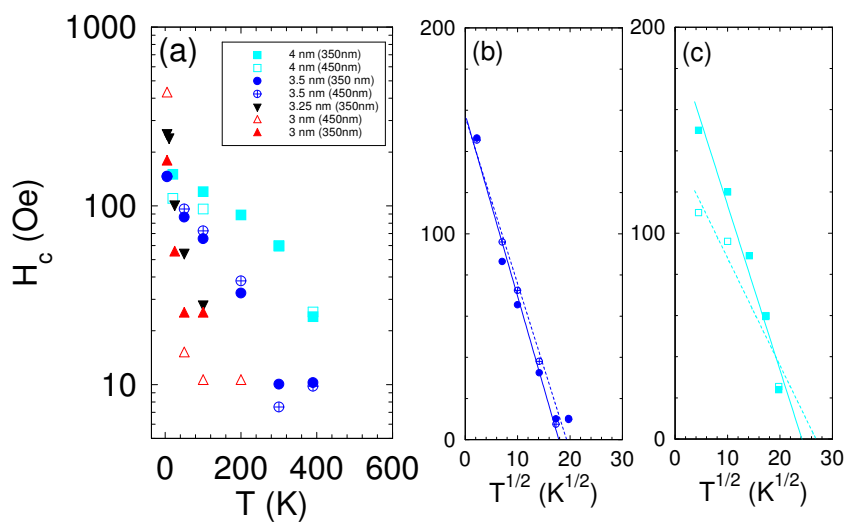


Figure 5.5: (a) Coercivity as a function of temperature for nominally the same island size but different thickness and lattice spacing (notice the log scale). The solid symbols indicate the more strongly interacting 350 nm lattice spacing, whereas the open symbols indicate the weaker interaction of the 450 nm lattice. The fitted blocking temperatures T_B as a function of thickness for (b) 3.5 nm and (c) 4 nm. There is also some hint that interaction strength has a negative effect on T_B , suggesting our samples are in the weak S-W regime.

with the freezing of a collective state into a glassy or superferromagnetic state at low temperature, resulting in a positive correlation of increased interaction and blocking temperature [92].

S-W first introduced this model in the context of spin glasses or, more generally, interacting magnetic clusters. They define the temperature:

$$T_K = KV/k_B \quad (5.3)$$

and compare this energy scale with the interaction energy as calculated from the eq. 1.9, which for parallel neighbours separated by their lattice constant, a , simplifies to:

$$E_{\text{dipolar}} = -\frac{\mu_0 m_{\text{island}}^2}{\pi a^3}. \quad (5.4)$$

If $E_{\text{dipolar}}/k_B \ll T_K$, the system is in the weak coupling regime and $E_{\text{dipolar}}/k_B \gg T_K$ defines the strong regime. We can attempt to categorize the samples measured in this chapter within this framework. Calculating E_{dipolar}/KV over the whole thickness range, using the measured magnetisation for each sample, we see that the smaller islands from section 5.4 have ratios between 0.016 - 0.146, whereas for the larger lateral but thinner islands from section 5.5 the ratios lie in a region 0.02 - 0.03. This would suggest that for all samples we are probably in the weaker regime and therefore should expect negative correlation of T_B with increased interaction.

5.6 Conclusions

The thermal activation in artificial spin ice has been probed using conventional magnetometry, namely with $m - H$ hysteresis curves, AC susceptibility measurements and ZFC-FC measurements. Lower than expected magnetisation has been measured for the patterned samples compared to the bulk value, having values between 0.5 - 0.7 $M_S(\text{Py})$, consistent with other groups' findings [8; 14]. For the smaller, more strongly interacting islands, there is a larger change in H_c as a function of temperature, which could be attributed to the onset of collective behaviour at low temperatures, described as superferromagnetism although more extensive modelling is called for. For larger 80 × 250 nm thin islands, a decrease in T_B was observed and can be explained as the reduction of the energy barrier due to decreased volume. There is also some evidence that T_B is shifted to higher temperatures for more weakly interacting samples, although the

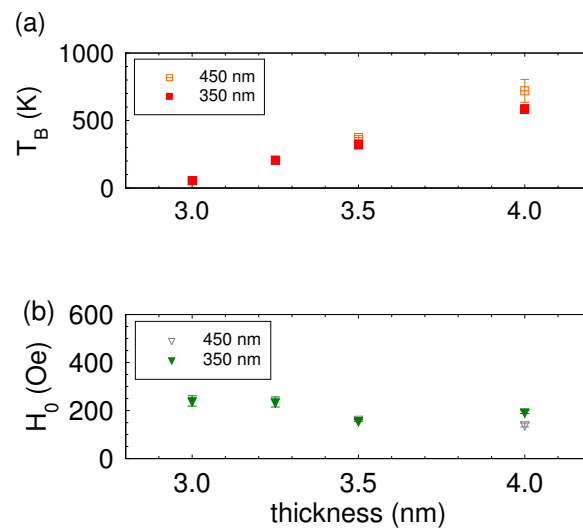


Figure 5.6: (a) The fitted blocking temperatures as a function of thickness for the 80×250 nm islands. As the thickness and corresponding energy barrier increase the blocking temperature also increases. There is also some hint that interaction strength has a negative effect on T_B , which is an unexpected effect. (b) The fitted H_0 as a function of thickness seems to remain fairly constant over the measured thickness range.

5.6 Conclusions

ZFC-FC measurements seem to disagree with this behaviour. More accurate modelling taking into account the interaction energies and the size distribution is required.

CHAPTER 6

Magnetic X-ray photon correlation spectroscopy
(XPCS) to track the dynamics of Artificial Spin
Ice

6.1 Introduction

Although magnetic microscopy has come far in recent years there are often certain requirements which have to be fulfilled in order to achieve optimum imaging conditions and the resolution of most techniques is still on the order of ≈ 50 nm [98]. In our case, to create a truly fluctuating system using Py, we have shrunk the island dimensions down to ≈ 30 nm. At this lengthscale imaging proves very challenging for most techniques, perhaps with the exception of Lorentz-TEM [98] and spin-polarised scanning tunnelling microscopy (SP-STM) [99]. Moreover, the stability required to do extensive statistical surveys is poorly suited to microscopy. Therefore, we have had the opportunity to develop, along with our colleagues at Diamond Light Source, a way to overcome this problem. We have borrowed a well-known technique from soft matter physicists known as photon correlation spectroscopy (PCS), where the dynamics probed, in that case, are usually on the lengthscale of visible light and lasers are used as a coherent source [100]. Here, we are more interested in the nanoscale fluctuations related to the magnetism of the sample and so X-rays with their nanomagnetic sensitivity are a natural choice; this extends PCS to the so-called XPCS (as previously discussed in section 4.4.2). The beauty of this technique is that it is a relatively powerful way to learn about complex dynamics, anomalous diffusion, jamming or glassy transitions [101]. It probes the microscopic nature of otherwise difficult-to-observe non-equilibrium properties. We have employed it here mainly in the temperature range 100 - 400 K and studied the relaxation dynamics of our ASI samples. This chapter will firstly discuss general X-ray scattering from our patterned samples and then go on to outline the efforts in setting up this new capability at the I10 beamline in Diamond, in which I was heavily involved. Firstly, the characterisation of the beam coherence will be discussed, then the review of the qualitative and quantitative main experimental results obtained from our samples, and finally a discussion of the nature of the dynamic behaviour observed in relation to the temperature dependence of our sample.

6.2 X-ray Resonant magnetic scattering of square artificial spin ice with incoherent light

Coherent light is not essential to diffract from an array of nanomagnets, it is possible to carry out XRMS measurements using incoherent light. In the first such study,

6.2 X-ray Resonant magnetic scattering of square artificial spin ice with incoherent light

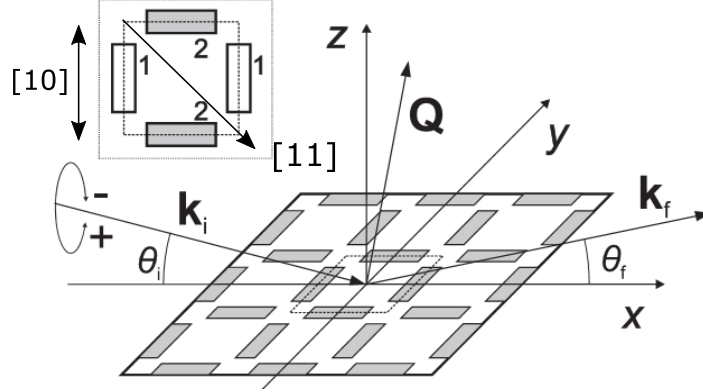


Figure 6.1: Schematic of the reflection geometry used in the scattering experiments. Q is the wave vector transfer i.e. difference between the incident and scattered X-ray wave vector, $k_f - k_i$. The structural unit cell is shown in the box. The [10] direction is defined as along the easy axis of one sublattice (white islands) and the hard axis of the other (grey islands). The [11] direction is defined as 45° to both sublattices (figure adapted from ref. [16])

Morgan *et al.* ascertained sublattice-specific information about the magnetic reversal, dependent on which order of diffraction they measured [16]. Also, in more recent work Perron *et al.* were able to identify the ground state of their spin ice from half-order peaks that appeared on magnetic resonance [17]. They had increased access to reciprocal space as they used a 2D detector. However, both of these studies are sensitive to an ensemble average of the illuminated part of the sample and microscopic disorder or dynamics are difficult to measure.

6.2.1 Bragg diffraction using a point detector

In the first instance we measured many different lattice spacings, in the range of 140 - 500 nm, using incoherent light. Scattering was performed at the I10 beamline at Diamond Light Source (UK) and all measurements were done in reflection geometry. A schematic of the geometry is shown in figure 6.1 where the structural unit cell is defined within the dotted box. The sample is in the $x - y$ plane and the scattering is within the $x - z$ plane. Incoherent light was used to scatter from the sample and ascertain the position of each sample with different lattice spacing. The arrays were patterned in 1 mm^2 areas and with a 2 mm pitch. The nominal lattice spacings used here were 140, 280, 420 and 560 nm.

6.2 X-ray Resonant magnetic scattering of square artificial spin ice with incoherent light

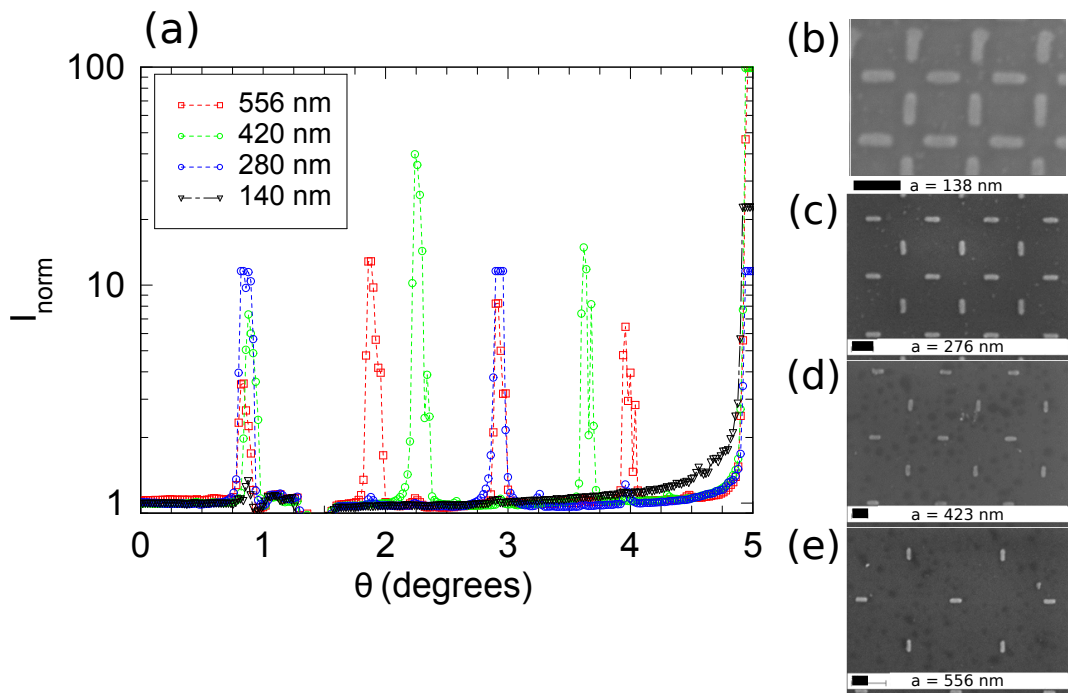


Figure 6.2: (a) In-plane Q_x rocking scans performed along the $[10]$ axis of the square array with the detector angle $= 10^\circ$. The lattice constants, a , for each sample are shown in the legend. The peaks correspond to the Bragg diffraction from the in-plane periodicity, with $Q_x = 2n\pi/a$, where n defines the order of diffraction. All intensity data has been normalised to a monitor upstream of the sample and the background baseline. (b)-(e) Scanning electron micrographs of the corresponding samples; thick black bars indicate 100 nm scale.

6.3 Coherent scattering from artificial spin ice

In order to be sensitive to in-plane periodicity, measurements were done at $2\theta = 10^\circ = \theta_i + \theta_f$, where $\theta_{i,f}$ are the incident beam and detector axis angles relative to the sample plane. During a rocking scan the θ_i is varied from sample horizon to the specular position, $\theta = 5^\circ$ in this case. This was done with the photodiode point detector, whose resolution is defined by the detector slit width. The so-called rocking curves are shown in figure 6.2(a). The in-plane scattering vector Q_x is given by [85]:

$$Q_x = (k_f - k_i)_x = \frac{2\pi}{\lambda} (\cos(2\theta - \theta_i) - \cos(\theta_i)). \quad (6.1)$$

It is possible then to use the position of the peaks to calculate the in-plane periodicity; $Q_x = 2n\pi/a$ where n is the order of diffraction and a is the lattice spacing. These were calculated from the peak positions to be 138 ± 4 , 281 ± 2 , 424 ± 2 and 563 ± 4 nm using $\lambda = 1.755$ nm (measured on the Fe L_3 edge where the energy of the X-rays is 708.6 eV). These are in good agreement with those measured from SEM; 138 ± 3 , 276 ± 2 , 423 ± 2 and 556 ± 2 nm, respectively.

6.3 Coherent scattering from artificial spin ice

6.3.1 Characterising the coherence of the beamline I10 at Diamond

The paramount requirement of the XPCS technique is to use coherent x-ray illumination. Third generation synchrotron X-rays, by their very nature, are not good coherent sources due to the width of the electron beam which produces them and the low monochromaticity of the undulator [102]. The longitudinal coherence of the beam can be improved upon by using a monochromator and the transverse coherence can be addressed by using a pinhole to select only the laterally coherent portion of the beam. Therefore, adjustments to the beamline were required in order to ensure that the light incident on the sample was coherent.

There are two conditions for the coherence in order to be sensitive to the dynamics of the scattering objects [102]. The longitudinal coherence, ξ_1 , which can also be considered as the temporal coherence, needs to be much larger than the path length, a , between different scattering centres of the sample and is defined as:

$$\xi_1 = \frac{\lambda^2}{2\delta\lambda} > a. \quad (6.2)$$

6.3 Coherent scattering from artificial spin ice

Table 6.1: Experimental parameters required for calculation of coherence properties

Description	Symbol	Value
Distance Source-Sample	Z	53.6 m
Distance Pinhole-Sample	d	270 mm
Distance Sample-CCD	D	800 mm
Pinhole Diameters	Φ	5,10,20,50 μm
CCD pixel size		$13.5 \times 13.5 \mu\text{m}^2$
Number of pixels		2048×2048
Angle of incidence	θ_i	2 - 4 $^\circ$
CCD detector angle (fixed)	2θ	9.6 $^\circ$
Angular resolution of CCD	$\delta(2\theta)$	17 μrad

In order to achieve longitudinal coherence, spectral filtering is used via the monochromating mirror, far upstream of the sample, which selects a certain portion of the spectral distribution. It is also important that the spatial coherence of the beam is not much smaller than the incident beam size, Σ_i :

$$\xi_t = \frac{\lambda Z}{\Sigma(0)} > \Sigma_i, \quad (6.3)$$

where Z is the distance from the source and $\Sigma(0)$ is the size of the source. However, both of these conditions come at the expense of flux which is why a third generation synchrotron level of brilliance (or intensity) is required; in order to be able to resolve the speckles.

Firstly, the longitudinal coherence length, ξ_l , was calculated from eq. 6.2 to be $\approx 6 \mu\text{m}$. However, the absorption length, μ^{-1} , of Fe at the resonance is $\approx 30 \text{ nm}$ [103], and the resolving power of the monochromator is $\lambda/\Delta\lambda = 3000$ which means the penetration depth, defined as $\mu^{-1} \sin^2\theta$, is much smaller than the longitudinal coherence length and, as such, satisfies the temporal coherence condition.

Secondly, the theoretical transverse coherence of the experimental setup was calculated using the formula for the beam size from ref. [102]:

$$\Sigma_{h,v}(Z) = 2.35(\sigma_{h,v} + \sigma'_{h,v}Z), \quad (6.4)$$

where h and v denote the horizontal and vertical direction, respectively, $\Sigma_{h,v}(Z)$ is the full width half maximum (FWHM) size of the beam at a distance Z from the source,

6.3 Coherent scattering from artificial spin ice

$\sigma_{h,v}$ is the FWHM size of the x-ray source and $\sigma'_{h,v}$ is its divergence (which uses a Gaussian approximation and also assumes no focussing optics). On I10 the FWHM size of the beam is $\sigma_h \times \sigma_v = 300 \mu\text{m} \times 50 \mu\text{m}$ and the divergence is $\sigma'_h \times \sigma'_v = 65 \mu\text{rad} \times 35 \mu\text{rad}$. Since perfect focussing should not change the ratio between $\Sigma_{h,v}(Z)$ and the transverse coherence length, ξ_t , it is possible to estimate the coherence from this ratio multiplied by the known beam size post-focussing. Therefore at the source ($Z = 0$) and at the diffractometer ($Z = 53.6 \text{ m}$):

$$\Sigma_h(53.6) = 8.9\text{mm}, \Sigma_h(0) = 705\mu\text{m}, \quad (6.5)$$

$$\Sigma_v(53.6) = 4.5\text{mm}, \Sigma_v(0) = 117.5\mu\text{m}. \quad (6.6)$$

The coherence, as a function of Z , is then calculated using the following:

$$\xi_{h,v}(Z) = \frac{\lambda Z}{\Sigma_{h,v}(0)}. \quad (6.7)$$

So without any focussing optics and at the Fe L_3 edge where $\lambda = 1.755 \text{ nm}$,

$$\xi_h(53.6) = \frac{1.755\text{nm} \times 53.6}{705\mu\text{m}} = 133\mu\text{m} \quad (6.8)$$

and

$$\xi_v(53.6) = \frac{1.755\text{nm} \times 53.6}{117.5\mu\text{m}} = 800\mu\text{m} \quad (6.9)$$

The corresponding ratios are,

$$\Sigma_h(53.6)/\xi_h(53.6) = 66.9, \quad (6.10)$$

$$\Sigma_v(53.6)/\xi_v(53.6) = 5.63, \quad (6.11)$$

Then, assuming these ratios remain the same for perfect focussing optics, using the size of the beam at the sample position we can approximate the coherence with focussing is:

$$\xi_h(53.6) = \frac{1\text{mm}}{66.9} = 14.9\mu\text{m}, \quad (6.12)$$

and

$$\xi_v(53.6) = \frac{100\mu\text{m}}{5.63} = 17.8\mu\text{m}, \quad (6.13)$$

These theoretical values agree well with those observed experimentally, as the tests with different sized pinholes demonstrated diffraction through the 5 and 10 μm pinholes, as shown in figure 6.3, but not through the 20 and 50 μm pinholes. The presence of the

6.3 Coherent scattering from artificial spin ice

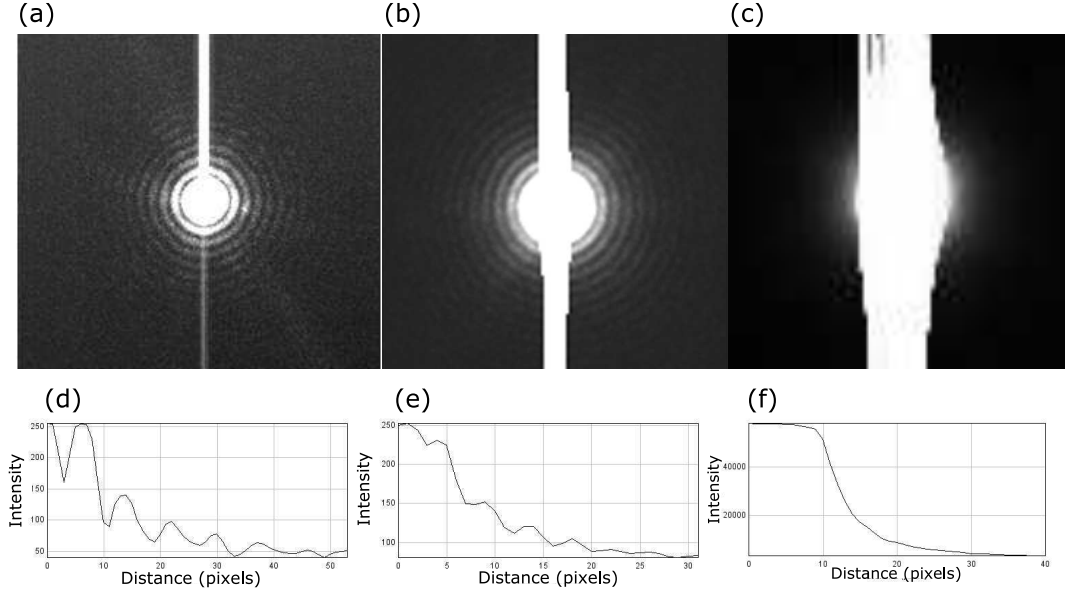


Figure 6.3: Diffraction recorded through pinholes with diameter (a) $5 \mu\text{m}$ and (b) $10 \mu\text{m}$ (c) $20 \mu\text{m}$, using the straight-through beam on to the array detector. Exposure times were 50 ms, 2 ms and 1 ms, respectively. This shows the X-ray photons are coherent through the 5 and $10 \mu\text{m}$ pinholes. Line cuts for each are plotted in (d), (e) and (f). A value for the coherence can be estimated from the contrast of the Airy pattern. In (d) and (e), the line cut is from centre of the pinhole to the fifth visible ring.

fringes confirms the coherence through the pinhole. If the smallest coherence length is $14.9 \mu\text{m}$ then a $20 \mu\text{m}$ pinhole (or larger) is too big to have a fully coherent beam across the aperture. The theoretical prediction is also supported by the observation of better coherence obtained in the vertical direction compared to the horizontal for the $10 \mu\text{m}$ pinhole, as discussed below.

The experimental approach used to evaluate the coherence was to test a range of pinhole sizes. In order to observe diffraction the detector was placed in straight-through beam position and in the far-field of the pinhole. The calculated near-field limit is defined as $\phi^2/\lambda \approx 60 \text{ mm}$ for the $10 \mu\text{m}$ pinhole. The sample was removed and the total distance between the pinhole and the CCD was 350 mm. As this is nearly six times larger than the near-field limit. We were able to observe the Airy diffraction rings from the 5 and $10 \mu\text{m}$ pinhole as shown in figure 6.3(a) and (b) but hardly through the $20 \mu\text{m}$ pin hole as shown in (c). The visibility of the diffraction rings can be used to calculate the experimental coherence [102]. The contrast, A , of the rings can be

6.3 Coherent scattering from artificial spin ice

measured by taking a line-cut through the pattern and is estimated by:

$$A = \left(\frac{I_{\max} - I_{\min}}{I_{\max} + I_{\min}} \right)^2. \quad (6.14)$$

This is the same experimental coherence factor which relates the intensity-intensity autocorrelation function to the field-field autocorrelation function, g_1 , via the Siegert relation [104]:

$$g_2(Q, \tau) = 1 + A|g_1(Q, \tau)|^2. \quad (6.15)$$

An example of the line plot used to estimate the coherence are shown in (d) and (e). For the 5 μm pinhole, $A = 0.22 \pm 0.01$ was calculated using just the first visible ring at many different positions from the centre. This gives a value of coherence, $\xi = 22 \pm 2 \mu\text{m}$, which is larger than that expected from the theoretical calculation. For the 10 μm pinhole, the diffraction is less uniform radially. Therefore, two A values were calculated in the horizontal and vertical direction; $A_{\text{horizontal}} = 0.046 \pm 0.002$ and $A_{\text{vertical}} = 0.082 \pm 0.002$. By multiplying these with the size of the x-ray beam at the exit slits coherence lengths of 9.2 μm and 8.2 μm respectively are obtained. This is a little less than the predicted value of 14.9 μm , but agrees well with the results of the pinhole tests, which clearly showed diffraction from the 5 and 10 μm pinholes but not for the larger 20 and 50 μm . The higher value obtained for the 5 μm pinhole could be due to the real coherence of the beam is a value quite close to 10 μm . Therefore, it is likely that the entire beam through the 5 μm pinhole is coherent whereas the 10 μm pinhole may not be 100% coherent. Nevertheless, the 10 μm pinhole was chosen to obtain enough intensity and make sure that a statistically meaningful number of islands were illuminated.

6.3.2 Qualitative time dependence of the speckle pattern

When coherent illumination is used then speckle contrast can be observed in the diffraction spot, arising from the randomly distributed regions of sample introducing different phase shifts into the scattering of the incident light [105]. This speckle is visible in the detailed views of the diffraction spots shown at the top of figure 6.4. As the random regions fluctuate in time then so will the speckle, allowing the dynamics of the system to be studied in a statistical manner, an effect that has long been used with visible light to study ageing and relaxation phenomena in soft matter [106].

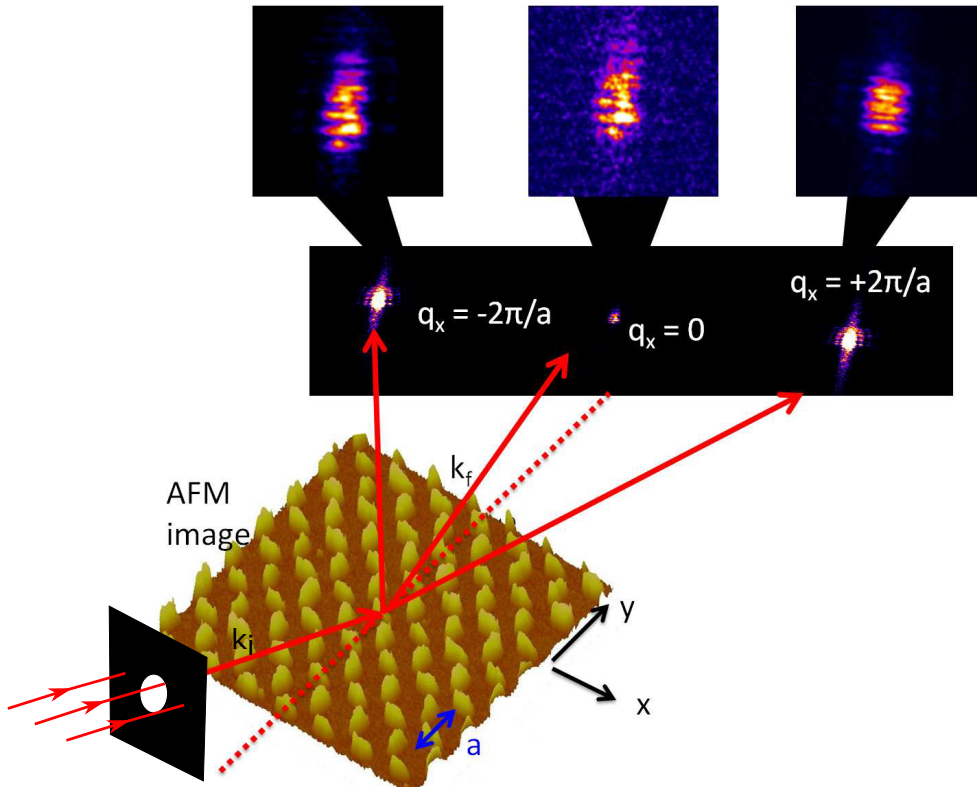


Figure 6.4: Schematic of the experimental setup showing the incoming X-ray beam with wave vector k_i travels through the pinhole and the scattered X-ray wave vector k_f . The three main spots in the row above the specular reflection are shown here. Since each diffraction spot arises from the small, disordered region of the sample that has been coherently illuminated, it contains speckle contrast. The illuminated area was between 200 - 300 μm , dependent on the exact incident angle. The lattice constant is indicated by a .

6.3 Coherent scattering from artificial spin ice

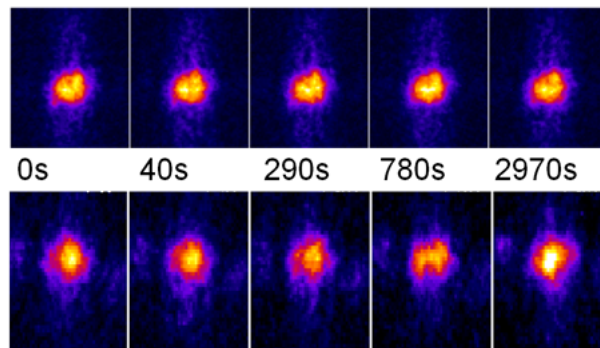


Figure 6.5: Time evolution of the speckle pattern for two different sized island samples at $T = 300$ K. The top row of panels is for an ASI with $35 \text{ nm} \times 90 \text{ nm}$ islands and the bottom panel shows speckle patterns from an ASI made up of $30 \text{ nm} \times 70 \text{ nm}$ islands.

In recent condensed matter XPCS experiments, hard X-rays have been used to study charge density waves associated with antiferromagnetic domains in Cr [107] giving an indirect measurement of magnetic dynamics. Soft X-rays at the M_5 resonance of Ho revealed antiferromagnetic domain fluctuations in a thin film of that metal [108], whilst the jamming of spiral magnetic domains in a Y-Dy-Y trilayer was revealed in the stretched exponential correlations studied using soft X-rays at the Dy M_5 resonance [109]. There have also been studies at the Co L_3 resonance using small-angle X-ray scattering (SAXS) geometry to study the effects of disorder on the domain pattern of multilayer perpendicular Co/Pt films [110]. The same group have also measured the dynamics associated with the surface reconstruction of Au and Pt monolayer films [111; 112]. Here we have implemented XPCS using soft X-rays at the Fe L_3 resonance to study the dynamics of nanomagnets fabricated from the ferromagnetic material, permalloy, and reveal the dynamics of the ASI array as a function of temperature.

In figure 6.5 we show a qualitative comparison of the changes in the speckle pattern over 2970 s for islands with a lateral size of $35 \text{ nm} \times 90 \text{ nm}$ compared to slightly smaller $30 \text{ nm} \times 70 \text{ nm}$ islands. There is almost no change in the speckle pattern over the whole measurement time for the larger volume islands. On the other hand, for the smaller islands the pattern slowly changes and decorrelates from the first image. There is very little change after 40 s, but the pattern has changed noticeably after 290 s and is completely different for times of 780 s or longer. Thus these smaller islands, with their lower energy barriers to reversal, are thermally active on timescales of hundreds of

seconds. This is broadly to be expected since the rate at which (non-interacting) islands flip can be approximated by the superparamagnetic relation, eq. 1.5 [26; 27]. Smaller volumes thus lead to shorter timescales τ on which the magnetic moment direction of an island is stable.

It can be seen from figure 6.6 that for a time sequence at a temperature where dynamics have been observed in the speckle pattern, the same measurement carried out off-resonance showed no change. This is because there is greatly reduced sensitivity to changing magnetic states when the energy of the X-rays is not on an absorption edge. The data for off-resonance is shown in the top panel and the on-resonance is in the bottom panel. Thus, the changes in the speckle are confirmed to be due to the magnetic fluctuations within the sample.

6.3.3 Quantitative analysis of the temperature dependence of g_2 function

In order to be more quantitative it is possible to calculate how quickly these dynamics proceed. We measured Py square ASI with islands of 30 nm \times 70 nm and 8 nm thick, as shown in 6.7(a). We calculated the intensity-intensity autocorrelation function in the standard way [100]:

$$g_2(Q, \tau) = \frac{\langle I(t')I(t'+\tau) \rangle_{t'}}{\langle I(t')^2 \rangle_{t'}} = 1 + A |F(Q, \tau)|^2 \quad (6.16)$$

where $I(Q, t')$ is the intensity at wave vector Q at a time t' , τ is the time delay, and $\langle \dots \rangle_{t'}$ indicates a time average. $F(Q, t')$ is the so-called intermediate scattering function, and A is a measure of the speckle contrast. This g_2 function was calculated for each pixel (value of Q) within the speckle pattern where the intensity is above the background and averaged over all such pixels as outlined in the methods section 4.4.2. The resulting g_2 functions measured at different temperatures are plotted in figure 6.7(b).

The g_2 curves were fitted with a heterodyne model, as the experimental set-up means that the static signal, simply coming from the structure of the array acts as a reference beam and is mixed with the fluctuating magnetic signal during the measurement [73]:

$$g_2 = 1 + A \cos(\omega\tau) e^{-(\tau/t_r)^\beta}, \quad (6.17)$$

where τ is the delay time, t_r is the characteristic relaxation time and ω is an oscillation frequency. The value of ω was found to be in the range ≈ 0.001 - 0.0002 rads^{-1} , corresponding to a time period, $2\pi/\omega = 3141$ - 15707 s (≈ 1 - 4 hrs), which correlates well

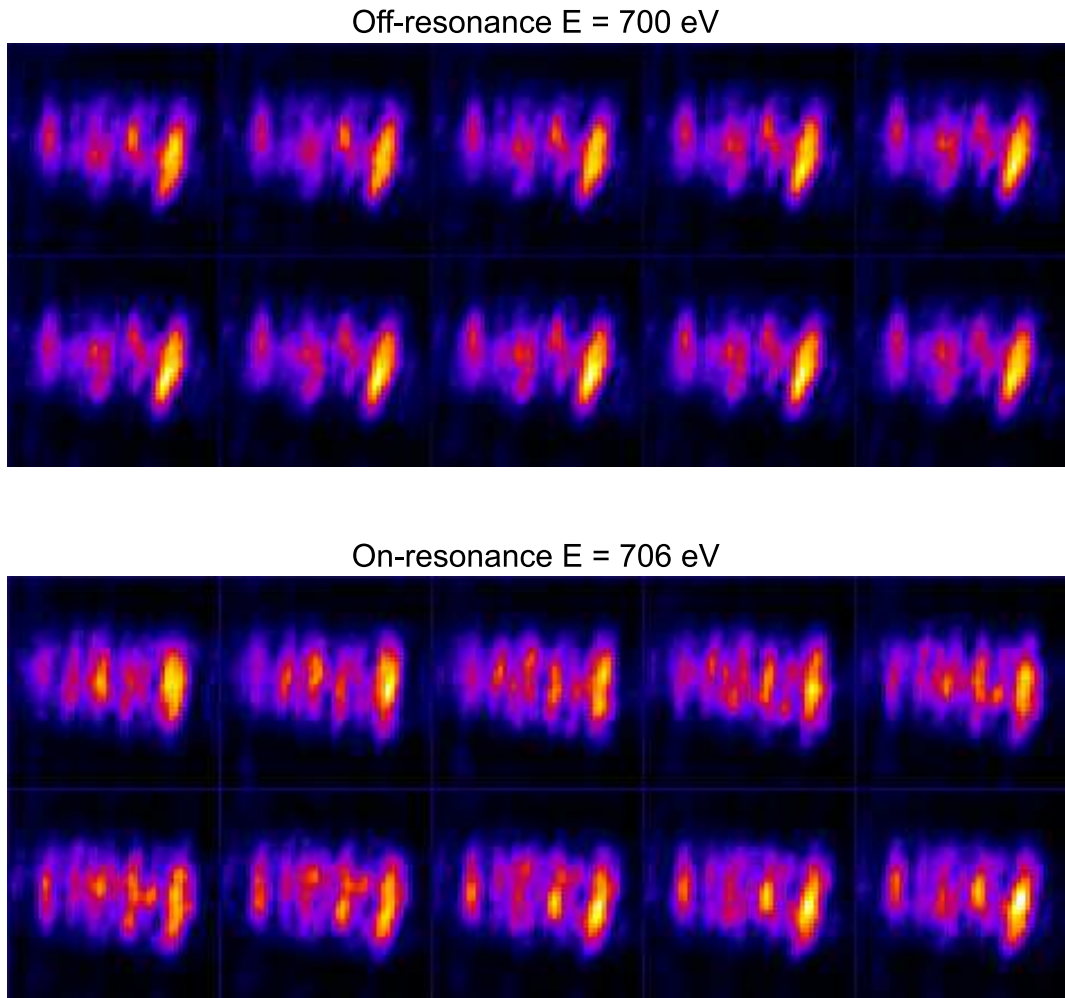
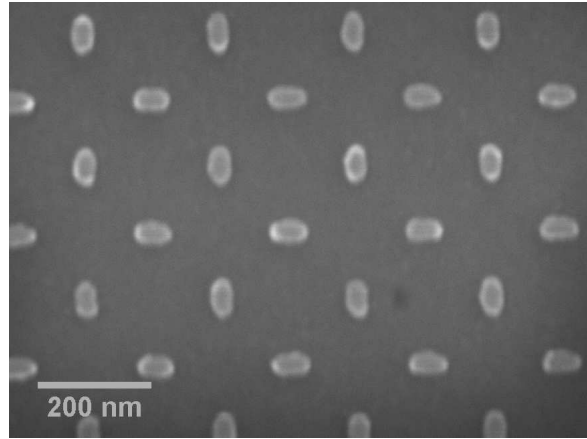
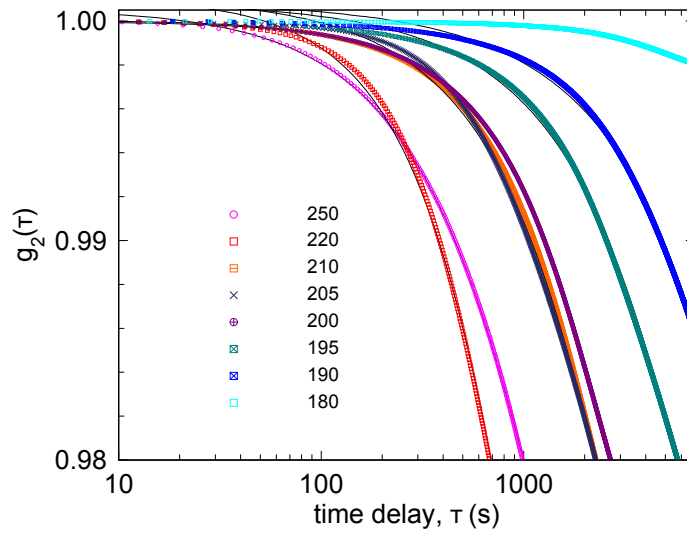


Figure 6.6: Each panel shows a series of images taken with 100 ms exposure every 510 s, therefore the 10 image sequence corresponds to ≈ 1.4 hrs. The top panel shows the measurement carried out off-resonance ($E= 700$ eV) where the image shows no change in the intensity configuration over the measurement time. The lower panel is measured on-resonance ($E= 706$ eV) where the X-rays are sensitive to the magnetic fluctuations and the changes between each image are visible as a change in the distribution of the intensity across the speckle pattern.

6.3 Coherent scattering from artificial spin ice



(a)



(b)

Figure 6.7: (a) A scanning electron micrograph showing the sample measured, which had islands $30 \text{ nm} \times 70 \text{ nm}$, 8 nm-thick permalloy arranged in a square ice pattern with lattice spacing $a = 240 \text{ nm}$. (b) Temperature dependent g_2 autocorrelation functions, normalised to their initial value. The black lines are fits to a heterodyne model described in the text.

6.3 Coherent scattering from artificial spin ice

with the total measurement time. The speckle contrast, A , was found in the range 0.02 - 0.05 which agrees with that found in the pinhole tests and the fitted β in these measurements was ≈ 1 , indicating equilibrated behaviour. The function is fairly flat or static at 180 K suggesting the relaxation time is longer than the time of measurement ($\cong 3.8$ hrs). The correlation function changes faster and faster with increasing temperature, as can be seen from the initial slope and the drop-off in figure 6.7(b). The data taken at 295 K and 305 K were flat at a value of 1, suggesting at these high temperatures we are not sensitive to the relaxation processes happening on a timescale faster than the smallest acquisition time (≈ 50 ms). The fitted relaxation times, t_r , for temperatures between 190 and 250 K are shown in figure 6.8. There is a large range of timescales probed with the longest relaxation time, $t_r(190\text{K}) = 19,600$ s down to $t_r(250\text{K}) = 1390$ s. The data cannot be fitted with a simple Néel-Brown relaxation, instead the data is fitted to a Vogel-Fulcher law [113]:

$$\tau = \tau_0 e^{T_A/(T-T_0)}, \quad (6.18)$$

where T_A is the activation temperature and T_0 is the freezing temperature, these were found to be 40 ± 10 K and 178 ± 5 K, respectively.

6.3.4 Interpretation of the observed Vogel-Fulcher behaviour

As is shown in figure 6.8 the Néel-Brown behaviour expected from non-interacting superparamagnetic (SPM) systems does not fit well the data (red line). The Vogel-Fulcher (V-F) law captures the low temperature detail much more accurately. The Vogel-Fulcher law has been found to fit a lot of different data sets very well empirically, such as spin glasses, super-cooled organic liquids, metallic liquids and glassy polymer systems [114]. Although, this law does well to describe an extensive range of experimental situations, it is often difficult to derive from a microscopic picture.

Following the work of Shtrikman and Wohlfarth (S-W) [97], as discussed in section 5.5, it is possible to define a weak and strong interaction regime for a system which shows Vogel-Fulcher behaviour. For this system, we can estimate $T_K = 5.6 \pm 0.8 \times 10^4$ K, from eq. 5.3 where KV was calculated assuming $M_S(\text{Py}) = 860$ kA/m, $\Delta N_D = 0.1$ from ref. [115] and the islands volume, V , is $30 \times 70 \times 8$ nm³. Our fitted T_0 is 178 K which is much smaller than both estimates of T_K , indicating the system is very weakly coupled. This is to be expected for such a large lattice spacing relative to the island

6.3 Coherent scattering from artificial spin ice

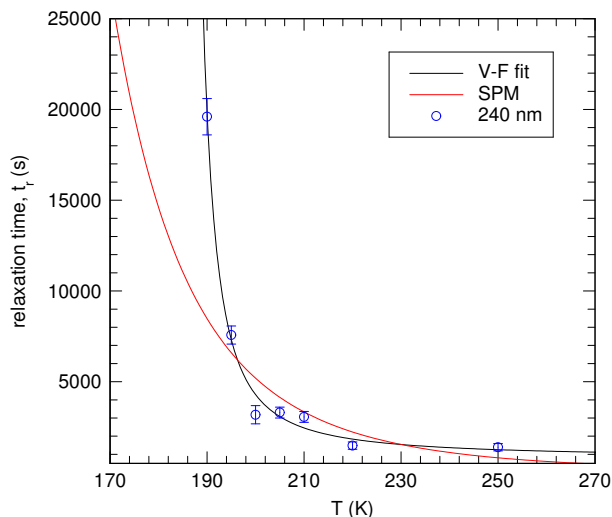


Figure 6.8: Relaxation times as a function of temperature, fitted to a Vogel-Fulcher (V-F) function showing faster dynamics with increased temperature. Also plotted is the superparamagnetic (SPM) function which would indicate simple Arrhenius behaviour.

size [116]. We calculated T_A to be 900 ± 200 K (or 410 ± 50 K for $M_S = 0.6M_S(\text{Py})$), using $\ln(t_m/t_0)k_B T_A = KV$ where the measurement time, t_m , is taken as the average total measurement time (2 hr) and t_0 is the inverse attempt frequency. This is more than an order of magnitude larger than the fitted T_A of 40 K. This large discrepancy is not entirely unexpected due to the large error associated with estimation of KV , in particular N_D has a large dependence on the assumption of a perfect ellipsoid and doesn't account for the disorder inherent in the island from the nanofabrication. The roughness here begins to approach the size of the island for this sample. Recent studies have found the roughness can act to create nucleation sites for non-uniform modes of reversal [117]. The measured T_A could then indicate a much smaller volume involved in the activation barrier, leading to non-collinear magnetic structure or curling within the island. The fitted T_A would require a reduction of the energy barrier by a factor of 20.

In order to further investigate the origin of the low activation temperature we measured the same sample by other means. We carried out extensive magnetometry using a SQUID-VSM. Firstly we measured the zero-field cooled (ZFC) and field-cooled (FC) magnetic moment as a function of temperature which is plotted in figure 6.9(a). From this data we can see there are two separate increases in the moment indicating

6.3 Coherent scattering from artificial spin ice

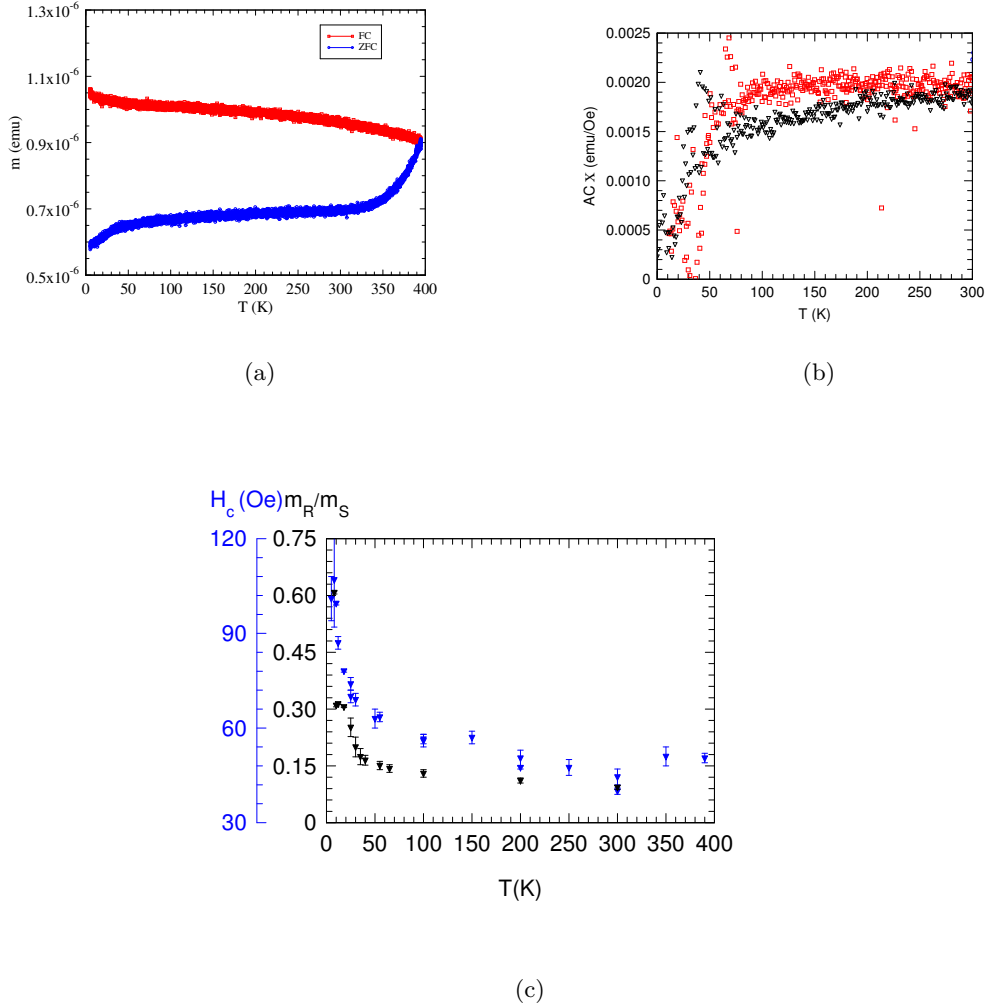


Figure 6.9: (a) ZFC-FC curve as measured along the [10] axis of the ASI. (b) AC susceptibility, χ , measured at 257 Hz with 10 Oe field after a ZFC procedure. Both show a feature ≈ 40 K similar to the activation temperature found in the Vogel-Fulcher fit. (c) m_R/m_S plotted versus temperature (black triangles) and the coercivity, H_c , (blue triangles), both show an abrupt decrease up to 40 K then a gradual decrease on further warming.

6.3 Coherent scattering from artificial spin ice

a bimodal distribution of the energy barriers, one around $T = 40$ K and the other at a temperature above 395 K. These two features indicate two energy scales involved in the process of unblocking the moment. The AC susceptibility, χ , as a function of temperature is plotted in figure 6.9(b), this was done at a measurement frequency of 257 Hz and an AC amplitude field of 10 Oe. This measurement also shows a feature around 40 K, a similar temperature to the T_A from the Vogel-Fulcher fit. Comparably, the coercive field H_c and the remanent moment (normalised to the saturated moment) plotted as a function of temperature in 6.9(c), show a steep decrease between 5-40 K, with a much more gradual decrease above this temperature. These data indicate a much smaller energy barrier than that defined by the full volume.

In order to investigate the activation volume and reversal properties of the nanoislands by considering the internal spin structure we carried out reversal simulations using the exact SEM image of the islands of this sample. We used the MuMax micromagnetic simulation package [88]. Firstly, the island was initiated in a saturated state along the negative x -direction. The field was then increased from zero to 100 mT, in steps of 0.5 mT and allowed to relax before going to the next field step. Standard values for Py were used: M_S as above; exchange constant, $A=13$ pJ/m; and damping constant, $\alpha = 0.05$. It is clear from the simulation that the activation begins in a small part of the island, around a 10 nm portion at the less-uniform end. The magnetisation here starts to curl in the positive y -direction, indicated by the orange-yellow colour, before flipping completely the island magnetisation (as shown in figure 6.10). Although the situation we probe in the XPCS experiments is purely thermally driven in contrast to the situation simulated by MuMax, we can still try to equate the energies. In the simulation as the full M_S value of Py was used, the coercive fields observed are a factor of 10 different. The energy to curl the end of the island was extracted from the MuMax simulation to be $E_{curl} = 2.2 \times 10^{-19}$ J, however this was calculated from the Zeeman term ($E_Z = M_S \mu_0 H$). If we divide E_{curl} by the reduced factors from the experimental values of M_S and H_c this reduces to $E_{curl} = 1.2 \pm 0.3 \times 10^{-20}$ J. This corresponds to a temperature 70 ± 20 K, in reasonable agreement with that observed. Incorporating real temperature and additional information about the internal structure into the simulations would help to visualise these dynamic edges at low temperature to further support this argument.

In order to see if this is representative behaviour, we carried out the same sim-

6.3 Coherent scattering from artificial spin ice

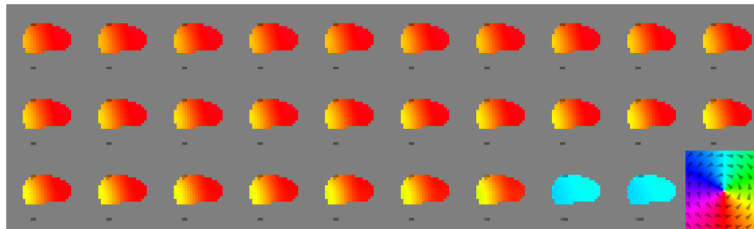


Figure 6.10: Micromagnetic simulation of the reversal under applied field of an island at $T = 0$ K. The island was taken directly from thresholding an SEM image and therefore its approximate dimensions are 30×70 nm. The field steps shown are between 37.5 and 80.0 mT. In the last three panels a small region, roughly 10 nm from the end of the island, initiates the reversal supporting evidence of an activation volume for reversal much smaller than the whole island volume. The colour key indicates the direction of the magnetisation vector. A $2 \text{ nm} \times 2 \text{ nm}$ mesh size was used for the calculation with standard exchange stiffness and magnetisation values for permalloy.

ulations on different randomly chosen individual islands, as is shown in figure 6.11. There is a quite a broad distribution of switching fields dependent on the shape and uniformity of the islands. Also shown are the corresponding islands used, and their 2D magnetisation map at the field step just before the full reversal occurs. It can be seen that island 2 (red box) rotates almost coherently, in an Stoner-Wohlfarth manner, having $\mu_0 H_c = 113$ mT. However, dependent on the exact shape disorder of the island, non-uniformity at the ends can also be a dominant property. The reversal by a small portion at the end of the island, as shown in island 1 (green box), the same as shown in figure 6.10, acts to lower the switching field by 36 mT. For the kidney-shape of island 3 (black box), this non-uniformity actually acts to increase the switching field by 30 mT, compared to the coherent case. Also, shown is the case for two parallel islands, where a difference in their switching fields manifests as a step feature in the hysteresis curve.

Finally, we can also consider the freezing temperature as a measure of the interaction field and, following that of ref. [97], it can be defined as:

$$T_0 = k_B^{-1} E_i^2 / E_K. \quad (6.19)$$

Using the parameters from the V-F fit, *i.e.* $T_0 = 178$ K and $T_A = 40$ K and $E_K = k_B T_A$, we find $E_i = \sqrt{T_0 k_B^2 T_A} \cong 1.2 \times 10^{-21}$ J. This energy is comparable to the dipolar interaction energy which was calculated for a pair of parallel and anti-parallel islands using eq. 1.9, $E_{\text{dipolar}} = 8.6 \times 10^{-21}$ J. The parameters used were $V_{\text{island}} = 2 \times 10^{-23}$ m³

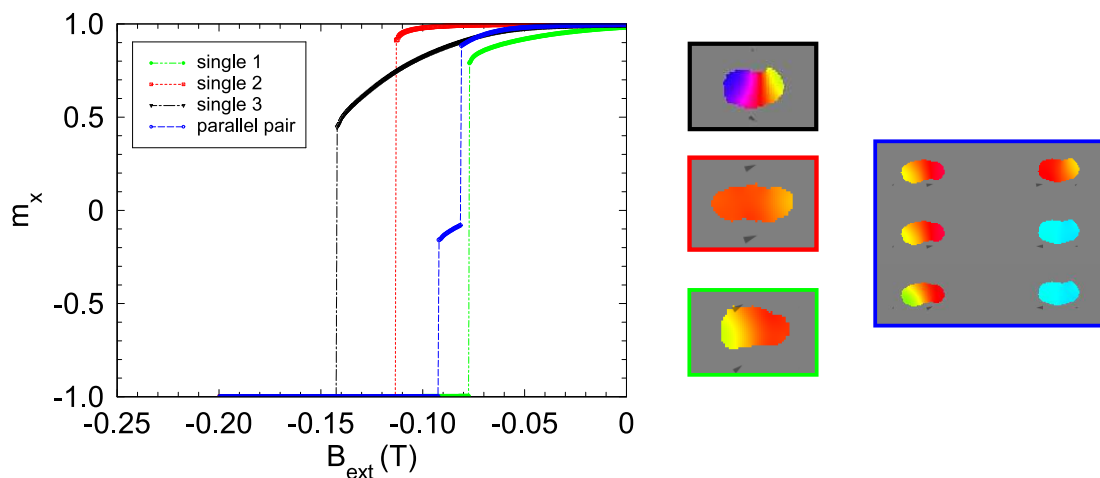


Figure 6.11: Simulated half hysteresis using SEM of different islands with the corresponding last image before the flip shown in the same coloured box as the curve on the graph.

and r , the separation is taken as the lattice constant, $a = 240$ nm. The actual value of the dipolar energy may be smaller than this due to the observed reduction in $M_S V$, it would require 40% of the bulk value for good agreement which is not unrealistic as shown in the previous chapter.

In summary, the magnetometry data and simulations support the idea of non-coherent rotation in some of the islands, leading to an activation volume much smaller than the full island volume which accounts for the T_A from the V-F fit. The fitted T_0 offers a way to characterise the strength of interaction between the islands and a comparison with the calculated T_K indicates the islands are only weakly interacting. The large dependence of the exact magnetic texture within the island on the demagnetising fields and interaction could account for the observed behaviour. This could also explain examples in the literature where activation and thermal behaviour have been observed at much lower temperatures than would be indicated by calculating the energy barrier using the full island moment.

6.4 Conclusions

In our XPCS experiments, we have measured dynamics in the low temperature region and seen the systematic decrease of relaxation time with increased temperature for Py artificial spin ice. In our weakly interacting system we have shown that the XPCS

technique can probe Vogel-Fulcher behaviour and that the reversal of an island at this size can proceed in a non-coherent fashion. This lowered energy barrier for dynamic curling within the islands themselves is induced by the inherent disorder from the patterning process. We have identified two temperature regimes in our samples from the ZFC data, which display evidence for two distributions of blocking temperature. The low- T range corresponds to non-coherent reversing islands and the reversal of the more elliptical Ising-like nanomagnets corresponds to the higher- T range. This has further been confirmed by MuMax simulations of the actual SEM images of the islands from the sample. The possibility of the reversal being initiated by a smaller volume, not equal to the full volume barrier of the island is proposed although further investigation into the exact process, for example, by direct visualisation using L-TEM is called for [118].

We have also used the measured freezing temperature, T_0 , to further confirm weak interaction in the measured system and reproduced the observed activation temperature, T_A , using both DC and AC magnetometry. We have demonstrated the potential of magnetic XPCS to measure the nature of dynamics of nanostructures beyond current microscopic capabilities which may pave the way for similar studies of magnetic nanostructures of this scale; such as skyrmions, interacting nanoparticles, and the boundaries between magnetic and non-magnetic phases.

CHAPTER 7

Nanomagnetic field-driven thermal mobility in
artificial spin ice

7.1 Introduction

Many of the imaging methods that have been suited to probe the dynamics of ASI so far involve the manipulation of electrons, such as PEEM and L-TEM where it is only possible to apply small magnetic fields (≈ 100 Oe) during imaging due to the deflection of the electrons. Therefore, there has been limited exploration of the combined role of magnetic field and varied temperature. Also, due to the high temperatures or low moment materials required for thermal behaviour, MFM has not been suitable for dynamic studies as the stray fields are too small to detect and the tip would also perturb the fluctuating states. Due to the nature of TXM, as a ‘photon-in-photon-out’ method, it presents a unique opportunity to probe the vertex populations in the rich phase space which has become available to us using this alternative method.

7.1.1 Experimental set-up

All the experiments described in this chapter were done at the full-field soft X-ray microscope, XM-1, located at beamline 6.1.2 at the Advanced Light Source as described in section 4.4.1. All images were taken at the Co L_3 edge (778 eV) with circularly polarised X-rays of a fixed helicity. A nanomagnet whose moment is oriented parallel to the X-ray propagation vector will have absorption different from one that has its an anti-parallel, which provides the magnetic contrast mechanism. Since this method requires differences in magnetisation along the X-ray beam axis, usually the technique is used for samples whose moment lies out-of-the-plane. In order to be sensitive to the in-plane magnetism of our samples it was necessary to tilt the sample 30° out of the plane (figure 7.1(a)). A sample CCD image is shown in figure 7.1(b) and the corresponding magnetic contrast image is shown in figure 7.1(c). This is obtained after dividing two consecutive images with increasing reversal field, darker contrast indicates those islands that have switched their moment orientation during the field step. It can be seen from this image that the non-uniform illumination means that only part of the field of view can be used for the magnetic imaging. The sample is aligned in such a way that the field is applied in the film plane and along a diagonal of the ASI array, so that all islands have their magnetic easy axis, which is defined by their shape, at 45° to the field direction. All experiments were carried out in this general set-up. The results from the following three sections can be found in a recent publication [91].

7.2 Thermal behaviour at room temperature using field-modified barrier height

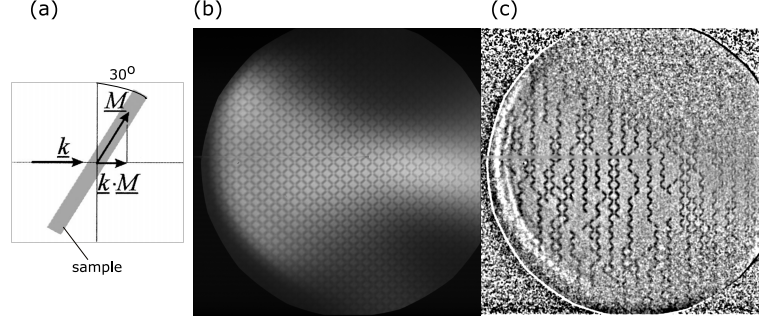


Figure 7.1: (a) A plan view of the sample showing the measurement geometry where a 30° tilt out-of-the-plane is necessary to measure in-plane magnetism at the XM-1 microscope; \mathbf{k} represents the X-ray propagation vector and \mathbf{M} is the vector of magnetisation of the sample. Contrast scales with $\mathbf{k} \cdot \mathbf{M}$. (b) A raw transmission X-ray image from the XM-1 microscope of an square artificial spin ice of 80×250 nm islands. (c) A difference image between the raw absorption image at saturation and one close to the coercive field of the sample where it can be seen that around half the visible islands have switched and are black, whilst the remaining ones are yet to switch and show no contrast. The field of view is $10 \mu\text{m}$.

7.2 Thermal behaviour at room temperature using field-modified barrier height

In the first experiments, the islands were $80 \text{ nm} \times 250 \text{ nm}$ islands, which are 10 nm thick, so the demagnetisation factor $\Delta N_D = 0.04$ [115]. With the saturation magnetisation of CoFeB measured by SQUID-vibrating sample magnetometry as $M_S \approx 1.0 \pm 0.1 \text{ MA/m}$, we find the in-plane shape anisotropy $K = 25.1 \text{ kJ/m}^3$, yielding an energy barrier to coherent rotation reversal of $KV/k_B \approx 3.6 \times 10^5 \text{ K}$. At $T = 300 \text{ K}$, the ratio of $KV/k_B T \approx 1210$. At this ratio, thermal relaxation will be many orders of magnitude too slow to observe, according to the Néel-Brown equation.

According to Bean and Livingston [90], there is a simple modification of ΔE by a factor which depends on the magnitude of the applied magnetic field,

$$\Delta E = KV \left(1 - \frac{H}{H_c} \right)^n, \quad (7.1)$$

where H_0 is the characteristic field, the exponent n is dependent on the direction of the applied field in relation to easy axis of the particle. For example, $n=2$ if the field is along the easy axis of the island [119].

7.3 Application of temperature with on-membrane heating

Hence, we attempted to observe thermally activated flipping events by adjusting the barrier height with magnetic field according to eq. 7.1. We measured the sample with 0.6 s exposure time and 5 averages per image, giving a acquisition time of 3 s. The sample was first saturated in one direction and then an opposite field applied that was 90 % of H_c , we then continued taking images for a further 40 s. Shown in figure 7.2 is the cumulative number of flips observed at each waiting time, which grows linearly with time. The slope of a straight line fit to these data gives the observed flipping rate under these conditions, which was measured to be $r = 0.12 \pm 0.02 \text{ s}^{-1}$. Inserting the rate for one island over the total number of flipped islands, N , $r/N = 1/\tau$ into eq. 1.5 yields a ratio $\Delta E/k_B T = 20.89 \pm 0.02$, if we assume $f_0 = 10 \text{ GHz}$.

Here, the field is at 45° to easy axis of all the islands. Under these circumstances, Harrell has shown that $n \sim 1.45$, [120] close to the $n = 3/2$ value of the Victora expansion [28]. Assuming that $H_0 \approx H_c$ for these athermal islands, inserting $H/H_c = 0.9$ into eq. 7.1 yields an energy barrier ΔE that should be only 3.5 % of the zero field value. This implies a ratio $\Delta E/k_B T = 23$ which agrees reasonably well with the measured value, given the extreme sensitivity of the exponential function in eq. 7.1 to its argument. This agreement is to some extent fortuitous given the uncertainty over the true value of quantities such as f_0 , and the fact that we have neglected the inter-island coupling. Assuming an activation volume smaller than the real island volume can also explain the discrepancy: the measured value of $\Delta E/k_B T$ implies that the activation volume is approximately half of the true volume, an idea explored in detail in section 6.3.4 of the previous chapter.

7.3 Application of temperature with on-membrane heating

An on-membrane heater and thermometer were patterned via nano-fabrication, as previously discussed (section 4.2.4), and could reliably reach temperatures in excess of 700 K. The calibration of thermometer was done in two stages. Firstly, the membrane sample was submerged in a non-conductive liquid, such as isopropanol or deionised (DI) water, then the liquid was heated whilst the resistance of the thermometer and temperature of the liquid were measured. A thermocouple also submerged in the same beaker was used to measure the temperature of the liquid. The thermometer resistance

7.4 Reversal as a function of temperature

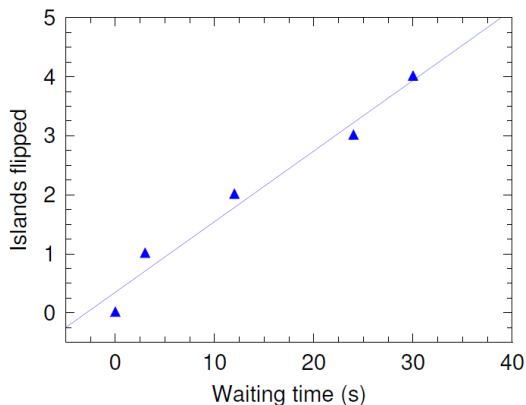


Figure 7.2: Thermally-assisted flipping events measured at 300 K, as a function of waiting time, after applying a reversal field equivalent to 90% of the coercivity.

had a very linear dependence on temperature as shown in figure 7.3(a), which could be extrapolated to high temperatures as should be valid for platinum, as it is often used in thermometry for this reason [121]. The sample is then tested in air by again measuring the resistance of the thermometer but this time as a function of different applied heater currents. As the power output of the heater is $P = I^2 R$, the temperature of the membrane follows a square law with respect to the current, as shown in figure 7.3(b). As the power is also proportional to the resistance of the heater, heating increases with decreased thickness of the heater (figure 7.3(c)). This is at the expense of a larger working voltages at the power source, therefore an optimum thickness of 60 nm was used. This on-membrane heater and thermometer assembly allowed experiments to be carried out over an extensive range of temperatures. According to the membrane specification, temperatures as high as 1473 K can be reached, however we found degradation of the magnetic material before this at ≈ 710 K due to oxidation in air. Therefore, all experiments were carried out below this threshold.

7.4 Reversal as a function of temperature

7.4.1 Hysteresis

In order to see how elevated temperature affected the reversal of ASI we again patterned $80 \text{ nm} \times 250 \text{ nm}$ islands of CoFeB with a lattice spacing of 500 nm. The sample was first saturated along the negative [11] direction and then the field was reversed in the

7.4 Reversal as a function of temperature

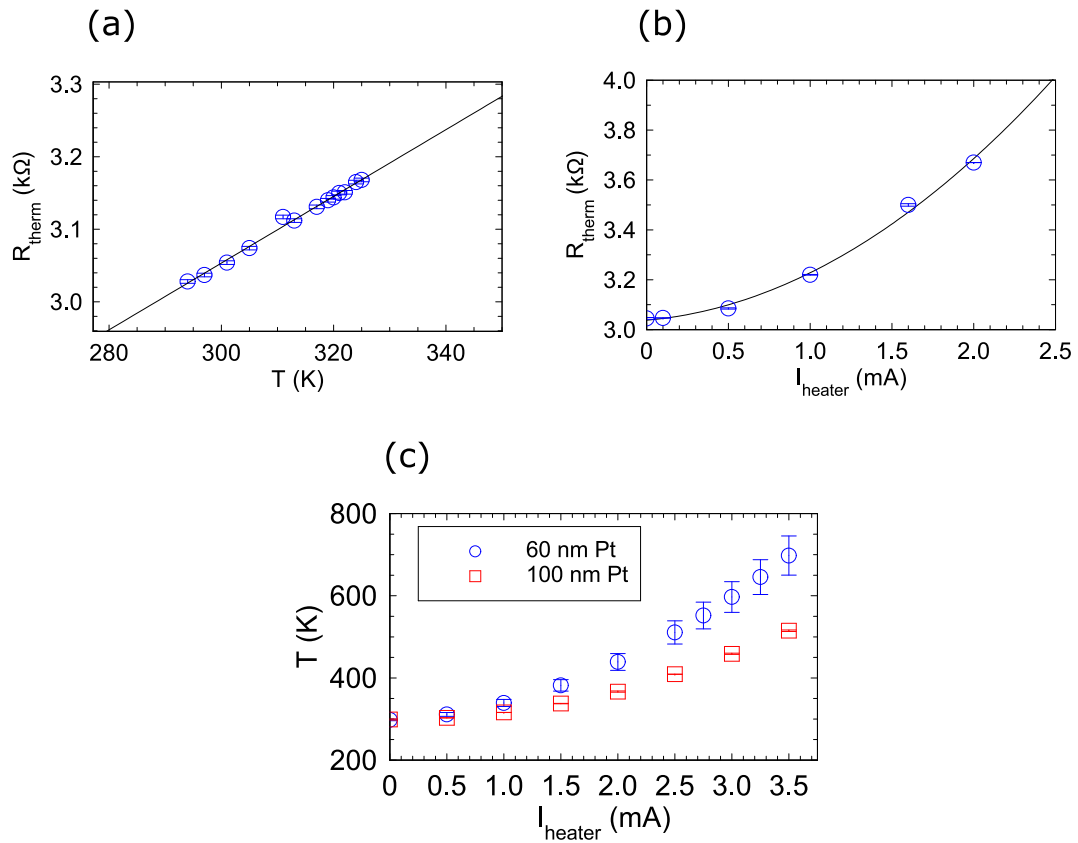


Figure 7.3: (a) Resistance of the thermometer when submerged in DI water as a function of the liquid temperature. Black line is a linear fit to the data. (b) The resistance of the thermometer as a function of the applied heater current in air, the line of best fit for a quadratic is also shown. (c) A comparison between the temperatures which can be obtained from different thicknesses of Pt. The thicker Pt has a lower resistance and therefore produces less heating power for the same applied current.

7.4 Reversal as a function of temperature

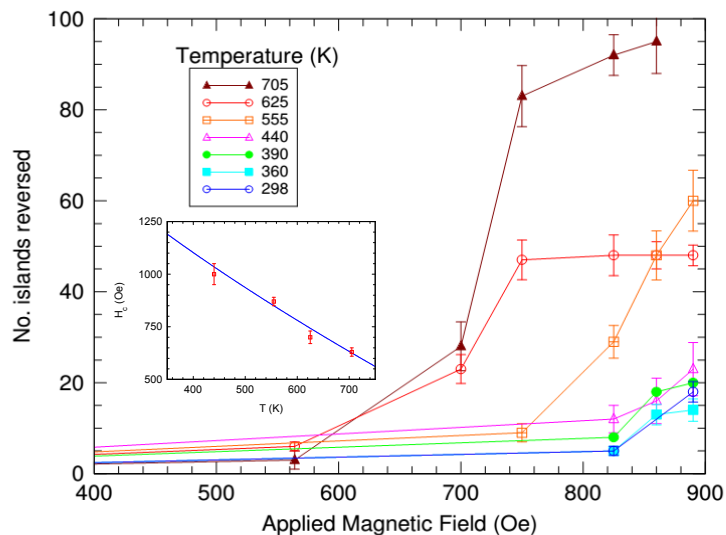


Figure 7.4: Number of flipped islands as the applied field H is increased towards positive saturation after negative saturation for various different elevated array temperatures (lines to guide the eye). (Inset) Coercive field H_c as a function of temperature T . The line is a fit to the data as described in the text.

positive direction, tracing out a hysteresis loop for the array. Figure 7.4 shows the dependence of the hysteresis for this sample at different applied temperatures. This data shows the decrease in the field value at which the reversal is initiated but also how quickly it propagates as a function of temperature. It can be seen from the curves that there is little change between the data at room temperature and 440 K. However, as the temperature was increased further the reversal began at lower field values indicating a reduced effective barrier height for the individual islands. There is also an increase in the number of islands which reversed within the field of view. This data is replotted as coercivity as a function of temperature in the inset. There is a trend in decreasing coercivity of the array with temperature and we attribute this to the onset of dynamics, similar to the pre-melting behaviour observed by Kapaklis *et al.* using a macroscopic magneto-optic measurement [61]. The use of an imaging method means that we are able to see exactly how the array begins to ‘melt’ and track the different vertex populations as they happen.

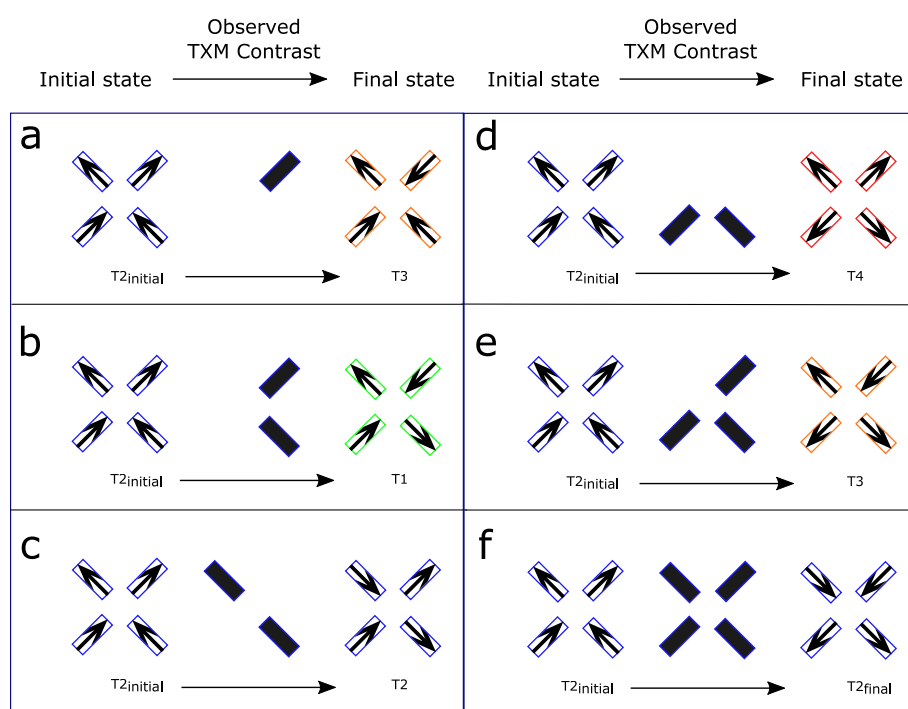


Figure 7.5: The starting state vertex is the left column representing the saturated background of $T2$ vertices, the middle column shows the observed TXM contrast and the final column indicates which vertex would result from such contrast. The end of strings will be Type 3 (a) and they can propagate by separating via strings creating either Type 1 (b) or 2 (c) vertices via the processes shown. The highest energy vertex is indicated by observed contrast in (d). The other possible observed contrast and their corresponding vertices are shown in (e) and (f).

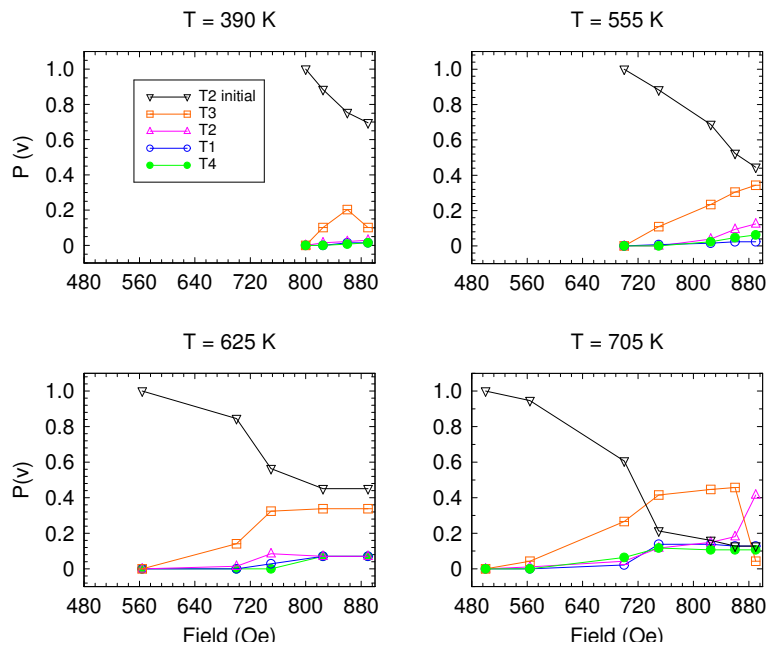


Figure 7.6: The population of different vertex types, $P(v)$, as a function of reversal field and shown for four temperatures; 390, 555, 625 and 705 K.

7.4.2 Vertex populations

Since we start with a known state, *i.e.* a background of Type 2 vertices, when we image the changes in contrast of certain islands we are also able to assign the resulting vertex type as shown in figure 7.5. The end of strings are characterised in the TXM image as a vertex with only one flipped island as shown in the middle column of figure 7.5(a); this indicates a Type 3 vertex or a emergent monopole excitation. Using this information we can map out the vertices in both field and temperature phase space, as shown in figure 7.6. In this figure, we show the fractional populations of the four different vertex types $P(v)$, where $v \in 1, 2, 3, 4$ or 2_{initial} . Type 2 vertices possess a dipole moment and here we have separated out the particular instance of Type 2 where that moment points along the initial saturation direction as a distinct vertex type, along the lines of the background Type 2 vertex defined by Nisoli *et al.* in their theory of effective temperature in a rotationally demagnetised square ice array [55]. This allows us to distinguish between the saturated background and Nambu string defects that are carved in it by the field as it separates a monopole-antimonopole pair, indicated either by the contrast seen in 7.5(b) or (c).

Our experiment extends the field-driven reversal measurements of Pollard *et al.*,[51] who studied square ices, or Mengotti *et al.*, who studied kagome ices,[32] from the athermal regime to the onset of thermalization. The data are shown in figure 7.6 for four different measurement temperatures. At all four temperatures, the system begins with $P(T_{2_{\text{initial}}}) = 1$ and all other populations at zero. As the field is swept, $P(T_{2_{\text{initial}}})$ then drops as vertices are converted into other types by individual islands flipping their vertices. The fact that particular populations rise indicates that there are preferred ways in which this can happen, due to the inter-island coupling. We see a larger population of Type 3 excitations at higher temperatures, indicating an increased preference for nucleating monopole-antimonopole pairs over the propagation of strings through the sample. The latter would be signified by an increase in the values of $P(T_2)$, which is less pronounced. There is also an increase of the highest energy vertices, Type 4, at the highest temperature, showing that the thermal energy is becoming sufficient to explore the whole of phase space. This can be contrasted with the findings of Pollard *et al.*, who found that reversal predominantly occurs through the mechanism of string extension in the athermal limit.[51]

7.5 Injection and avalanche dynamics

Further investigation into the square geometry as a function of lattice spacing was carried out and the effect of temperature and interaction strength on string length and propagation dynamics was investigated. For these experiments there were two different lattice spacings of $a = 350$ and 400 nm. In order to probe exactly how temperature and field played a part in the dynamics of these frustrated ASI we designed injectors to inject monopole excitations into the ASI. These were made to have a large elliptical pad as shown in figure 7.7. This had a reversal field ($H_c \cong 10$ mT) much lower than that of the islands in the array ($H_c \approx 60 - 80$ mT) and therefore could be independently switched. From this pad there was a nanowire which led to the edge of the array. The idea was that a domain wall would travel down this nanowire channel into the vertex and its reversal would create an excited Type-3 vertex. It was expected then that the stray field from this monopole-like excitation would cause further flipping and the excitation would diffuse from this vertex into the array. However, we had little success, experimentally, at injecting with this device. Initially, it seemed the quenched disorder inherent in the array may have been enough that an injection event was as

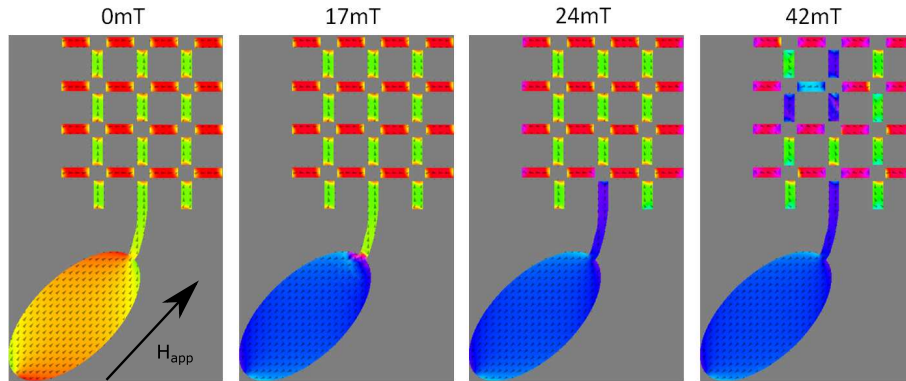


Figure 7.7: Simulation of starting from a saturated state on the left to increasing reversal field. It can be seen that the pad reverses in the second image by 17 mT and on increasing the field more the injector reverses via the propagation of a domain wall from the pad down the nanowire to the vertex. In the final image the next part of the reversal takes place elsewhere in the array and is not propagated from the vertex which is connected to the injector. The mask island were taken from a TEM image (taken at Glasgow University in collaboration with Prof. Steve McVitie and Yue Li) of some 80×250 nm islands with a lattice spacing of 400 nm. Simulations were carried out at 0 K.

likely to happen anywhere. However, after carrying out simulations where the islands were designed to be identical with no disorder and with the mask created from a real TEM image (shown in figure 7.7), the injection from this vertex into the array still was not guaranteed, ruling out the former hypothesis. It is proposed that as the excitation is not produced in a pair (as normally would occur from a Type-1 or 2 ice background), there is less energy-saving to move into the array as there is no oppositely charged partner to separate from. This meant we could not control the exact position and number of injected monopole-antimonopole excitations as required but we were able to engineer starting states with only a few excitations in order to easily follow their trajectories within the field of view. Examples of such states are highlighted in the yellow boxes of figures 7.8 and 7.9. Once injection was obtained, the way in which these monopoles propagated as a function of field and temperature was measured.

An example of the 350 nm lattice spacing is shown in figure 7.8. Firstly, a large saturating field of -73 mT and a temperature of 439 K was applied to create a full Type-2 background. Then a positive injection field of 64 mT was applied for 0.1 s with zero heater current which created 5 separate strings of reversed islands with lengths between

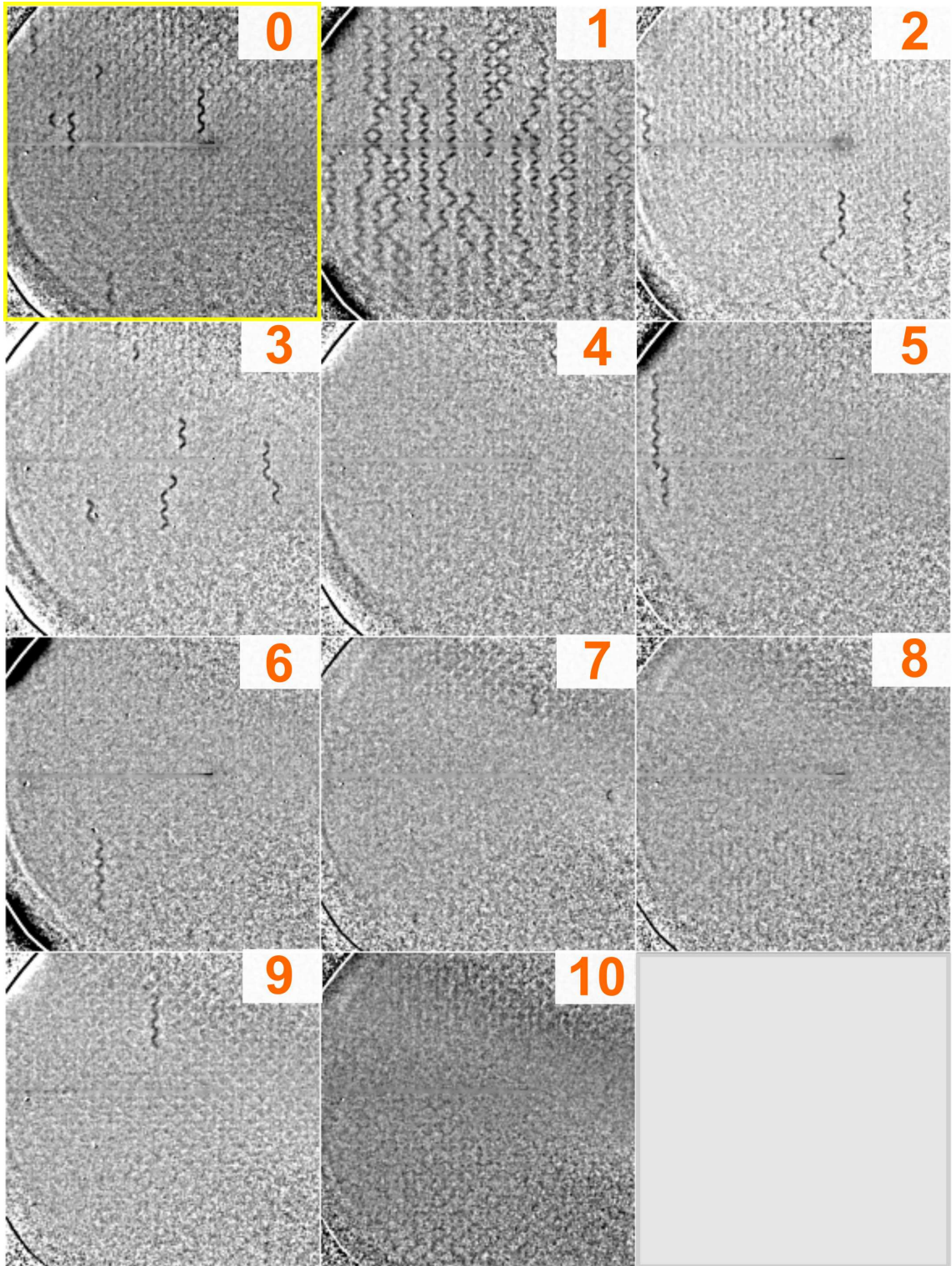


Figure 7.8: An image sequence for 350 nm lattice spacing. The first image at 0 s in the yellow box is the injection state. Each subsequent image is the result of a 0.1 s pulse of 63 mT propagation field and temperature 495 K. Black contrast indicates island reversals.

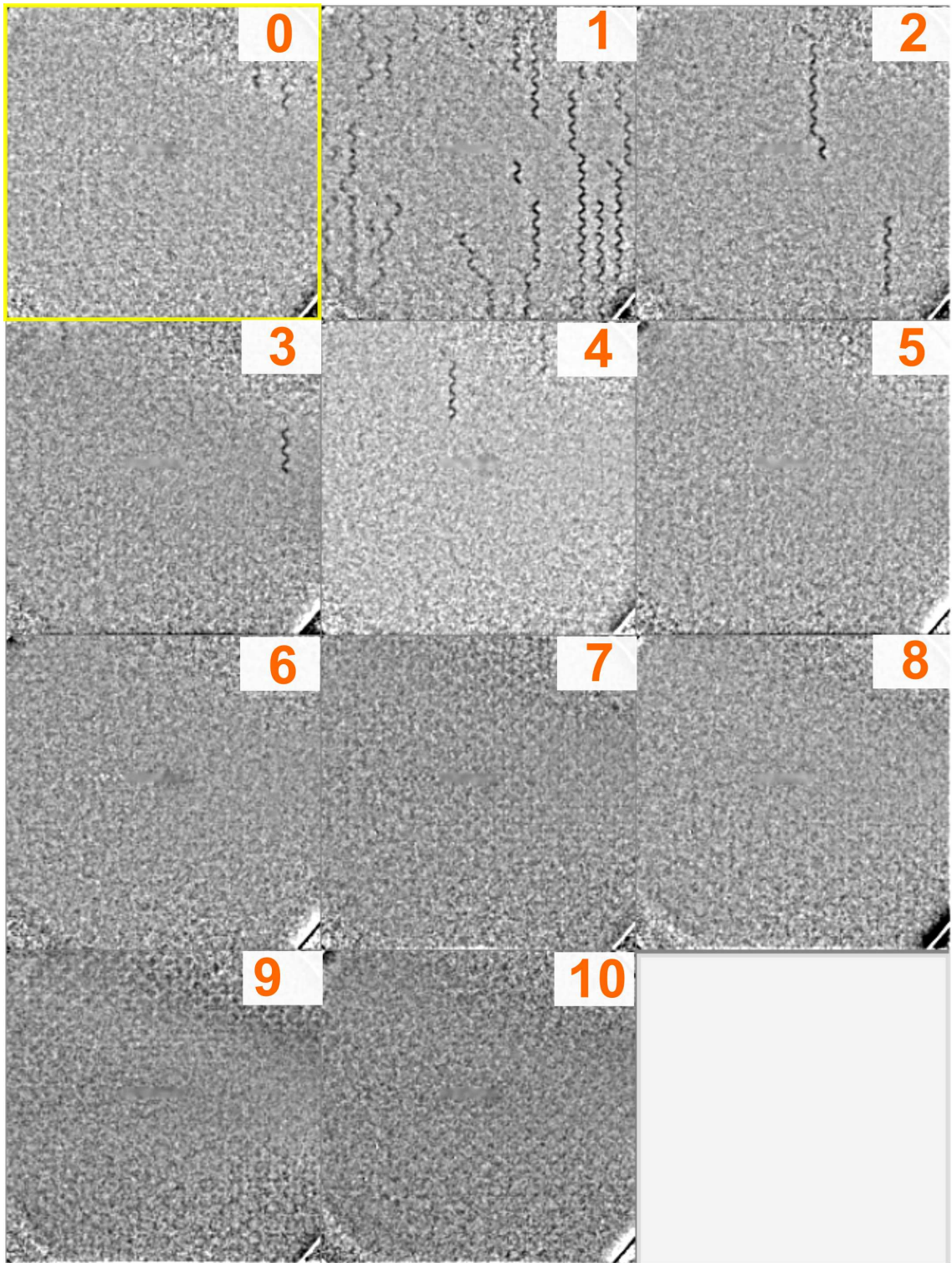


Figure 7.9: The same image sequence as shown in the previous figure for a decreased temperature, 467 K, but the same propagation field 63 mT. Similarly, the first image at 0 s in the yellow box is the injection state. Overall for a decrease in temperature of $\Delta T = 28$ K, there are much fewer island reversals and after the fourth pulse the dynamics have stopped, therefore the overall average velocity of a string is much slower.

2 - 6 islands; this is the injection state (highlighted with a yellow box in the figure). Each image is the average of 8×0.8 s exposures, with a total acquisition time 6.4 s. Just before each subsequent image a propagation field of 63 mT and a temperature of 495 K was applied for 0.1 s and then reduced to zero (for larger applied fields there was considerable shift which caused poor alignment for image processing, this was greatly reduced by returning to zero after each pulse). It can be seen from the image sequence that there is a large initial event after the first propagation field where many strings can be seen within the field of view, after this there are fewer per image but they tend to have lengths, $s > 4$ islands. This was shown to be in contrast to an image sequence with the same propagation field but a lower temperature of 467 K (only $\Delta T = -28$ K), which is plotted in figure 7.9. Here there are many fewer reversals in the same measurement time and actually after the fourth pulse, there were no more island reversals. The average string velocity is calculated as the average avalanche length per frame over the entire pulse sequence which is, for a total of 10 pulses, 1 s. This gives a value of 37 lattice hops s^{-1} compared to 30 lattice hops s^{-1} for the lower temperature. The mean observed avalanche length was also higher for the higher temperature, 10.1 ± 0.8 islands compared to 7.8 ± 0.9 islands.

The separation of these oppositely charged poles can be likened to the flow of electric charge [42; 43] and in order to draw a parallel to this physics we measured the average velocity at various propagation fields. Borrowing the definition of carrier mobility from semiconductor physics, one can write:

$$v_D = \mu E, \tag{7.2}$$

where v_D is the magnitude of the carrier's drift velocity, μ is the mobility (usually quoted in cm^2/Vs) and E is the magnitude of the applied electric field. Beach *et al.* have previously defined a magnetic equivalent quantity to study the average domain wall velocity as a function of applied field in nanowires [122]. We can define a similar quantity which we will call the magnetic mobility, μ_m , for our nanomagnetic system:

$$v_{av} = \mu_m H_{prop}. \tag{7.3}$$

The propagation field, H_{prop} , is analogous to the electric field, providing the “tilted” energy landscape, this tilt defines the preferred direction of propagation which is why the strings expand vertically in the image (*i.e.* along the direction of the applied field). The velocity measured here is subtly different to the drift velocity as the strings should

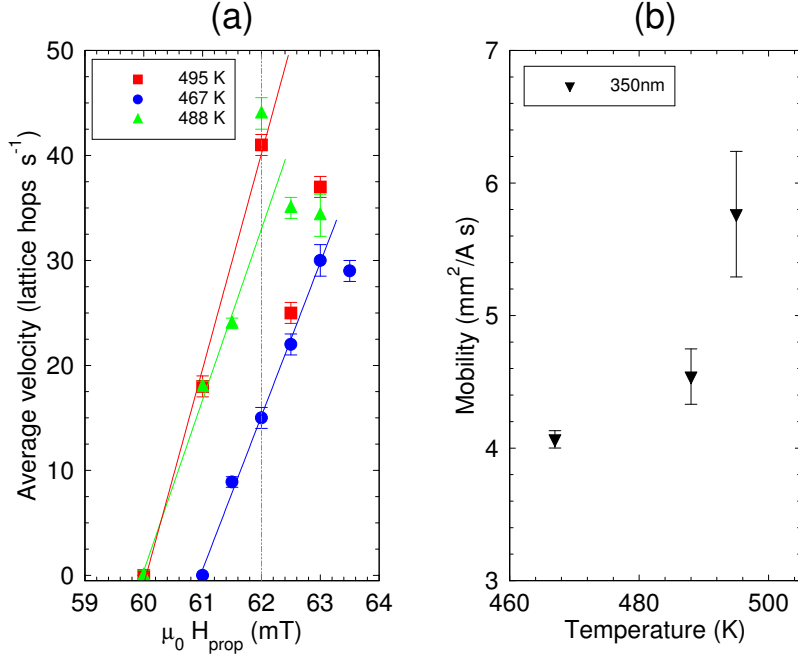


Figure 7.10: (a) The average avalanche velocity plotted in units of the lattice hops per second for different propagation fields. The lowest temperature increases linearly up to $H_{prop}=63$ mT. For the 488 K and 495 K data, the linear region shifts to lower values of propagation field and fits are taken in the low-field region up to 62 mT, indicated by the grey dotted line. The gradients from the fits are replotted as magnetic mobility in (b). The extracted mobility increases for increased temperature.

expand equally in both directions. Although, this could be likened to electron/hole motion.

In figure 7.10, the average velocity as a function of field is plotted and the mobility is extracted by fitting a straight line to the data using eq. 7.3. For the higher temperatures this was only done for the low field region of the data, up to 62 mT. Above this field there are too many excitations within the field of view to extract a meaningful average velocity. At these higher values of field, more than half the visible islands have flipped within the first image of the sequence which limits the dynamics that can then be observed. It is desirable to measure more quickly in order to access these shorter timescales. We can see from figure 7.10(b) that the mobility increases by $1.7 \pm 0.9 mm^2 A^{-1} s^{-1}$ for a relatively small temperature increase, $\Delta T \approx 30$.

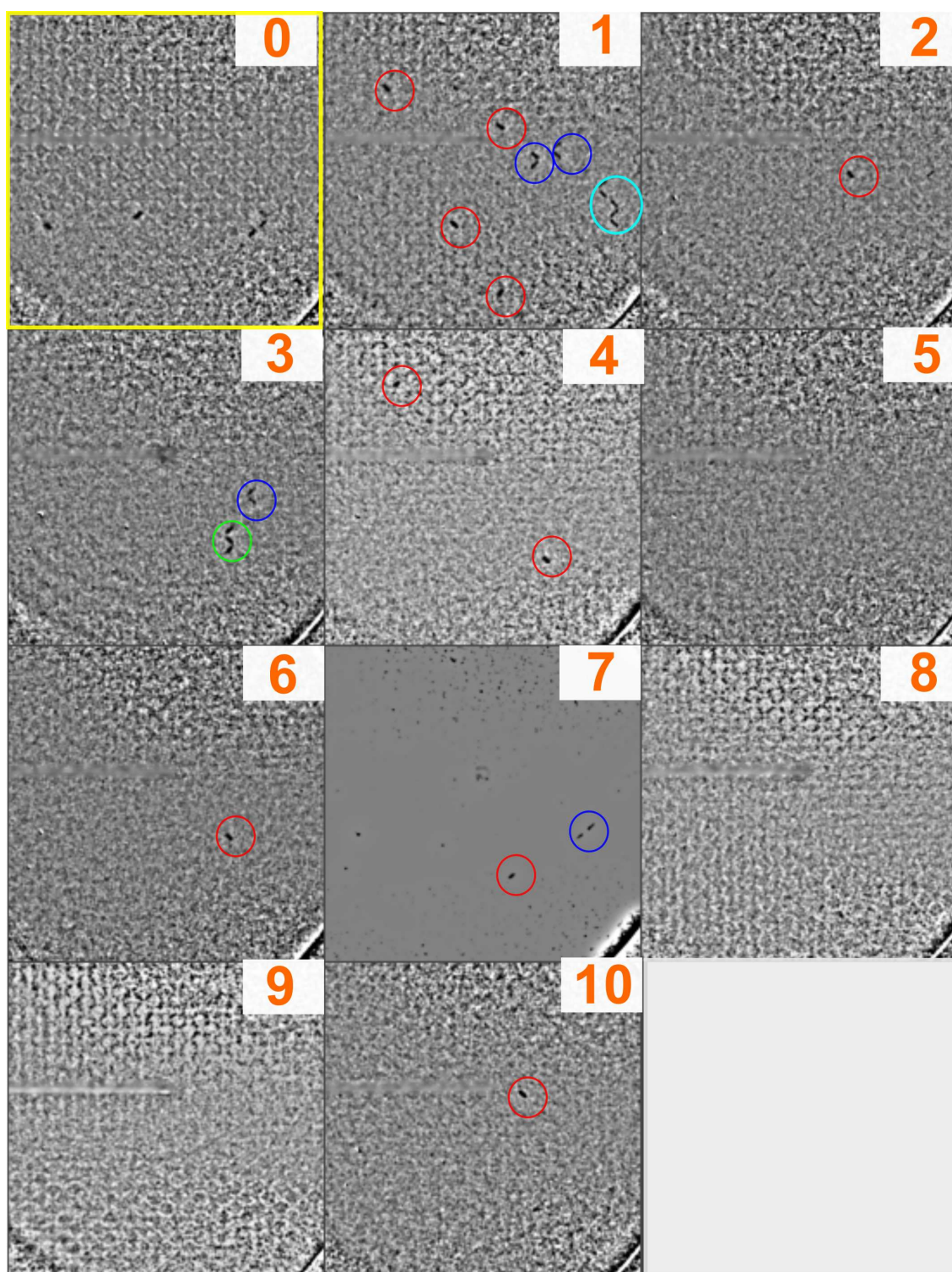


Figure 7.11: Image sequence for a increased lattice spacing of 400 nm. The temperature is 495 K and propagation field 63 mT (same as in figure 7.8). Here the islands which have reversed have been highlighted in order to guide the eye. Single, double and triple chains are circled in red, blue and green respectively. The longest chain observed, is in the second image and is highlighted in turquoise.

7.6 Role of interaction in drift experiments

We were also able to measure the same thing for less strongly interacting ASI. An example of the same experiment as shown in figure 7.8 is shown in figure 7.11. The islands here are the same size but the lattice spacing has been increased to 400 nm. The most striking difference is the average avalanche length is greatly reduced to 2.2 islands, less than a quarter of that observed for the 350 nm lattice spacing for the same temperature and propagation field. The average avalanche speed is more than four times as slow; 8.3 lattice hops s^{-1} cf. 37 lattice hops s^{-1} for the 350 nm lattice spacing. The same analysis to obtain the magnetic mobility at different temperatures was employed and is plotted in figure 7.12(a). For the larger lattice spacing the propagation dynamics are shifted to a higher field range. Also, the velocities are slower than the more closely coupled ones. However, at the highest temperature, 511 K, similar velocities can be reached to those of the lowest temperature of the 350 nm sample. The mobilities for both samples are plotted in figure 7.12(b). There is a very small increase overall in the mobility for the 400 nm sample whereas the more strongly interacting array sees a sharp increase in a smaller temperature window. The more weakly coupled ASI may be better described within the ‘magnetolyte’ framework of Bramwell *et al.* [123], although this has not been further investigated here.

In section 7.4, for a 500 nm array, we saw that the reversal was generally characterised by the creation of monopole-antimonopole pairs and the increased temperature caused an increase in their population. There was less probability of observing T1 or T2 vertices which indicates string propagation. For the more closely coupled arrays their reversal is primarily via strings in the direction of the field. The separation of two oppositely charged T3 vertices can occur via the creation of ground state (T1) vertices or higher energy T2 vertices (figure 7.5). The 350 nm array had a preference for excitations to propagate exclusively in the direction of the field unlike the 400 nm array. Therefore, GS vertices were accessed by the monopoles separating. In the 400 nm array it was also as likely to propagate via the creation of T2 vertices. We can perhaps explain this difference by considering the energy separation of the T1 and T2 vertices for the two different arrays. Calculating the energy of each vertex using the dipole model, the separation in energy is larger for the more strongly coupled arrays which means it requires much more energy to access the T2 state compared to the less strongly coupled array [116]. Therefore, for the same temperature and propagation field it is more likely

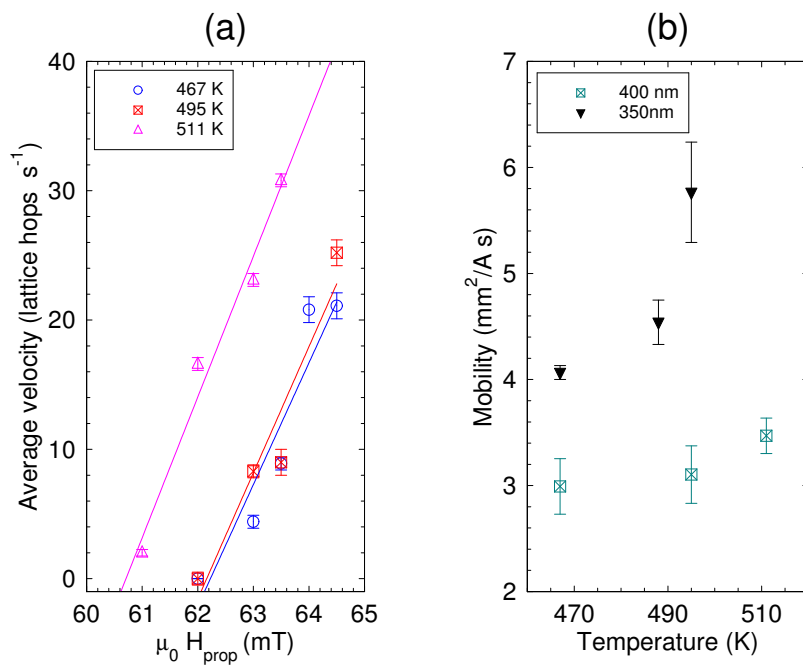


Figure 7.12: (a) The average string velocity for the 400 nm array plotted against the propagation field. (b) The extracted mobility as a function of temperature plotted for both the 350 nm and 400 nm lattice spacing. There is a much more pronounced increase in the mobility in the same temperature range for the more strongly coupled ASI.

that the 350 nm array will reverse via creation of T1 vertices as has been observed. There were no T4 vertices observed for the 350 nm and 400 nm lattice spacing for the temperatures measured, as seen previously in the 500 nm array in section 7.4.2.

7.7 Conclusions

We have been able to image directly the effect of increased temperature on the reversal of an ASI using a newly developed on-membrane heating device. We have shown increased dynamics and changes to the coercivity in the temperature range 298 - 705 K. We have also been able to track the individual vertex populations as a function of both field and temperature. Further to this, we have shown that increased temperature increases the average velocity of the avalanches observed. Finally, we have shown that for less closely coupled arrays there is a large reduction in the average avalanche length and velocity. Decreased interaction causes a decrease in the magnetic mobility and the likelihood of observing longer avalanches.

CHAPTER 8

Summary and Outlook

8.1 Summary and conclusions

Originally the artificial spin ice systems were invented as a tool to help physicists access the microscopic picture of analogous atomic systems, so as to better understand both the statistical mechanics and the driving forces at play in these systems. In order to do this the most vital parts of the quest were to be able to visualise these systems or somehow access the microstates but also to thermalise the components so that real phase transitions are observed and real thermodynamics take place.

Magnetometry on such systems has been carried out over large temperature range owing to the capability to pattern over large enough areas to attain a measurable signal in a high-sensitivity magnetometer, such as the SQUID-VSM used here. These measurements help to characterise the the properties of the ASI but they are also useful in the general area of ‘supermagnetism’. We observe an increased blocking temperature for increased thickness of nominally the same size islands. Also the ZFC curves have shown lower temperature features attributable to a distribution of lower energy barriers which may be a signature of the distribution of the reversal mechanisms within the nanoislands.

The possibility to measure the smallest lateral islands of ASI via the newly developed magnetic XPCS at the Diamond synchrotron (UK) has opened up an avenue for many other condensed matter physicists interested in nanoscale dynamics, as well as providing an interesting and unexpected temperature dependence of our ASI. We found a Vogel-Fulcher temperature dependence for our $30 \times 70 \times 8 \text{ nm}^3$ islands which are only weakly coupled as indicated from the extracted freezing temperature and micro-magnetic calculations. A microscopic picture is been developed to better understand the origin of this behaviour and non-coherent rotation, as supported by simulations using the SEM of islands, is a probable candidate.

Finally, this thesis has demonstrated a microscopy technique, transmission X-ray microscopy, as an alternative tool to study the magnetism of the ASI systems. The required high temperatures to thermally excite such systems have been attained via the design and use of a novel on-membrane heater and thermometer device. The first drift experiments on such systems have shown that both increased temperature and decreased lattice spacing act to increase the mobility of the string excitations which propagate through an initially polarised state.

8.2 Future Work

The possibilities to continue in this field are really quite varied as there are many things which are still not well understood. The effects of the temperature dependence have little been explored and the nature of dynamics at the phase transition from ordered to disordered will prove an interesting area to explore. Recently, new materials with lower ordering temperatures have proven to be useful for experiments to reach the ground state [48], and provide a more strongly interacting system as islands can be thicker whilst maintaining low magnetisations. A more extended study of the dynamic regimes with these types of material seem promising, especially for microscopy where the volumes so far have been experimentally challenging to image.

One such experiment could use the newly developed XPCS technique to investigate the superferromagnetic regime as the glassy and collective behaviour involved should have characteristic ageing behaviour. Again, we would be able to borrow the techniques already ubiquitous in the polymer community, that of the two-time correlation analysis in order to confirm these distinct regimes [124].

Regarding the mobility studies, it will be interesting to see if the different geometries exhibit the same temperature dependence of their magnetic mobility. Routes to reducing the propagation field required would be advantageous for any technological applications and an exploration of different materials for this purpose is also called for.

A possible new direction in light of the magnetometry performed in this thesis could be to answer some of the unknowns in the field of nanoparticle magnetism. There are theoretical discussions concerning the effect of interactions on measures such as the blocking temperature - which has been reported to have a positive *and* negative correlation with T_B [95]. Again, with the control allowed at fabrication and the comparison with the huge volume of work which already exists in this area, the pairing of the two fields could prove as fruitful as that of the spin ice community. This may help to answer many open questions which still exist concerning the effect of interactions on the observed magnetic properties over a large temperature range.

Its unlikely the field will stop growing, although it may encompass more and more layers of complexity, for example lithographically-defined 3D systems [125] and quasi-crystal systems [126] have already been realised. The ability to control, visualise and manipulate the nanomagnetic states with the sophisticated tools now available to experimental researchers will be an attractive prospect for the foreseeable future. It is

really the ability to control defined aspects of a system that provides the most convincing arguments in science and this will always be interesting from a fundamental point of view, but also useful and practical from a technological one.

REFERENCES

- [1] P. Richard, M. Nicodemi, R. Delannay, P. Ribiere and D. Bideau, Slow relaxation and compaction of granular systems, *Nat. Mat.* **4**, 121 (2005) [2](#)
- [2] T. Enoki, K. Tanaka, T. Watanabe, T. Oya, T. Sakiyama et al., Frustrations in polymer conformation in gels and their minimization through molecular imprinting, *Phys. Rev. Lett.* **85**, 5000 (2000) [2](#)
- [3] W. E. Pickett, Erratum: Electronic structure of the high-temperature oxide superconductors, *Rev. Mod. Phys.* **61**, 749 (1989) [2](#)
- [4] A. Lee and A. Wand, Microscopic origins of entropy, heat capacity and the glass transition in proteins, *Nature* **411**, 501 (2001) [2](#)
- [5] L. Pauling, The structure and entropy of ice and of other crystals with some randomness of atomic arrangement, *J. Am. Chem. Soc.* **57**, 2680 (1935) [2](#), [15](#)
- [6] S. T. Bramwell and M. J. P. Gingras, Spin ice state in frustrated magnetic pyrochlore materials, *Science* **294**, 1495 (2001) [2](#), [15](#)
- [7] R. F. Wang, C. Nisoli, R. S. Freitas, J. Li, W. McConville et al., Artificial 'spin ice' in a geometrically frustrated lattice of nanoscale ferromagnetic islands, *Nature* **439**, 303 (2006) [2](#), [3](#), [18](#)
- [8] A. Farhan, P. M. Derlet, A. Kleibert, A. Balan, R. V. Chopdekar et al., Direct observation of thermal relaxation in artificial spin ice, *Phys. Rev. Lett.* **111**, 057204 (2013) [3](#), [21](#), [22](#), [58](#), [67](#)
- [9] N. Rougemaille, F. Montaigne, B. Canals, A. Duluard, D. Lacour et al., Artificial

- kagome arrays of nanomagnets: A frozen dipolar spin ice, *Phys. Rev. Lett.* **106**, 057209 (2011) [3](#)
- [10] R. F. Wang, C. Nisoli, R. S. Freitas, J. Li, W. McConville et al., Demagnetization protocols for frustrated interacting nanomagnet arrays, *J. Appl. Phys.* **101**, 09J104 (2007)
- [11] Y. Qi, T. Brintlinger and J. Cumings, Direct observation of the ice rule in an artificial kagome spin ice, *Phys. Rev. B* **77**, 094418 (2008) [19](#)
- [12] X. Ke, J. Li, C. Nisoli, P. E. Lammert, W. McConville et al., Energy minimization and ac demagnetization in a nanomagnet array, *Phys. Rev. Lett.* **101**, 037205 (2008) [3](#)
- [13] U. B. Arnalds, A. Farhan, R. V. Chopdekar, V. Kapaklis, A. Balan et al., Thermalized ground state of artificial kagome spin ice building blocks, *Appl. Phys. Lett.* **101**, 112404 (2012) [3](#), [21](#)
- [14] A. Farhan, P. M. Derlet, A. Kleibert, A. Balan, R. V. Chopdekar et al., Exploring hyper-cubic energy landscapes in thermally active finite artificial spin-ice systems, *Nat. Phys.* **9**, 375 (2013) [22](#), [58](#), [67](#)
- [15] V. Kapaklis, U. B. Arnalds, A. Farhan, R. V. C. A. Balan, A. Scholl et al., Thermal fluctuations in artificial spin ice, *Nat. Nano.* **9**, 514 (2014) [3](#)
- [16] J. P. Morgan, C. J. Kinane, T. R. Charlton, A. Stein, C. Sánchez-Hanke et al., Magnetic hysteresis of an artificial square ice studied by in-plane bragg x-ray resonant magnetic scattering, *AIP Advances* **2**, 022163 (2012) [3](#), [51](#), [72](#)
- [17] J. Perron, L. Anghinolfi, B. Tudu, N. Jaouen, J.-M. Tonnerre et al., Extended reciprocal space observation of artificial spin ice with x-ray resonant magnetic scattering, *Phys. Rev. B* **88**, 214424 (2013) [3](#), [51](#), [72](#)
- [18] S. T. Bramwell and M. J. Harris, Frustration in ising-type spin models on the pyrochlore lattice, *J. Phys.: Cond. Matt.* **10**, L215 (1998) [4](#)
- [19] L. D. C. Jaubert, M. Haque and R. Moessner, Analysis of a fully packed loop model arising in a magnetic coulomb phase, *Phys. Rev. Lett.* **107**, 177202 (2011) [4](#)

REFERENCES

- [20] R. P. Cowburn, D. K. Koltsov, A. O. Adeyeye, M. E. Welland and D. M. Tricker, Single-domain circular nanomagnets, *Phys. Rev. Lett.* **83**, 1042 (1999) [6](#)
- [21] J. M. D. Coey, *Magnetism and Magnetic Materials*, Cambridge University Press (2010) [7](#)
- [22] J. Osborn, Demagnetizing factors of the general ellipsoid, *Phys. Rev.* **67**, 351 (1945) [7](#)
- [23] R. Skomski, *Simple Models of Magnetism*, Oxford University Press (2008) [8](#)
- [24] E. Stoner and E. Wohlfarth, A mechanism of magnetic hysteresis in heterogeneous alloys, *Philosophical transactions of the Royal Society of London series A-mathematical and physical sciences* **240**, 599 (1948) [8](#)
- [25] J.-M. Porro Azpiazu, *Exploiting magnetic dipolar interactions in artificially nano-structured systems*, Ph.D. thesis, University of the Basque Country (2014) [8](#)
- [26] L. Néel, Superparamagnetism, *Ann. Geophys.* **5**, 99 (1949) [9](#), [81](#)
- [27] W. F. Brown, Rigorous approach to the theory of ferromagnetic microstructure, *J. Appl. Phys.* **29**, 470 (1958) [9](#), [81](#)
- [28] R. H. Victora, Predicted time dependence of the switching field for magnetic materials, *Phys. Rev. Lett.* **63**, 457 (1989) [10](#), [94](#)
- [29] M. P. Sharrock, Time dependence of switching fields in magnetic recording media (invited), *J. Appl. Phys.* **76**, 6413 (1994) [10](#)
- [30] R. Cowburn, Property variation with shape in magnetic nanoelements, *J. Phys. D: Appl. Phys.* **33**, R1 (1999) [11](#), [12](#), [63](#), [65](#)
- [31] S. Blundell, *Magnetism in Condensed Matter*, Oxford Master Series in Condensed Matter Physics 4, Oxford University Press (2001) [10](#)
- [32] E. Mengotti, L. J. Heyderman, A. F. Rodriguez, F. Nolting, R. V. Hugli et al., Real-space observation of emergent magnetic monopoles and associated dirac strings in artificial kagome spin ice, *Nat. Phys.* **7**, 68 (2011) [11](#), [19](#), [20](#), [22](#), [100](#)
- [33] C. Castelnovo, R. Moessner and S. L. Sondhi, Magnetic monopoles in spin ice, *Nature* **451**, 42 (2008) [11](#), [15](#), [16](#)

REFERENCES

- [34] P. Li, G. Csaba, V. K. Sankar, X. Ju, P. Lugli et al., Switching behavior of lithographically fabricated nanomagnets for logic applications, *J. Appl. Phys.* **111**, 07B911 (2012) [13](#)
- [35] M. Bode, O. Pietzsch, A. Kubetzka and R. Wiesendanger, Shape-dependent thermal switching behavior of superparamagnetic nanoislands, *Phys. Rev. Lett.* **92**, 067201 (2004) [13](#)
- [36] R. P. Cowburn, A. O. Adeyeye and M. E. Welland, Controlling magnetic ordering in coupled nanomagnet arrays, *New J. Phys.* **1**, 16 (1999) [13](#)
- [37] J. D. Bernal and R. H. Fowler, A Theory of Water and Ionic Solution, with Particular Reference to Hydrogen and Hydroxyl Ions, *J. Chem. Phys.* **1**, 515 (1933) [15](#)
- [38] W. F. Giauque and J. W. Stout, The entropy of water and the third law of thermodynamics. the heat capacity of ice from 15 to 273k., *J. Am. Chem. Soc.* **58**, 1144 (1936) [15](#)
- [39] A. P. Ramirez, A. Hayashi, R. J. Cava, R. Siddharthan and B. S. Shastry, Zero-point entropy in 'spin ice', *Nature* **399**, 333 (1999) [15](#)
- [40] M. J. Harris, S. T. Bramwell, D. F. McMorrow, T. Zeiske and K. W. Godfrey, Geometrical frustration in the ferromagnetic pyrochlore $\text{Ho}_2\text{Ti}_2\text{O}_7$, *Phys. Rev. Lett.* **79**, 25544 (1997) [15](#)
- [41] P. Dirac, Quantised singularities in the electromagnetic field, *Philos. T. R. Soc. Lond. A* **133**, 60 (1931) [15](#)
- [42] S. T. Bramwell, S. R. Giblin, S. Calder, R. Aldus, D. Prabhakaran et al., Measurement of the charge and current of magnetic monopoles in spin ice, *Nature* **461**, 956 (2009) [15](#), [104](#)
- [43] S. R. Giblin, S. T. Bramwell, P. C. W. Holdsworth, D. Prabhakaran and I. Terry, Creation and measurement of long-lived magnetic monopole currents in spin ice, *Nat. Phys.* **7**, 252 (2011) [15](#), [104](#)

-
- [44] J. P. Morgan, A. Stein, S. Langridge and C. H. Marrows, Thermal ground-state ordering and elementary excitations in artificial magnetic square ice, *Nat. Phys.* **7**, 75 (2011) [17](#), [21](#)
- [45] I. Gilbert, G.-W. Chern, S. Zhang, L. O'Brien, B. Fore et al., Emergent ice rule and magnetic charge screening from vertex frustration in artificial spin ice, *Nat. Phys.* **10**, 671 (2014) [19](#), [21](#)
- [46] G.-W. Chern, P. Mellado and O. Tchernyshyov, Two-stage ordering of spins in dipolar spin ice on kagome, *Phys. Rev. Lett.* **106**, 6413 (2011) [18](#)
- [47] S. Zhang, I. Gilbert, C. Nisoli, G.-W. Chern, M. J. Erickson et al., Crystallites of magnetic charges in artificial spin ice, *Nature* **500**, 553 (2013) [18](#), [19](#), [21](#)
- [48] J. Drisko, S. Daunheimer and J. Cumings, FePd₃ as a material for studying thermally active artificial spin ice systems, *Phys. Rev. B* **91**, 224406 (2015) [18](#), [19](#), [21](#), [22](#), [112](#)
- [49] M. Tanaka, E. Saitoh, H. Miyajima, T. Yamaoka and Y. Iye, Magnetic interactions in a ferromagnetic honeycomb nanoscale network, *Phys. Rev. B* **73**, 052411 (2006) [19](#)
- [50] G. Moller and R. Moessner, Artificial square ice and related dipolar nanoarrays, *Phys. Rev. Lett.* **96**, 237202 (2006) [19](#)
- [51] S. D. Pollard, V. Volkov and Y. Zhu, Propagation of magnetic charge monopoles and Dirac flux strings in an artificial spin-ice lattice, *Phys. Rev. B* **85**, 1 (2012) [20](#), [100](#)
- [52] S. Ladak, D. E. Read, G. K. Perkins, L. F. Cohen and W. R. Branford, Direct observation of magnetic monopole defects in an artificial spin-ice system, *Nat. Phys.* **6**, 359 (2010) [20](#)
- [53] Y. Nambu, Strings, monopoles, and gauge fields, *Phys. Rev. D* **10**, 4262 (1974) [20](#)
- [54] L. A. S. Mól, A. R. Pereira and W. A. Moura-Melo, Extending spin ice concepts to another geometry: The artificial triangular spin ice, *Physical Review B* **85**, 184410 (2012) [20](#)

-
- [55] C. Nisoli, J. Li, X. Ke, D. Garand, P. Schiffer et al., Effective temperature in an interacting vertex system: Theory and experiment on artificial spin ice, *Phys. Rev. Lett.* **105**, 047205 (2010) [20](#), [99](#)
- [56] J. Morgan, J. Akerman, A. Stein, C. Phatak, R. M. L. Evans et al., Real and effective thermal equilibrium in artificial square spin ices, *Phys. Rev. B* **87**, 024405 (2013)
- [57] C. Nisoli, On thermalization of magnetic nano-arrays at fabrication, *New J. Phys.* **14**, 035017 (2012) [20](#)
- [58] P. E. Lammert, X. Ke, J. Li, C. Nisoli, D. M. Garand et al., Direct entropy determination and application to artificial spin ice, *Nat. Phys.* **6**, 786 (2010) [21](#)
- [59] P. E. Lammert, V. H. Crespi and C. Nisoli, Gibbsianizing nonequilibrium dynamics of artificial spin ice and other spin systems, *New J. Phys.* **14**, 045009 (2012) [21](#)
- [60] J. M. Porro, A. Bedoya-Pinto, A. Berger and P. Vavassori, Exploring thermally induced states in square artificial spin-ice arrays., *New J. Phys.* **15**, 055012 (2013) [21](#), [61](#)
- [61] V. Kapaklis, U. B. Arnalds, A. Harman-Clarke, E. T. Papaioannou, M. Karimipour et al., Melting artificial spin ice, *New J. Phys.* **14** (2012) [21](#), [97](#)
- [62] Z. Budrikis, K. L. Livesey, J. P. Morgan, J. Akerman, A. Stein et al., Domain dynamics and fluctuations in artificial square ice at finite temperatures., *New J. Phys.* **14**, 035014 (2012) [22](#)
- [63] Z. Budrikis, P. Politi and R. L. Stamps, Vertex dynamics in finite two-dimensional square spin ices, *Phys. Rev. Lett.* **105**, 017201 (2010) [22](#)
- [64] D. Levis and L. F. Cugliandolo, Out-of-equilibrium dynamics in the bidimensional spin-ice model, *EPL* **97**, 30002 (2012) [22](#)
- [65] Z. Budrikis, J. P. Morgan, J. Akerman, A. Stein, P. Politi et al., Disorder strength and field-driven ground state domain formation in artificial spin ice: Experiment, simulation, and theory, *Phys. Rev. Lett.* **109**, 037203 (2012) [22](#)

-
- [66] J. Y. Cheng, W. Jung and C. A. Ross, Magnetic nanostructures from block copolymer lithography: Hysteresis, thermal stability, and magnetoresistance, *Phys. Rev. B* **70**, 064417 (2004) 22
- [67] K. K. Kohli, A. L. Balk, J. Lie, S. Zhang, I. Gilbert et al., Magneto-optical kerr effect studies of square artificial spin ice, *Phys. Rev. B* **84**, 180412 (2011) 22, 59
- [68] W. Bragg and W. Bragg, The reflection of x-rays by crystals, *Philos. T. R. Soc. Lond. A* **88**, 428 (1913) 26
- [69] J. Als-Nielsen and D. McMorrow, *Elements of Modern X-ray Physics*, John Wiley and Sons, Ltd. (2001) 26, 28
- [70] M. Blume, Magnetic scattering of x-rays, *J. Appl. Phys.* **57**, 3615 (1985) 26
- [71] J. Stöhr and H. Siegmann, *Magnetism: From Fundamentals to Nanoscale Dynamics*, Springer Series in Solid-State Sciences, Springer Berlin Heidelberg (2007) 28, 29
- [72] G. van der Laan, Soft x-ray resonant magnetic scattering of magnetic nanostructures, *C. R. Physique* **9**, 570 (2008) 28
- [73] F. Livet, F. Bley, F. Ehrburger-Dolle, I. Morfin, E. Geissler et al., X-ray intensity fluctuation spectroscopy by heterodyne detection, *J. Sync. Rad.* **13**, 453 (2006) 30, 81
- [74] E. Geissler, *Dynamic Light Scattering*, Clarendon Press, Oxford (1993) 31
- [75] P. Pusey and W. Van Megen, Dynamic light scattering by non-ergodic media, *Physica A* **157**, 705 (1989) 31, 32
- [76] G. Binnig, H. Rohrer, C. Gerber and E. Weibel, Surface studies by scanning tunneling microscopy, *Phys. Rev. Lett.* **49**, 57 (1982) 43
- [77] D. Rugar, H. Mamin, P. Guethner, S. Lambert, J. Stern et al., Magnetic force microscopy: General principles and applications to longitudinal recording media, *J. Appl. Phys.* **68**, 1169 (1990) 44
- [78] Mpms squid-vsm reference manual, *Technical report* (2010) 45

-
- [79] S. Foner, Versatile and sensitive vibrating-sample magnetometer, *Rev. Sci. Inst.* **30**, 548 (1959) [44](#)
- [80] H. Kiessig, Interference of x-rays in thick layers, *Annalen Der Physik* **10**, 769 (1931) [46](#)
- [81] W. L. Chao, B. D. Harteneck, J. A. Liddle, E. H. Anderson and D. T. Attwood, Soft x-ray microscopy at a spatial resolution better than 15nm, *Nature* **435**, 1210 (2005) [46](#)
- [82] P. Fischer, D.-H. Kim, W. Chao, J. A. Liddle, E. H. Anderson et al., Soft X-ray microscopy of nanomagnetism, *Mater. Today* **9**, 26 (2006) [46](#)
- [83] G. Kusinski, K. Krishnan, G. Thomas, G. Denbeaux, D. Weller et al., Magnetic imaging of ion-irradiation patterned co/pt multilayers using complementary electron and photon probes, *App. Phys. Lett.* **79** (2001) [47](#)
- [84] T. A. W. Beale, T. P. A. Hase, T. Iida, K. Endo, P. Steadman et al., RASOR: An advanced instrument for soft x-ray reflectivity and diffraction, *Rev. Sci. Inst.* **81** (2010) [50](#)
- [85] C. H. Marrows, P. Steadman, A. C. Hampson, L.-A. Michez, B. J. Hickey et al., Probing magnetic ordering in multilayers using soft x-ray resonant magnetic scattering, *Phys. Rev. B* **72**, 024421 (2005) [51](#), [74](#)
- [86] R. L. Leheny, Xpcs: Nanoscale motion and rheology, *Curr. Opin. Colloid In.* **17**, 3 (2012) [53](#)
- [87] M. J. Donahue and D. G. Porter, OOMMF User's Guide, Version 1.0, *Interagency Report NISTIR 6376*, National Institute of Standards and Technology, Gaithersburg, MD (1999) [55](#)
- [88] A. Vansteenkiste and B. Van de Wiele, MuMax: A new high-performance micro-magnetic simulation tool, *J. Magn. Magn. Mater.* **323**, 2585 (2011) [55](#), [87](#)
- [89] U. B. Arnalds, M. Ahlberg, M. S. Brewer, V. Kapaklis, E. T. Papaioannou et al., Thermal transitions in nano-patterned XY-magnets, *App. Phys. Lett.* **105**, 042409 (2014) [57](#), [63](#)

-
- [90] C. P. Bean and J. D. Livingston, Superparamagnetism, *J. Appl. Phys.* **30**, S120 (1959) [59](#), [93](#)
- [91] S. A. Morley, A. Stein, M. C. Rosamond, D. Alba Venero, A. Hrabec et al., Temperature and magnetic-field driven dynamics in artificial magnetic square ice, *Proc. SPIE* **9551**, [95511Q](#) (2015) [61](#), [92](#)
- [92] S. Bedanta and W. Kleemann, Supermagnetism, *J. Phys. D-Appl. Phys.* **42**, [013001](#) (2009) [63](#), [67](#)
- [93] W. C. Nunes, W. S. D. Folly, J. P. Sinnecker and M. A. Novak, Temperature dependence of the coercive field in single-domain particle systems, *Phys. Rev. B* **70**, [014419](#) (2004) [63](#), [65](#)
- [94] R. C. Temple, A. P. Mihai, D. a. Arena and C. H. Marrows, Ensemble magnetic behavior of interacting CoFe nanoparticles, *Front. Phys.* **3**, [1](#) (2015) [65](#)
- [95] X. Batlle and A. Labarta, Finite-size effects in fine particles: magnetic and transport properties, *J. Phys. D: App. Phys.* **35**, R15 (2002) [65](#), [112](#)
- [96] S. Mørup and E. Tronc, Superparamagnetic relaxation of weakly interacting particles, *Phys. Rev. Lett.* **72**, [3278](#) (1994) [65](#)
- [97] S. Shtrikman and E. P. Wohlfarth, The theory of the vogel-fulcher law of spin glasses, *Phys. Lett.* **85**, 467 (1981) [65](#), [84](#), [88](#)
- [98] M. R. Freeman and B. C. Choi, Advances in magnetic microscopy., *Science* **294**, [1484](#) (2001) [71](#)
- [99] R. Wiesendanger, Spin mapping at the nanoscale and atomic scale, *Rev. Mod. Phys.* **81**, [1495](#) (2009) [71](#)
- [100] R. Pecora, *Dynamic Light Scattering: Applications of Photon Correlation Spectroscopy*, Springer US (2013) [71](#), [81](#)
- [101] S. Sinha, Z. Jiand and L. Lurio, X-ray photon correlation spectroscopy studies of surfaces and thin films, *Adv. Mater.* **26**, 7764 (2014) [71](#)
- [102] G. Beutier, A. Marty, F. Livet, G. van der Laan, S. Stanescu et al., Soft x-ray coherent scattering: Instrument and methods at esrf id08, *Rev. Sci. Inst.* **78**, [093901](#) (2007) [74](#), [75](#), [77](#)

-
- [103] R. Nakajima, J. Stöhr and Y. U. Idzerda, Electron-yield saturation effects in l-edge x-ray magnetic circular dichroism spectra of fe, co, and ni, *Phys. Rev. B* **59**, 6421 (1999) 75
- [104] R. Bergman, *Dynamic Light Scattering Studies of Glass-forming Liquids*, Springer Science and Business Media (1996) 78
- [105] M. Sutton, S. G. J. Mochrie, T. Greytak, S. E. Nagler, L. E. Berman et al., Observation of speckle by diffraction with coherent x-rays, *Nature* **352**, 608 (1991) 78
- [106] L. Cipelletti, L. Ramos, S. Manley, E. Pitard, D. A. Weitz et al., Universal non-diffusive slow dynamics in aging soft matter, *Faraday Discuss.* **123**, 237 (2003) 78
- [107] O. G. Shpyrko, E. D. Isaacs, J. M. Logan, Y. Feng, G. Aeppli et al., Direct measurement of antiferromagnetic domain fluctuations, *Nature* **447**, 68 (2007) 80
- [108] S. Konings, C. Schüßler-Langeheine, H. Ott, E. Weschke, E. Schierle et al., Magnetic domain fluctuations in an antiferromagnetic film observed with coherent resonant soft x-ray scattering, *Phys. Rev. Lett.* **106**, 077402 (2011) 80
- [109] S.-W. Chen, H. Guo, K. A. Seu, K. Dumesnil, S. Roy et al., Jamming behavior of domains in a spiral antiferromagnetic system, *Phys. Rev. Lett.* **110**, 217201 (2013) 80
- [110] M. S. Pierce, C. R. Buechler, L. B. Sorensen, S. D. Kevan, E. a. Jagla et al., Disorder-induced magnetic memory: Experiments and theories, *Phys. Rev. B* **75**, 1 (2007) 80
- [111] M. S. Pierce, K. C. Chang, D. Hennessy, V. Komanicky, M. Sprung et al., Surface X-Ray Speckles: Coherent Surface Diffraction from Au(001), *Phys. Rev. Lett.* **103**, 1 (2009) 80
- [112] M. S. Pierce, A. Barbour, V. Komanicky, D. Hennessy and H. You, Coherent x-ray scattering experiments of Pt(001) surface dynamics near a roughening transition, *Phys. Rev. B* **86**, 184108 (2012) 80

-
- [113] J. Tholence, On the frequency dependence of the transition temperature in spin glasses, *Solid State Commun.* **35**, 113 (1980) 84
- [114] M. Cyrot, A possible origin for the vogel-fulcher law, *Phys. Lett. A* **83**, 275 (1981) 84
- [115] J. A. Osborn, Demagnetizing factors of the general ellipsoid, *Phys. Rev.* **67**, 351 (1945) 84, 93
- [116] R. Wang, *Geometrical magnetic frustration and demagnetization of artificial spin ice*, Ph.D. thesis, Pennsylvania State University (2007) 85, 107
- [117] J. Gadbois and J.-G. Zhu, Effect of edge roughness in nano-scale magnetic bar switching, *IEEE Trans. Magn.* **31**, 3802 (1995) 85
- [118] S. Gliga, A. Kákay, L. J. Heyderman, R. Hertel and O. G. Heinonen, Broken vertex symmetry and finite zero-point entropy in the artificial square ice ground state, *Phys. Rev. B* **92**, 060413 (2015) 90
- [119] H. Pfeiffer, Determination of anisotropy field distribution in particle assemblies taking into account thermal fluctuations, *Phys. Status Solidi A* **118**, 295 (1990) 93
- [120] J. W. Harrell, Orientation dependence of the dynamic coercivity of Stoner-Wohlfarth particles, *IEEE Trans. Magn.* **37**, 533 (2001) 94
- [121] A. S. Morris, *Measurement and instrumentation principles*, Butterworth-Heinemann (2001) 95
- [122] G. S. D. Beach, C. Nistor, C. Knutson, M. Tsoi and J. L. Erskine, Dynamics of field-driven domain-wall propagation in ferromagnetic nanowires., *Nat. Mat.* **4**, 741 (2005) 104
- [123] V. Kaiser, S. T. Bramwell, P. C. W. Holdsworth and R. Moessner, ac wien effect in spin ice, manifest in nonlinear, nonequilibrium susceptibility, *Phys. Rev. Lett.* **115**, 037201 (2015) 107
- [124] O. G. Shpyrko, X-ray photon correlation spectroscopy, *J. Synchrotron Rad.* **21**, 1057 (2014) 112

REFERENCES

- [125] C. Donnelly, M. Guizar-Sicairos, V. Scagnoli, M. Holler, T. Huthwelker et al., Element-specific x-ray phase tomography of 3d structures at the nanoscale, *Phys. Rev. Lett.* **114**, 115501 (2015) 112
- [126] V. S. Bhat, J. Sklenar, B. Farmer, J. Woods, J. T. Hastings et al., Controlled magnetic reversal in permalloy films patterned into artificial quasicrystals, *Phys. Rev. Lett.* **111**, 077201 (2013) 112